Transverse Thermoelectric Effects for Cooling and Heat Flux Sensing

By

Brooks Samuel Mann

Thesis submitted to the Faculty of the
Virginia Polytechnic Institute and State University
in partial fulfillment of the requirements for the degree of
Master of Science
in
Mechanical Engineering

Approved:

_____

Scott T. Huxtable, Advisor

_____

Elaine P. Scott, Committee Member

_____

Thomas E. Diller, Committee Member

June 16, 2006
Blacksburg, Virginia

Keywords: transverse thermoelectrics, cooling, heat flux sensing, semiconductor, bismuth telluride, Seebeck, Peltier, anisotropy

Transverse Thermoelectric Effects for Cooling and Heat Flux Sensing

Brooks Samuel Mann

(Abstract)

While thermoelectric technology has developed steadily over the last 50 years, transverse thermoelectrics have generally been ignored in the industrial and commercial uses of thermoelectric devices to date. This project focuses on investigating transverse thermoelectric effects for localized cooling and heat flux sensing. Thermoelectric cooling devices are useful when their advantages (small size, solid state, active temperature control) outweigh their relatively poor efficiency. Transverse heat flux sensors, which generate an electric field in a direction orthogonal to the heat flow, have the advantage that the signal depends on the length of the device rather than the thickness. Thus, they can be made very thin for fast response times while maintaining a large signal.

A prototype transverse device was built out of bulk samples of bismuth and bismuth telluride, which are common thermoelectric materials. The device was constructed of alternating layers of the constituent materials to simulate the effects of an intrinsically anisotropic material. The device was tested for its cooling and heat flux sensing capabilities, and the results of this testing were compared to predicted values. Although the device failed to demonstrate cooling, its heat flux sensing capabilities were promising. The device was tilted to several angles of inclination between 44° and 84° from horizontal, and the output voltage was recorded for several values of heat flux. The signal strength varied between 190.2 and 2321.6 $\mu V/(W/cm^2)$, at inclination angles of 84° and 44°, respectively. The results followed the trend of the predicted values well, but the magnitude of the output voltage was significantly lower than expected. An uncertainty analysis was performed, and it was determined that the most likely source of error was the uncertainty in the amount of heat flux that went through the device during testing.

This thesis outlines the process of building and testing the device, and the analysis of the results. Recommendations for future work are also given.

Acknowledgements

I would like to thank Dr. Scott Huxtable, my advisor, for the opportunity to perform this research. His constant support and advice helped me to solve the problems and overcome the obstacles I encountered throughout the process. I also greatly appreciate the help and support of Dr. Elaine Scott and Dr. Thomas Diller, the other members of my committee. Many friends and fellow students provided technical and organizational advice, including Nitin Shukla, Manu Mital, Jerrod Ewing, Christian James, and Andrew Gifford. The faculty, staff, and students of the Center for Power Electronics (CPES) also deserve thanks for technical advice and for the annual conferences that added greatly to my engineering knowledge and professional skills. This project was funded primarily through CPES by the ERC Program of the National Science Foundation (NSF) under Award Number EEC-9731677.

Many friends have provided companionship and encouragement during my six years at Virginia Tech, which is greatly appreciated. Finally, I would like to thank my family for their unwavering support and interest in my studies throughout my coursework and research. Without the support of my family I doubt I could have made it this far.

Table of Contents

List of Figures

List of Tables

Chapter 1 – Introduction

1.1 Motivation

The initial goal of this project was to develop a transverse thermoelectric device that could demonstrate cooling and heat flux sensing capabilities. Thermoelectric applications have been limited due to low efficiency, and the transverse effects exhibit certain advantages that may lead to better and more useful thermoelectric devices. The specific application that this project was initially geared towards was a thin-film transverse thermoelectric device for localized cooling on electronic chips. A device was built from bulk thermoelectric materials to simulate the characteristics of a thin-film device, and was tested for its cooling capabilities. However, the device performance when used as a heat flux sensor was much more promising. A future project may continue the pursuit of a thin-film device that takes advantage of the transverse effects.

1.2 Thermoelectric Cooling Devices

A thermoelectric cooler is a solid state heat pump that uses the Peltier effect, and works in conjunction with a heat sink to remove heat from a system. Most applications that require cooling do not employ thermoelectrics because of the low values of efficiency that are inherent in thermoelectric coolers (TECs). A TEC requires relatively large amounts of electrical power in order to produce a cooling effect. In fact, more conventional systems such as vapor compression refrigeration cycles have as much as a 3 to 1 advantage in efficiency over thermoelectrics [1]. However, TECs can be useful in cetain applications where the advantages outweigh the disadvantages.

TECs are solid state, and so they produce no noise and require little to no maintenance. They also are quite small when compared to other systems, and so can be useful when there is a limited amount of space in a system. Figure 1.1 shows three examples of commercial TECs made by Marlow®. Despite their small size, these devices

can all create temperature differences of around 65 °C [2]. They can also be stacked on top of each other to create even larger temperature differences. Because of their small size, TECs can be used for localized cooling, where only a small part of the system needs to be cooled.

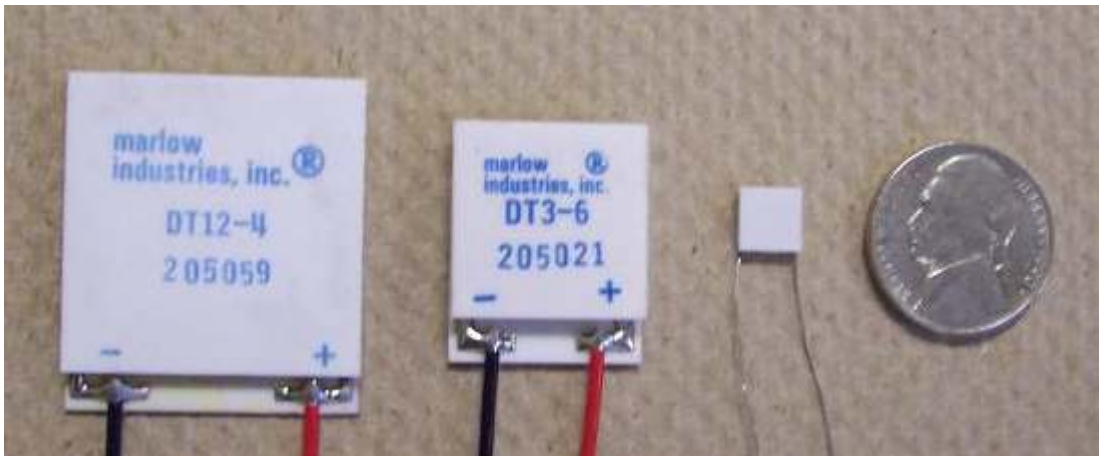

Figure 1.1. Three examples of commercially available TECs. To achieve the maximum temperature difference of 65 °C, the DT12-4 uses 36 W of electrical power, the DT3-6 uses 13 W, and the MI1021T-03AC-09 (right) uses 2.2 W (assuming an ambient temperature of 27°C).

TECs are also useful as "active temperature control" devices. A simple feedback loop can be used to implement a TEC in a system where a specific temperature is required, because the temperature of one side of the TEC is directly proportional to the input power. The "cold" side of the device can be either cooled or heated to the proper temperature, depending on the direction of the electrical current. As long as the temperature is within the range of the device, and a proper heat sink / heat source is used on the other side, the temperature can be controlled quite accurately.

The current applications of TECs are minimal because of the low efficiency values associated with them. Marlow lists some possible uses of TECs as "temperature stabilization of bolometers and ferroelectric detectors, laser diode arrays in fiber optic systems, and maintaining constant viscosity in ink jet printers." In a more general sense, TECs can be used where there is limited space, low maintenance is desirable, active temperature control is needed, or another of the advantages of thermoelectrics can be applied. Possibly the most widespread current use of TECs is in small refrigerators and

beverage coolers. They are much less efficient than other refrigerators and coolers, but are also much lighter and quieter.

1.3 Heat Flux Sensors and Power Generators

Heat flux sensors are useful in any application where it is important to know about how and where thermal energy goes. Most industrial processes have some method of temperature measurement, but in some instances the amount of heat flux is just as important [3]. Heat flux sensors can help determine if a certain process is running properly and efficiently, or if energy is reaching its proper destination in a system.

Thermoelectric heat flux sensors can have the same structure as TECs, but work somewhat in reverse. A temperature difference across the device (which is proportional to the heat flux flowing through the device) creates an electrical signal which can be measured. Properly calibrated, the device can determine the energy flow from any surface, or the radiative energy from a remote source such as a laser.

The advantage of a transverse thermoelectric heat flux sensor is that the size of the signal depends on the length of the device rather than the thickness, as with normal heat flux sensors. This is because the electric field develops in a direction orthogonal to that of the heat flux. The device can be built with a very small thickness to improve the response time of the signal while maintaining a large signal by increasing the device's length.

Thermoelectric devices can also be used for power generation. The principles are essentially the same as with thermoelectric heat flux sensors, i.e. a temperature difference across the device creates a voltage. There is not much everyday use for thermoelectric power generators because the power gained is far outweighed by the cost of the device. However, in applications where another power source is not readily available but a temperature difference is, thermoelectric power generators can be useful. Such applications could include remote sensors, sensors in enclosed spaces, and even deep space probes. NASA has implemented thermoelectric power generators is several deep space missions, such as Voyager and Cassini [4,5]. These generators are known as

Radioisotope Thermoelectric Generators (RTG) because they use Plutonium-278 as a heat source. As the radioactive substance releases heat energy, the thermoelectric devices convert that energy to electricity for use in the probe. NASA is also working on a device that could be implanted inside the human body and use temperature differences to power health monitoring systems on long manned missions [6]. These types of devices could also be used to power pacemakers.

One can imagine a myriad of other uses for thermoelectric power generators. There are countless instances in industry and transportation where heat is lost to the environment because of the inefficiency of conventional power systems (smokestacks, internal combustion engines, cooling towers, etc.). Thermoelectric devices could be installed to convert some of this waste heat to useable electricity, but at this time the inefficiency of thermoelectric materials prevents this type of application from being economically viable. It is possible that in the future transverse thermoelectric technology may contribute to the improvement of the efficiency of thermoelectric devices, but that is outside the scope of this work.

1.4 Summary and Achievements of the Project

Many achievements were made over the course of this project. The material properties of thermoelectric properties were investigated, techniques for measurements of cooling and heat flux sensing were developed, and a transverse thermoelectric device was designed and constructed. Several obstacles were overcome during the design and testing phases of the project, and several remain to be solved.

The project began with the selection of bulk thermoelectric materials to be used to build a multilayered device. Past studies [7,8,9] suggested that bismuth (Bi) and bismuth telluride (Bi_2Te_3) would be good thermoelectric materials, i.e. they would work well in conjunction to produce a testable transverse device. These materials were obtained and tested for their Seebeck coefficient, the main material property used to characterize thermoelectric materials. Once the materials had been investigated, a device was constructed. Techniques for cutting and connecting the pieces were developed and

improved over the course of several months. The materials were cut with a low speed dicing saw and were ultimately connected using indium film.

Measurement techniques for determining the cooling and heat flux sensing capabilities of the device were developed in a simple yet effective way. For cooling, the device was powered with a DC source and the resulting temperature difference was measured with thermocouples. For heat flux sensing, the device was heated on one side to create a temperature difference (heat flux), and the resulting voltage was measured. All measurements were taken using a DAQ system made of parts from National Instruments® and recorded with a simple LabVIEW® program.

The results of the heat flux sensing tests were compared to predicted values, which were determined from basic theory [10]. The results followed the trend of the predicted values, but the magnitude of the output signal was significantly lower than expected. An analysis of uncertainty and errors followed, and several possibilities were uncovered. It was ultimately determined that the device was indeed displaying transverse thermoelectric effects consistent with expected results, but that certain flaws in the construction and testing process limited the accuracy of the data.

1.5 Thesis Outline

This thesis details the decisions and processes that lead to the creation, testing, and analysis of a transverse thermoelectric device. Chapter 2 outlines the history of thermoelectric research, from the discovery of thermoelectrics in 1822 to current research regarding the search for better thermoelectric materials and the transverse Seebeck effect. Chapter 3 describes the process of constructing and testing the device. Included are discussions of material selection, some early measurements, and a complete description of the test setup. Chapter 4 begins with a discussion of the expected results for heat flux sensing, and then details the actual results from several different tests. The results are then compared to the predicted values, and a discussion of uncertainty and error analysis follows. Finally, Chapter 5 summarizes the results and analysis of testing, and gives several recommendations for future work.

Chapter 2 - Background

2.1 A Brief History of Thermoelectrics

The study of thermoelectrics began in 1822 when Thomas Johann Seebeck [11], a German physicist, noticed that two dissimilar metals in a closed loop caused a compass needle to deflect when the two metals were held at different temperatures. This meant that an electric field was created between the two metals, thus inducing a magnetic field to deflect the needle. Seebeck later discovered that some metals were able to create stronger fields with the same temperature difference, and that the amount of deflection in the needle was proportional to the temperature difference between the two conducting metals. These principles make up the foundations of thermoelectrics, and for his discoveries the Seebeck coefficient (the voltage produced between two points of a conductor where a uniform temperature difference of 1K exists between those two points) was named after the founding father of thermoelectrics.

In 1834 a French watchmaker named Jean Charles Athanase Peltier [12] discovered that thermoelectric materials could also work in reverse. That is, an applied voltage could create a temperature difference between the two dissimilar metals. Although Peltier is generally credited with the discovery of thermoelectric cooling, he did not fully understand the physics of the phenomenon. The full explanation was given four years later by Emil Lenz, who showed that a drop of water on a bismuth-antimony junction would freeze when electrical current was applied one way, and melt again when the current was reversed.

As knowledge of thermoelectrics increased, the most important discoveries were related to material properties. In 1911, Altenkirch [13] derived the thermoelectric efficiency, now known simply as Z, or the thermoelectric figure of merit. This value is given as

$$Z = \frac{S^2 \sigma}{k} \tag{2.1}$$

where S is the Seebeck coefficient, σ is the electrical conductivity, and k is the thermal conductivity. Altenkirch and others realized that ideal thermoelectric materials would have a high electrical conductivity to minimize Joule heating and a low thermal conductivity to prevent the backflow of heat from the hot side to the cool side. The thermoelectric efficiency can be non-dimensionalized by multiplying by the absolute temperature T, which yields the most common form of thermoelectric efficiency, ZT, also known as the dimensionless *figure of merit*.

Early work in thermoelectrics resulted in very small values of Z because the materials being used (mostly metals) did not possess ideal thermoelectric properties. Most traditional materials have a correlation between electrical and thermal conductivity. That is, a material that conducts electricity well, such as a metal, will also conduct heat well, and a material that insulates heat, such as glass or ceramic, also insulates electricity.

Beginning in the late 1930's and continuing into the 1970's, there was a surge of discoveries that showed semiconductors exhibited the best thermoelectric properties. Until then metals such as bismuth and antimony alloys were the state of the art with a ZT value of around 0.1 at room temperature. The implementation of semiconductors such as bismuth telluride (Bi_2Te_3) helped to increase that number by ten fold because semiconductors are moderate conductors of heat and electricity. Figure 2.1 shows a rough approximation of the dependence of thermoelectric properties on carrier concentration. It can be seen in the figure that semiconductors display the largest value of $S^2\sigma$, and they also have moderate values of k. This means that they are the best known thermoelectric materials. The efficiency of modern thermoelectric materials still cannot compete with more conventional methods because the electrical conductivity is too low and the thermal conductivity is too high. A ZT value of roughly 3 is needed in order for thermoelectric cooling systems to compete with vapor compression refrigerators [1].

Recent advancements in nanoscale physics have allowed researchers to begin manipulating materials at the molecular level. This means that new materials may be created that can conduct electricity very well while insulating against heat transfer. This area of research will be discussed in more detail in the next section.

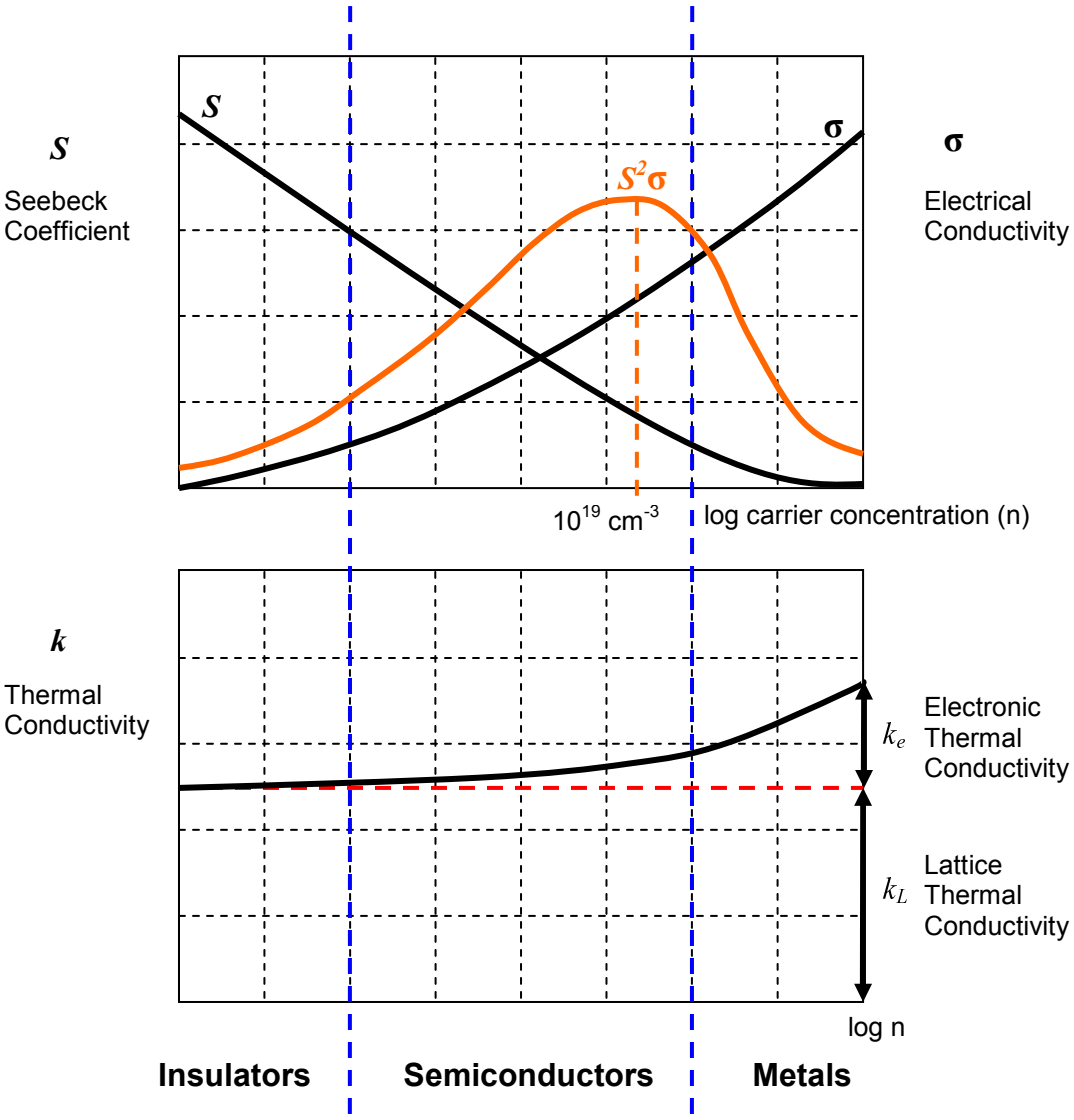

Figure 2.1. A rough sketch of the dependence of *S*, σ, and *k* on the concentration of free carriers. The relatively moderate values of electrical and thermal conductivity make semiconductors the best known thermoelectric materials [14].

2.2 Review of the Applications of Thermoelectrics

Thermoelectric effects can be used in two ways. The first is called the Seebeck effect, and it occurs when a temperature gradient in a material creates a voltage potential by pushing electrons from one side to the other. The Seebeck effect is useful for heat flux sensing, where the signal is proportional to the temperature gradient and thus the

heat flux, and power generation, where a small voltage (enough to run a small motor, sensor, transmitter, etc.) can be generated essentially for free if there is a large enough temperature difference. Thermocouples also operate on the Seebeck effect, by having one junction at a reference temperature and outputting a voltage proportional to the temperature difference between the junctions.

The second method for utilizing thermoelectrics is called the Peltier effect. This effect occurs when a current applied to a material creates a temperature difference. The side that gets cool can be used to actively lower the temperature of electronics or other surfaces. To date, thermoelectric coolers are not in wide-spread use because of their low efficiency. They are solid-state and quiet, require almost no maintenance, and will last indefinitely, but these advantages do not justify the amount of power they consume in most cases (a *ZT* value of 1 corresponds to roughly one third the efficiency of a normal refrigeration cycle [1]). The cost of materials and fabrication for thermoelectric coolers can also be high.

Most commercial coolers use bismuth telluride (Bi_2Te_3), the best known thermoelectric material around room temperature. Alternating legs of p-doped and n-doped Bi_2Te_3 are connected electrically in series and thermally in parallel (Fig. 2.2). In the p-doped legs, positively charged holes carry heat in the same direction as the current flow, and in the n-doped legs, negatively charged electrons carry heat in the opposite direction. The net effect is that heat is carried from the cold side to the hot side in both legs. A commercial cooler is generally constructed of dozens of pairs of legs in a fashion that maximizes cooling per unit area. The amount of doping in the material is optimized and usually results in a maximum *ZT* value of about 1 for Bi_2Te_3.

The applications of thermoelectric technology are somewhat limited due to the efficiency of current materials. Thermoelectric coolers are mostly used in electronic devices where a traditional fan and heat sink may be too loud or take up too much space. The advantage of a thermoelectric device in this case is that it has no moving parts, and so is quiet and requires less maintenance. The device pumps heat from the chip to a heat sink just as a fan does, but uses much more power to remove the same amount of heat. A thermoelectric device may also be used for active temperature control because it can either cool or heat the controlled side, depending on which way the current is flowing.

Thermoelectric devices are also used for power generation in remote locations where a significant temperature gradient is available. For instance, some deep space probes use thermoelectric generators for power when they are too far out for solar energy to be sufficiently available (the generator uses an onboard source of heat provided by radioactive plutonium). These types of generators could also be used to provide power to sensors in remote locations, enclosed spaces, wristwatches, laptop computers, or any other number of devices where a more conventional source of power is not available.

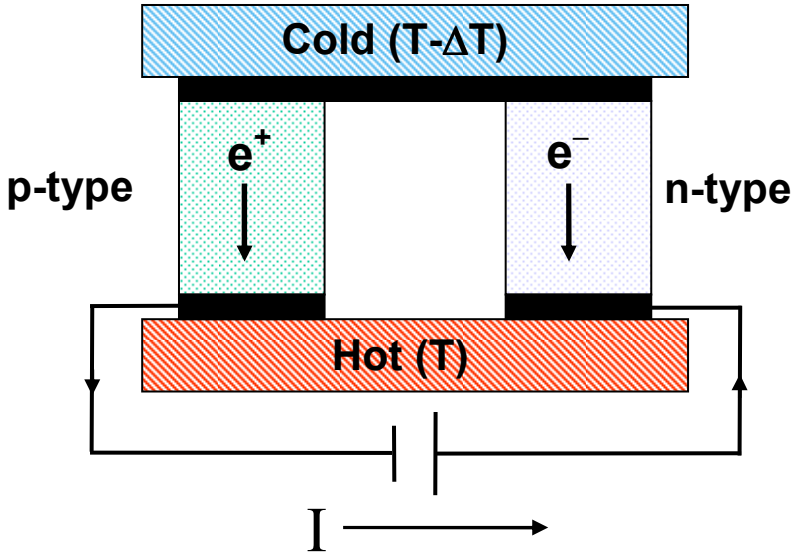

Figure 2.2. One pair of n- and p-type legs in a traditional thermoelectric cooler. The carriers move heat from the cold side to the hot side in both legs.

Recent investigations have resulted in discoveries of different materials that exhibit high ZT values using materials other than Bi_2Te_3. The main challenge in improving thermoelectric materials is that the three relevant properties (electrical conductivity, thermal conductivity, and Seebeck coefficient) are interrelated. The equation for Z dictates that one must maximize S and σ while minimizing k, yet most materials with a high value of σ also have a high value of k.

The basic way to create a material that is a good candidate for thermoelectrics is to confine electrons in one or more dimensions so that the electrical properties can be more easily controlled [15]. If one dimension is smaller than the mean free path of phonons while remaining larger than the mean free path of electrons, then electricity will

pass easily through the material while heat will not (high σ, low k). Such a material would be very thin, in the nanoscale range, and so is not yet perfected. In 2001 Rama Venkatasubramanian *et al*. [1] reported a ZT value of 2.4 using a device made of ultra-thin layers of bismuth telluride and antimony telluride. Such results have not been repeated to date, but the group says they may be able to achieve ZT values of up to 3.5 in the near future. A 2002 study by Yamashita and Tomiyoshi [16] reported more modest improvements with ZT values of around 1.2 using refined doping and annealing methods. Another group [17] uses $(Bi_{0.25}Sb_{0.75})_2Te_3$ and $Bi_2(Se_{0.1}Te_{0.9})_3$ alloys grown on very thin substrates as a miniaturized thermogenerator for radiation sensing and power generation for tiny devices. Here the advantage of using thin materials is the ability to have thousands of junctions instead of only a few dozen. Other studies have shown ZT values of 1.3-1.6 in PbSeTe/PbTe quantum dot superlattice structures [18,19], and ZT values above 5 were predicted for metal-based superlattices with tall barriers at room temperature [20].

The search for more efficient thermoelectric materials continues, and will be spurred by advances in nanotechnology in the future. Another direction for possible improvements to thermoelectric devices is the use of transverse thermoelectric effects.

2.3 The Transverse Seebeck and Peltier Effects

Transverse thermoelectric effects have been studied less extensively than traditional thermoelectric effects, mostly because of limitations in efficiency. Recent work has revealed that newly discovered materials and techniques may increase the viability of transverse thermoelectrics.

The thermoelectric field of any material due to a temperature gradient ∇T can be determined by [10]

$$\mathbf{E} = \mathbf{S} \cdot \nabla T \tag{2.2}$$

where **S** is the Seebeck tensor, which is of the form [10]

$$\mathbf{S} = \begin{bmatrix} S_{\parallel}\cos^2\alpha + S_{\perp}\sin^2\alpha & 0 & \frac{1}{2}\left(S_{\parallel} - S_{\perp}\right)\sin(2\alpha) \\ 0 & S_{\parallel} & 0 \\ \frac{1}{2}\left(S_{\parallel} - S_{\perp}\right)\sin(2\alpha) & 0 & S_{\parallel}\sin^2\alpha + S_{\perp}\cos^2\alpha \end{bmatrix} \tag{2.3}$$

where $S_{\parallel}$ and $S_{\perp}$ are the in-plane and out-of-plane Seebeck coefficients, and α is the angle between the c-axis and the surface normal of the material (Fig. 2.3). If the angle α is either 0º or 90º, then the off-diagonal terms are zero, and the thermoelectric effects are purely traditional. Current thermoelectric cooling technology utilizes this traditional effect, where the electric current and heat are flowing in parallel directions.

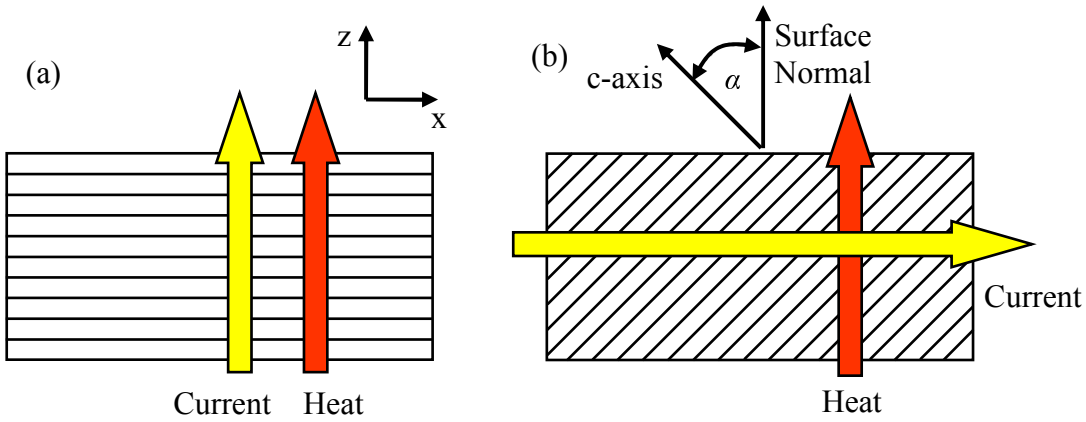

$$\mathbf{S} = \begin{bmatrix} S_{\parallel} & 0 & 0 \\ 0 & S_{\parallel} & 0 \\ 0 & 0 & S_{\perp} \end{bmatrix} \qquad \mathbf{S} = \begin{bmatrix} S_{\parallel}\cos^2\alpha + S_{\perp}\sin^2\alpha & 0 & \frac{1}{2}\left(S_{\parallel} - S_{\perp}\right)\sin(2\alpha) \\ 0 & S_{\parallel} & 0 \\ \frac{1}{2}\left(S_{\parallel} - S_{\perp}\right)\sin(2\alpha) & 0 & S_{\parallel}\sin^2\alpha + S_{\perp}\cos^2\alpha \end{bmatrix}$$

Figure 2.3. The material orientations for (a)traditional and (b)transverse thermoelectric effects. Both orientations follow the same general Seebeck tensor, but the off-diagonal terms are only non-zero when the angle α is between 0º and 90º and the Seebeck coefficient is anisotropic.

If the material is cut so that the angle between the c-axis and the surface normal is between 0º and 90º, the off-diagonal terms will be non-zero and thus contribute to thermoelectric effects. However, the reason that most materials will not exhibit strong transverse thermoelectric behavior is that there must be a significant difference between the in-plane and out-of-plane Seebeck coefficients. In other words, the material must be strongly anisotropic. If such anisotropy exists, then the current and heat will flow in

perpendicular directions. This is particularly advantageous when the device is used as a heat flux sensor. Most heat flux sensors have signal strengths proportional to their thickness, and so response time must be sacrificed for signal strength (because a large thickness results in a slow response time). A transverse thermoelectric heat flux sensor has a signal strength proportional to its length, since that is the direction of electrical current flow. This means that the device can be made as thin as possible to achieve fast response times, and will still have a sufficient signal strength.

2.4 Anisotropy: Intrinsic vs. Artificial

The underlying principle of transverse thermoelectrics is the anisotropy of the material. This results in non-zero off-diagonal terms in the Seebeck tensor, which allows for a transverse voltage. As shown in Figure 2.4, there are two ways to achieve anisotropy in thermoelectric materials. The device may be made of a single material which is intrinsically anisotropic, such as growing single-crystal bismuth, $YBa_2Cu_3O_{7-\delta}$ (YBCO), or some other anisotropic material on a miscut substrate so that the c-axis is at an angle with the surface normal. This results in a thin film device made from one material that exhibits transverse thermoelectric effects. The alternate method is to build a layered device with alternating layers of two materials that have sufficiently differing thermoelectric properties and then cutting the device at the desired angle. The result here is a device which can be considered a single anisotropic material (so long as the dimensions of each layer are small compared with the overall dimensions of the device), and also exhibits transverse effects.

The first type of device (Fig. 2.4a) offers several advantages for practical applications. They can be much thinner for fast-response sensors, and should be easier to mass-produce once their design is perfected. A layered device must be fabricated from alternating layers, and a connection must be made between each layer. This would certainly prove to be more costly than constructing an intrinsically anisotropic device. For experimental purposes a layered device (Fig. 2.4b) is simpler to construct, but requires a method for joining the layers so that they are sufficiently connected

electrically. The interface material or process used here should not contribute significantly to the performance of the device. This type of device may be cheaper to make, and easier to deal with in proof-of-principle studies, but thin films made of intrinsically anisotropic materials are more promising for actual future devices.

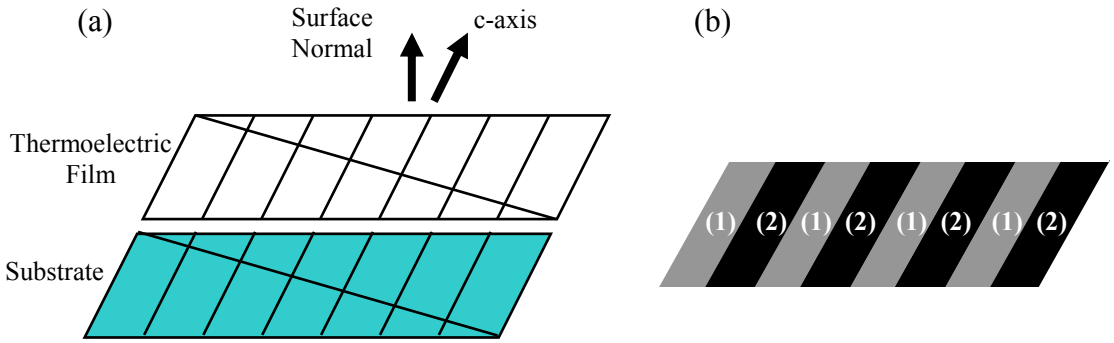

Figure 2.4. The two ways to construct a transverse thermoelectric device are (a) from a single intrinsically anisotropic material grown at an angle on a miscut substrate, and (b) from two dissimilar materials layered at an angle to simulate an intrinsically anisotropic material.

2.5 The History of Transverse Thermoelectric Studies

The transverse Seebeck effect was first discovered by Lord Kelvin in the 19th century [21] when he noticed that anisotropic materials exhibit thermoelectric fields in a perpendicular direction to applied temperature gradients. Research in the area of transverse thermoelectrics began growing steadily in the early 1970's with many studies coming from the former Soviet Union. These studies were mostly geared towards using transverse thermoelectric devices for power generation using waste heat, but a few were also focused on using these devices for cooling.

Early studies focused on the anisotropy of semiconductors such as Bi_2Te_3 and $CrSi_2$ [22] found that certain materials had strongly anisotropic thermoelectric properties. A study by Korolyuk *et al*. [23] used homogeneous thermoelectrically anisotropic thermoelements for power generation as well as measurement of current, voltage, or power. A current was applied to the device and converted to a temperature difference, which was then converted back to a voltage which can be measured. This method was

proposed because of its high accuracy and independence of the form of the input signal. The same study also showed that for a thermoelement with an anisotropic Seebeck tensor independent of temperature and a linear temperature distribution though the element, the resulting emf is proportional to a/b where a is the length of the thermoelement and b is the width (the direction of the temperature gradient). This is important when considering a transverse device for the measurement of heat flux, because the device has a larger output when the dimension perpendicular to the heat flux is large, rather than the dimension parallel to the heat flux as in traditional thermoelectric sensors.

While some work focused on the anisotropic thermoelectric properties of homogeneous materials, some groups decided to construct heterogeneous devices made of alternating layers to simulate a homogeneous material. Babin *et al*. [9] did such a study in 1974 with the goal of theorizing a heterogeneous device with better thermoelectric properties than those of homogeneous thermoelectric materials. The layered device (Fig. 2.5) was considered to be comparable to a homogeneous material if the thickness of each individual layer was small compared to the length of the device. The theoretical work chose to consider the two layers to be a semiconductor and a metal because the large difference in the thermoelectric properties of these two types of material causes the overall properties of the device to be strongly anisotropic. Specifically, a semiconductor would have a large Seebeck coefficient and moderate electrical and thermal conductivities while the metal would have a small Seebeck coefficient and large electrical and thermal conductivities. The authors concluded that the device did display better characteristics than a thermoelectrically anisotropic single crystal. However, it was also deduced that this type of device (a transverse device constructed of alternating layers of a semiconductor and metal at an angle α) cannot exceed the ZT value of a traditional thermoelectric device constructed of the same materials because of circulation currents within the device. These "eddy currents" were also studied by Samoĭlovich and Snarskiĭ [24], who confirmed that they can contribute significantly to the generalized equation of heat conduction pertaining to transverse thermoelectric devices.

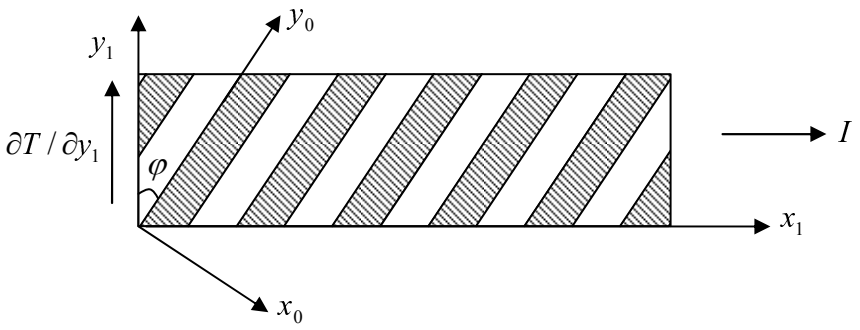

Figure 2.5. The device proposed by Babin *et al*. in Ref. 9. The individual layers are assumed to be isotropic, and the device can be regarded as a homogeneous anisotropic material if the thickness of each layer is small compared with the total length of the device.

In 1977 Gudkin *et al*. [8] carried out an experimental study to confirm the findings of Babin *et al*. [9]. A device was constructed with alternating layers of Bi and $Bi_{0.5}Sb_{1.5}Te_3$, and tested to show its cooling capabilities. The components were chosen to maximize the quantity

$$Z_{xy} = \frac{S_{xy}^2 \sigma_{xx}}{k_{yy}} \tag{2.4}$$

where σ_{xx} is the electrical conductivity in the direction of current flow, k_{yy} is the thermal conductivity in the direction of heat flow, and S_{xy} is the off-diagonal term from the Seebeck tensor (see Eqn. 2.3). This can then be compared to the Z value of a traditional cooler whose legs are made with the same two materials,

$$Z_{1-2} = \frac{\left(S_1 - S_2\right)^2}{\left(\sqrt{k_1/\sigma_1} + \sqrt{k_2/\sigma_2}\right)^2} \tag{2.5}$$

where the subscripts 1 and 2 indicate the properties of the two constituents of the device. The materials making up the transverse device must maximize $Z_{1\text{-}2}$ and the ratio $k_2\sigma_2$ / $k_1\sigma_1$ in order to be effective, and the two materials chosen in this study resulted in acceptable values of $Z_{1\text{-}2} = 0.85 \times 10^{-3}$ K^{-1} and $k_2\sigma_2$ / $k_1\sigma_1 = 60$. This study also claims

that the optimum angle between the layers and the surface normal is 60°, although no mathematical reason is given (a discussion of the effect of angle on device properties will follow later in this chapter). At the optimum current density, the temperature drop across the device was reported to be more than 23º C. An earlier study by Gudkin *et al*. [25] shows the possibility of using "cascaded" devices of arbitrary shape to aid cooling by changing the relative areas of the cold and hot sides of the device.

Additional work in the late 1970's addressed other issues, such as utilizing transverse coolers in a magnetic field [26] and the more subtle effects of the anisotropy of thermoelectric properties [27-30]. In 1978 Gorya and Lupashko [31] confirmed the earlier theoretical work by Babin *et al*. that suggested an artificially anisotropic device could exhibit better thermoelectric performance than an anisotropic thermoelement made from a single-crystal material.

Once the basic principles of transverse thermoelectric effects had been thoroughly investigated, research in the area began to die down. But in the early 1990's, some researchers began to realize that new methods and technologies could be beneficial to the field of transverse thermoelectrics, and the amount of research began to increase. As was discussed earlier, the ideal thermoelectric material has high values of the Seebeck coefficient and electrical conductivity, and a low thermal conductivity. With the introduction of nanoscale processes and material manipulation, researchers saw that certain materials, mainly superconductors, could be arranged in a way that was advantageous to thermoelectrics. A paper from 1991 by Lengfeller *et al*. [32] showed that a thin film of superconducting $YBa_2Cu_3O_{7-\delta}$ (YBCO) produced large voltages in the transverse direction when subjected to heat flux from a laser pulse. These types of large voltages were reproduced by Testardi in 1993 [33]. Lengfeller *et al*. [32] concluded that the large voltages were due to non-zero off-diagonal terms in the Seebeck tensor, i.e. the transverse Seebeck effect. Lengfeller's group had originally thought that the abnormally large voltage was due to a combination of effects including tensorial photoelectric effects and piezo- and pyroelectricity. The superconductor was oriented with the c-axis at an angle of up to 20º from the surface normal to produce varying magnitudes in the output signal, and in fact it was concluded that the signal was directly proportional to the angle at which the film was grown. Lengfeller *et al*. [32] suggested that this new type of device

would be useful as a radiative heat flux sensor which would be almost wavelength-independent around room temperature.

Several other studies of superconductors were conducted during that time period, including studies related to the fast time response of YBCO films [34] and the equally promising transverse thermoelectric properties of $Bi_2Sr_2CaCu_2O_8$ films [35,36] and many other types of superconductors [37].

Another interesting direction that this area took in the late 1990's was in the field of conducting polymers. Mateeva *et al*. [38] described a way to make flexible material from conducting polymers such as polyaniline and polypyrrole that exhibit transverse thermoelectric effects. These types of materials are easily made anisotropic by stretching or spin-coating, but at the time of the study only exhibited ZT values of around 10^{-3}. The paper suggested, however, that future materials could conceivably have much higher values of electrical conductivity and therefore much better thermoelectric efficiency. The problem with the material used in the study was that there was an "internal short-circuiting" of the transverse Seebeck effect because the two types of carriers seem to cancel each other out. If conducting polymers ever become viable candidates for transverse thermoelectric devices, they would be useful in many applications, especially in the medical field, where a flexible bandage-like material could be constructed and serve as a splint device while also heating or cooling.

Transverse thermoelectric effects can also be observed in artificially anisotropic devices. A study by Zahner *et al*. in 1998 [10] used a metallic multilayer structure composed of alternating layers of thin films of copper and constantan. The stack was cut at an angle to produce a transverse device, and a correlation was found between the angle and the signal produced by the device when irradiated with a laser. The group concluded that the artificial structure exhibited the same type of response as YBCO and other superconducting films. A follow-up study in 2004 [39] presented more results from the copper-constantan type of device and determined that the device would be useful for laser sensing. Studies have also been done on intrinsically anisotropic materials other than superconductors. Cho *et al*. [40] constructed thin films of Bi and BiSb alloy on CdTe substrates cut at an angle of about 19°.

2.6 Summary

Thermoelectrics have been around for almost 200 years, but still are not in widespread use because of their poor thermodynamic efficiency. Research in the middle of the 20th century revealed that semiconductors had favorable properties for thermoelectrics, and interest was renewed in the field. Current work shows that some promising materials may soon be able to be competitive with conventional cooling methods.

The field of transverse thermoelectrics has evolved into a search for materials which have properties that maximize the value of *ZT*. Research began with materials such as bismuth and antimony alloys and moved later into superconductors and multilayered structures. The goal is to develop a device that produces a high signal in heat flux sensing and power generation applications, and a high temperature gradient in cooling applications. Many researchers are optimistic that in the future there will be materials that can eventually compete in efficiency with more conventional refrigeration methods. A device which utilizes transverse thermoelectric effects and has high efficiency would almost certainly become a popular method for cooling electronics, because the small size, localized cooling, and solid state operation of thin film devices would be advantageous in that area.

Chapter 3 – Construction of the Device and Test Procedures

This chapter outlines the decisions and procedures that led up to the construction of the transverse device. As stated in the previous chapter, a transverse device can be constructed either with an intrinsically anisotropic material grown at an angle or it can be made from alternating layers of differing materials to simulate anisotropy. The latter method was chosen because it was determined to be a simpler method for obtaining a device to be used for proof-of-principle purposes. The goal was to make a device that could exhibit transverse effects, and use the knowledge gained from that experience to later go on to more practical devices.

3.1 Material Selection

Previous researchers that have constructed artificially anisotropic transverse thermoelectric devices have chosen to use already proven thermoelectric materials like Bi and $Bi_{0.5}Sb_{1.5}Te_3$ [7,8], or metals with weaker thermoelectric properties like copper and constantan [10]. It was decided that for this study, proven thermoelectric materials would be better because they result in more measurable thermoelectric effects. A sample of bismuth telluride was obtained and it was determined that this material would be suitable for the semiconductor material. The second material needed to have significantly different thermoelectric properties than the first in order to create a large anisotropic effect. It was decided that bismuth would be the best choice because it is a metal, and because it was used in previous studies along with a semiconductor to create transverse devices [7,8]. The thermoelectric properties of bismuth and bismuth telluride are shown in Table 3.1.

Table 3.1. Thermoelectric properties of bismuth (Bi) and bismuth telluride (Bi_2Te_3) [37]. (* Measured)

Material	Electrical Conductivity, $\sigma\ (1/\Omega m)$	Thermal Conductivity, $k\ (W/mK)$	Seebeck Coefficient, S $(\mu V/K)$
Bi	9×10^5	8.0	34.5*
Bi_2Te_3 (N)	2.11×10^4	1.8	190*

3.2 Early Measurements

Before construction of the device began, early measurements were taken to determine the thermoelectric properties of the bismuth telluride samples. These early tests helped to develop techniques for measuring thermoelectric capabilities of the device itself, but eventually proved to be not useful in the characterization of the bismuth telluride.

3.2.1 Experimental Setup and Components

Figure 3.1 shows the experimental setup used to measure the thermoelectric characteristics of the bismuth telluride. A current was simply passed through the material, and the resulting temperature difference across the material was measured with thermocouples. The electrical leads were connected using high purity silver paint from SPI® because it was easy to implement and formed a good electrical connection. It was determined that normal solder would not work as well because it would not form a good connection with the surface of the bismuth telluride. Type K thermocouples were used to measure temperature, and were read using a National Instruments® SC-2345 Signal Conditioning Connector Block and SCC-TC01 Thermocouple input modules, and a PCI-6221 M Series Multifunction DAQ card, also from National Instruments®. The bismuth telluride was attached to the heat sink using AOS® Heat Sink Compound, a thermal paste, to aid in heat transfer and isolate the sample electrically from the aluminum heat sink. The device was powered with an Agilent® E3644A power supply.

A heat sink must be used when performing this kind of test because the Joule heating inside the sample due to the electric current can make the sample temperature rise rapidly without a means of heat removal. One side of the sample was placed on the heat sink and the other side was placed on a foam block for support. It was anticipated that one side of the sample would get hot while the other got cool, just as with a commercial thermoelectric cooler. There was indeed a temperature difference between the two sides, but neither side reached a temperature below room temperature, and if the direction of electrical current was reversed, the direction of the temperature difference remained the same. It was therefore determined that the temperature difference was only due to one side being on the heat sink and the other not. The Joule heating created an internal heat source in the sample, and the side on the heat sink rose in temperature less rapidly than the other side.

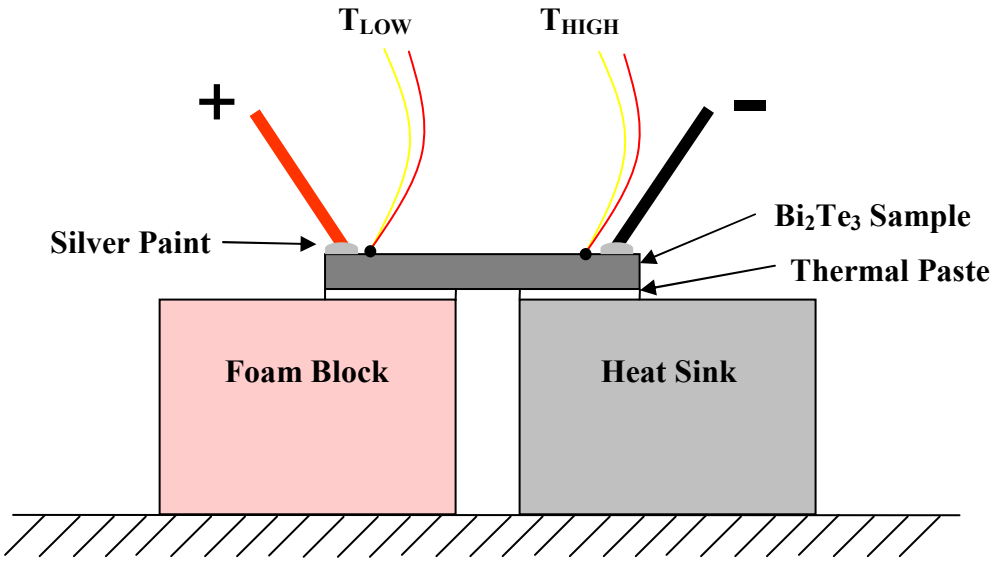

Figure 3.1. Experimental setup used to measure cooling effects from bismuth telluride sample.

3.2.2 Thermoelectric Cooling Capabilities of Bi_2Te_3 Samples

The testing procedures for determining the cooling effects of the bismuth telluride were fairly simple. The sample was powered at a constant current until a steady state was reached. The DAQ system then recorded temperature data for about 30 seconds. These

data were then averaged over the 30 second time period and the final result was two temperatures corresponding to one input current. The expected result for this type of test would be something like Figure 3.2, which shows the cooling characteristic chart for a commercial cooler built by Marlow®. In this chart one can see that a larger amount of current supplied to the device results in a larger temperature difference. In this case the temperature difference indicates cooling, i.e. the hot side was held at room temperature. At about 3.6 A the cooling starts to decrease because Joule heating produces too much excess heat, which begins to flow more rapidly back toward the cool side of the device.

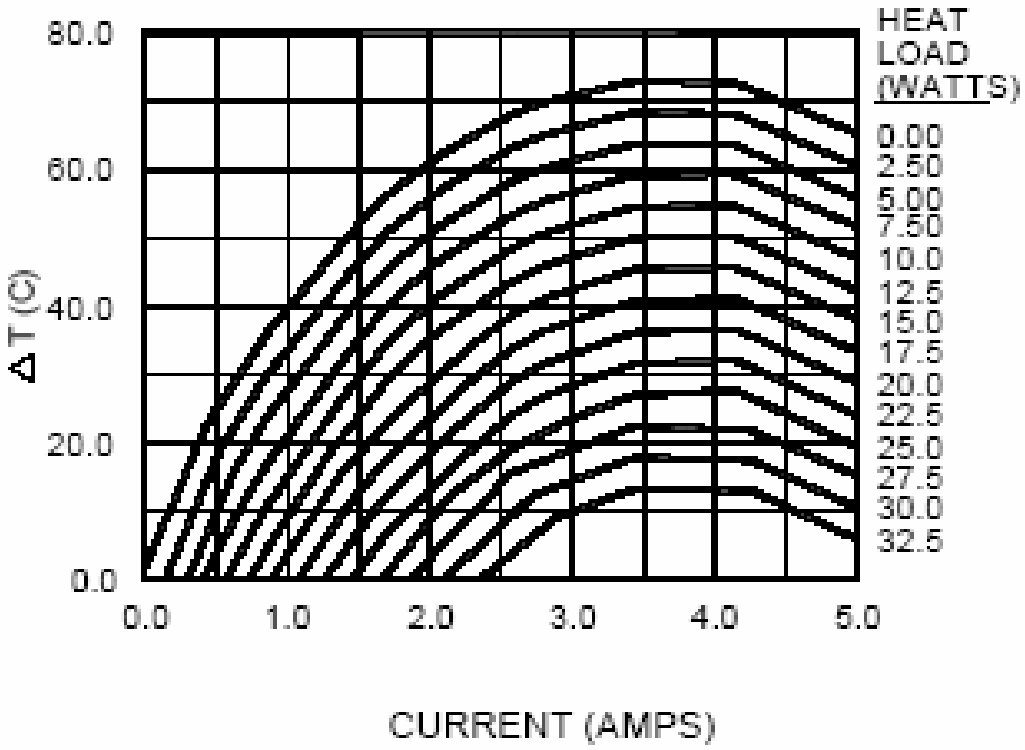

Figure 3.2. The cooling characteristics of Marlow® model #DT12-4 thermoelectric cooler (adapted from www.marlow.com)

In contrast to the expected result, Figure 3.3 shows some steady state results for the bismuth telluride sample. The sample did not show cooling, although there was a temperature difference because of the aforementioned reasons. The graph does not seem to have the same shape as the Marlow® chart either, but this may be because the maximum current is much larger than 1.25 A, which was the largest current tested.

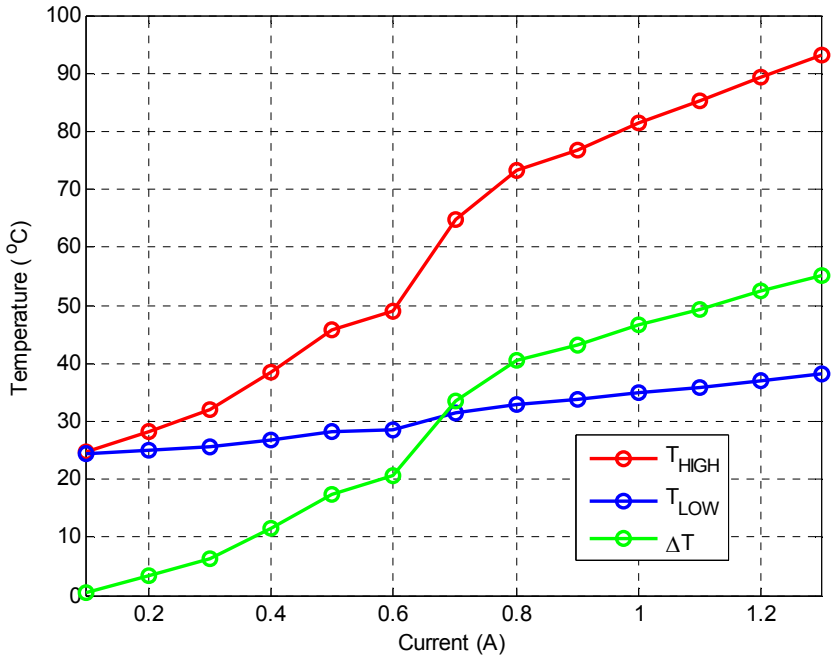

Figure 3.3. The results of steady state cooling tests on the sample of bismuth telluride. Cooling is not present although there is a temperature difference due to the heat sink.

3.2.3 Heat Flux Sensing Capabilities of Bi_2Te_3 Samples

The bismuth telluride sample was then tested for its heat flux sensing capabilities. The setup for this test is shown in Figure 3.4. One side of the sample was placed on a heater (a ¼" cartridge heater encased in a rectangular steel sleeve) and the other side was exposed to room temperature air. The voltage across the sample in the same direction of the heat flux was measured along with the temperature of each side, and the resulting Seebeck coefficient was recorded ($S = V/\Delta T$). This preliminary testing resulted in a Seebeck coefficient of around 200 μV/K, which is in good agreement with published values [14]. An example of results of the preliminary testing can be seen in Figure 3.5. Another test was performed later, when the techniques had been somewhat refined. The Seebeck coefficients of the bismuth and bismuth telluride samples were found to be 34.5 μV / K and 190 μV / K, respectively.

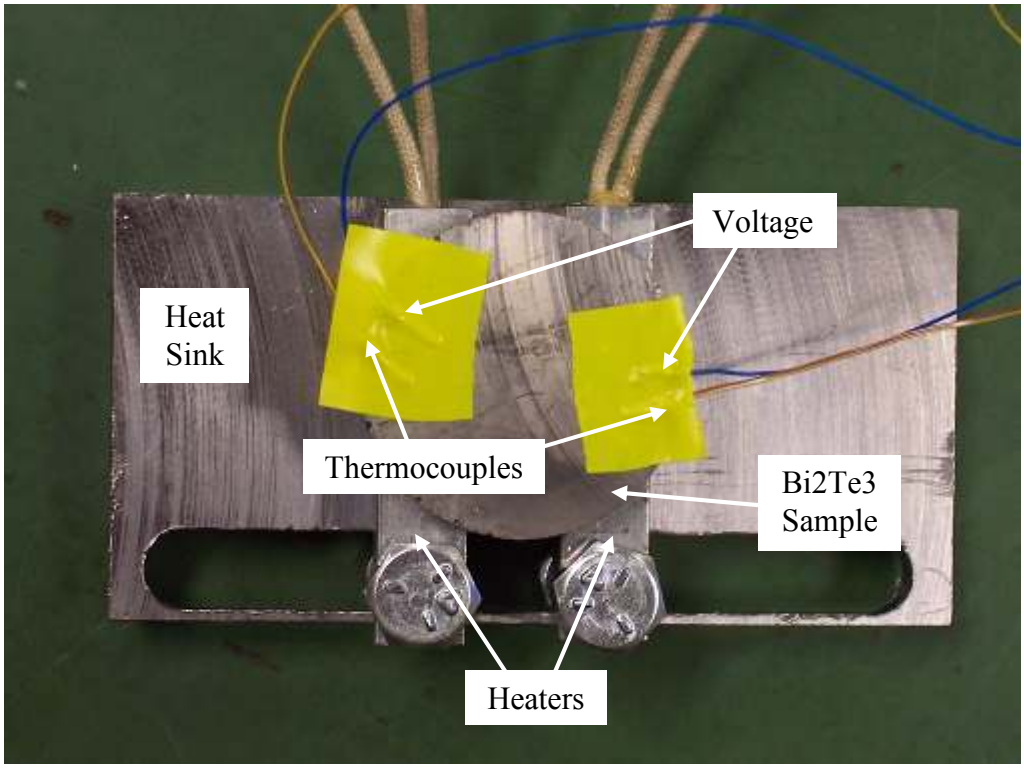

Figure 3.4. The setup for measuring the Seebeck coefficient of the bismuth telluride sample.

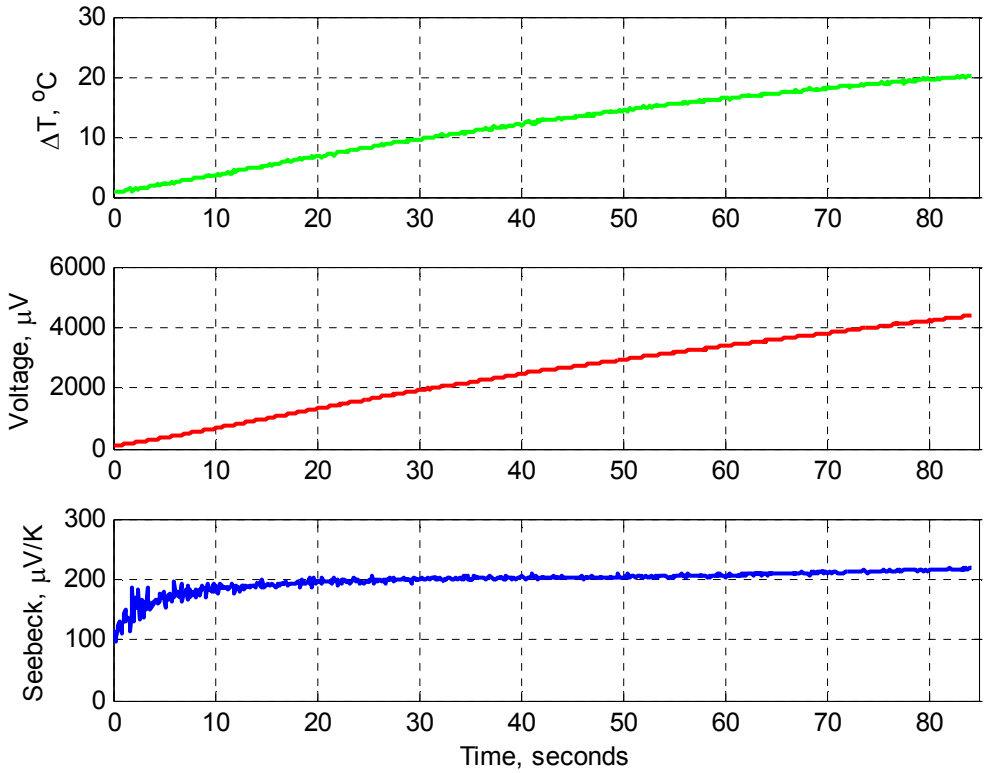

Figure 3.5. Sample data from Seebeck measurements on the Bi_2Te_3 sample.

3.3 Construction of the Device

Once the techniques for testing and characterizing a thermoelectric device had been developed, the design and construction of the artificially anisotropic device began. The device was meant to show the basic principles of transverse thermoelectrics, and was designed to be easy to construct and manipulate. This section details the process of constructing the transverse device.

3.3.1 Construction of Material Layers

Many things had to be considered when designing the transverse device. The materials must be significantly different to create artificial anisotropy, the contacts must be made to minimize electrical resistance between the layers, and it must be possible to test the device at many different angles. As discussed earlier the materials chosen for this project were bismuth and bismuth telluride, partly because of the precedent set by earlier studies and partly because the thermoelectric properties were determined to be sufficiently different. It was decided that the best way to cut the material into appropriately sized pieces would be with a dicing saw. The process was time consuming but effective, as the pieces had smooth interfaces and a consistent size. The original materials used were bars of bismuth (0.5" diameter × 4" length) from Alfa Aesar® and disks of bismuth telluride (1.35" diameter × 0.198" thickness) from Marlow®. The geometry and cutting process of the pieces is outlined in Figure 3.6.

An important thing to consider when concerned about the anisotropy of the device is the anisotropy of the individual materials. Bismuth is an intrinsically anisotropic material, but the particular sample used in this project was not single crystal. It was simply pure bismuth melted into a bar shape, and so the crystal planes were randomly arranged (amorphous). The bismuth telluride samples were obtained from a commercial thermoelectric cooler manufacturing company and were single crystal. One early concern was that it could be difficult to align the layers of the device so that the properties in each layer would be consistent. If some layers were aligned so that the crystal planes were not in the same direction as in other layers, the properties of the

device would not be consistent from layer to layer. It was determined that the cutting process assured that the layers would be consistent with each other because the cuts were made in a direction parallel to the crystal planes.

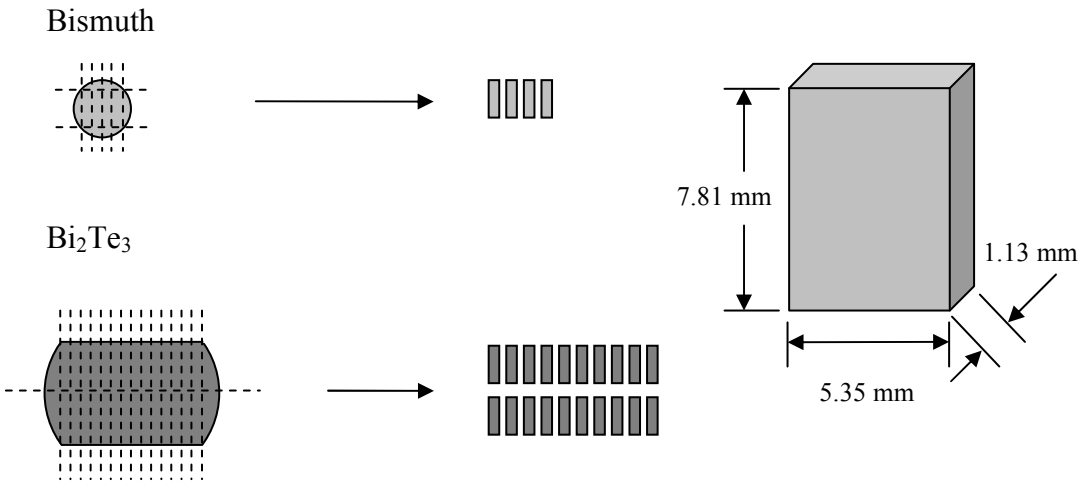

Figure 3.6. An overview of the geometry and cutting process used to make the device layers. The bismuth and bismuth telluride samples were cut into equally sized slabs using a Buehler Isomet® low speed saw.

3.3.2 Interface Materials

Once the layers of material were cut, they had to be joined by choosing an interface material that would hold the pieces together while providing a good electrical connection. The first interface material to be tested was conductive carbon paint from SPI® because it was fairly easy to use and could be removed with acetone in order to take the device apart and put it back together at a new angle. To construct the device, the layers were simply coated with the carbon paint, pressed together at a chosen angle, and then allowed to dry. The excess carbon paint was then scraped off the sides of the device to avoid electrical shorts. Carbon paint was also used to connect wires to the ends of the device for supplying power or reading voltage. The device was tested for cooling and heat flux sensing in a similar manner as the bismuth telluride samples (Fig. 3.7, 3.8). It also did not show any cooling, but did show the ability to sense a heat flux, although the results were not particularly satisfactory.

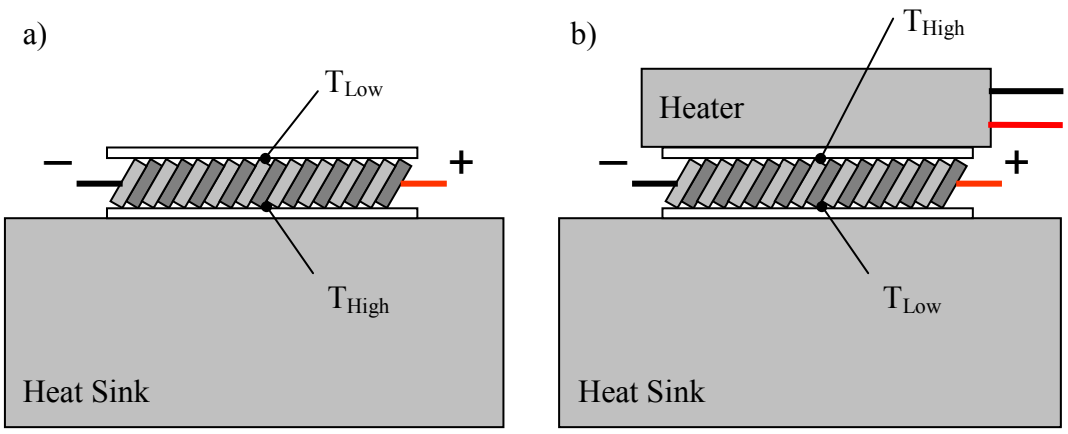

Figure 3.7. The experimental setup for testing the device for a) cooling and b) heat flux sensing.

The results of the cooling and heat flux sensing tests are shown in Figures 3.9, 3.10, and 3.11. Figure 3.9 shows steady state tests in which the device was powered with a DC source and the temperature of the top and bottom sides of the device were recorded. Each point on the graph shows one steady state test and the two lines correspond to two days of testing. One side of the device was on a heat sink, and it was determined that this was the cause for the temperature difference rather than thermoelectric effects, because when the direction of electrical current was switched, the temperatures of the two sides were not affected. Figure 3.10 shows a transient heat flux sensing test in which the device was heated on one side while the other side was on a heat sink to create a temperature difference across the device. The temperature at each side was recorded, as was the resulting voltage induced along the length of the device (in the direction perpendicular to the temperature difference). The voltage follows the temperature difference well, although it is not smooth.

Figure 3.11 shows steady state heat flux sensing tests. Again, each point represents a steady state test, and the five lines correspond to five days of testing. This test indicated that there was some sort of problem with either the testing methods or the device itself, because the tests are significantly inconsistent from day to day. It was thought that the fan attached to the heat sink was providing too much interference by increasing convection along the sides of the device, but tests with and without the fan all show the same inconsistencies. The resistance of the device from end to end was around 12 ohms (the theoretical resistance was less than 1 ohm), and it was thought that this high

value of resistance might be affecting the cooling and heat flux sensing capabilities of the device.

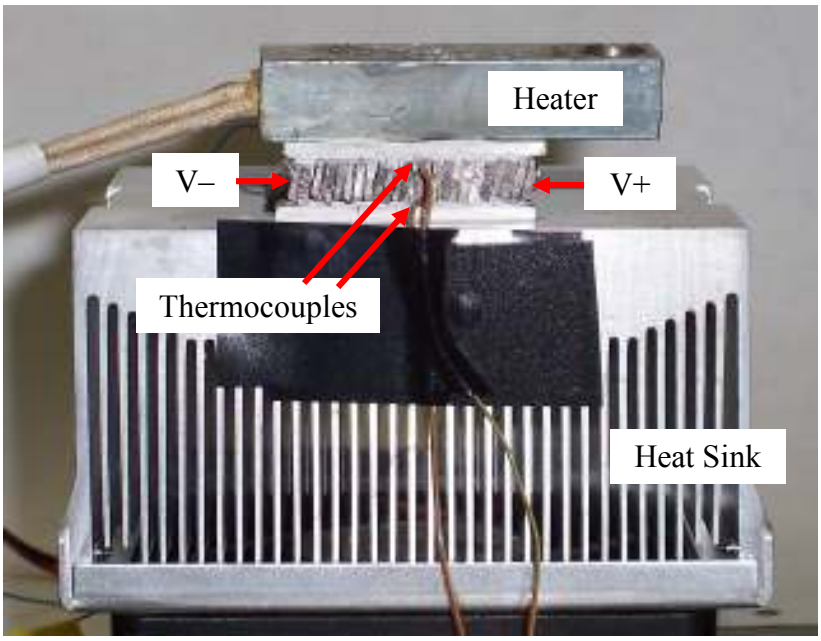

Figure 3.8. Photo of test setup used for measuring the heat flux sensing capabilities of the device.

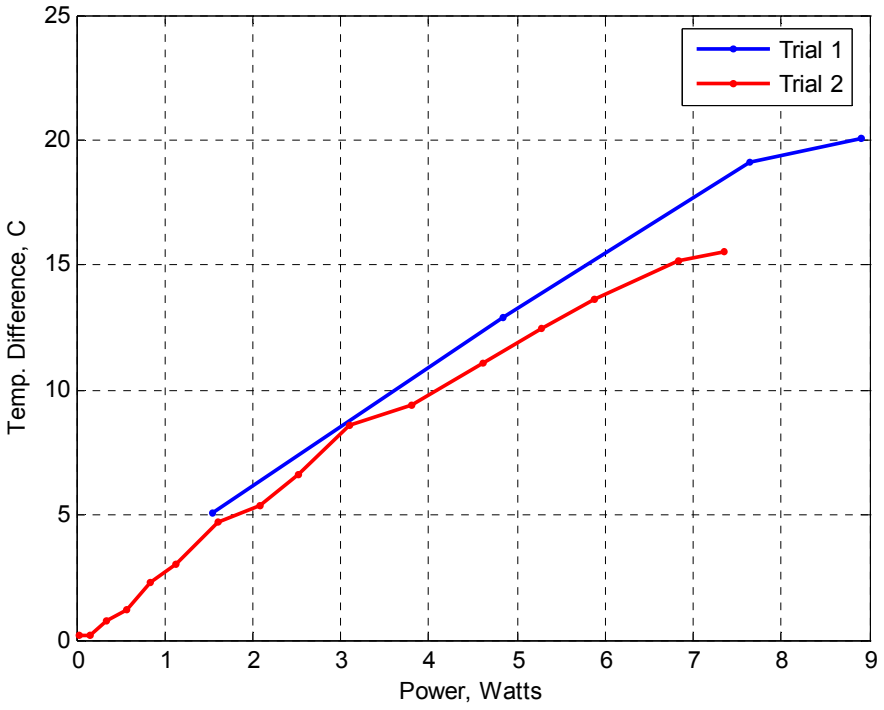

Figure 3.9. Steady state cooling tests with the device made with carbon paint. The two lines correspond to two days of testing.

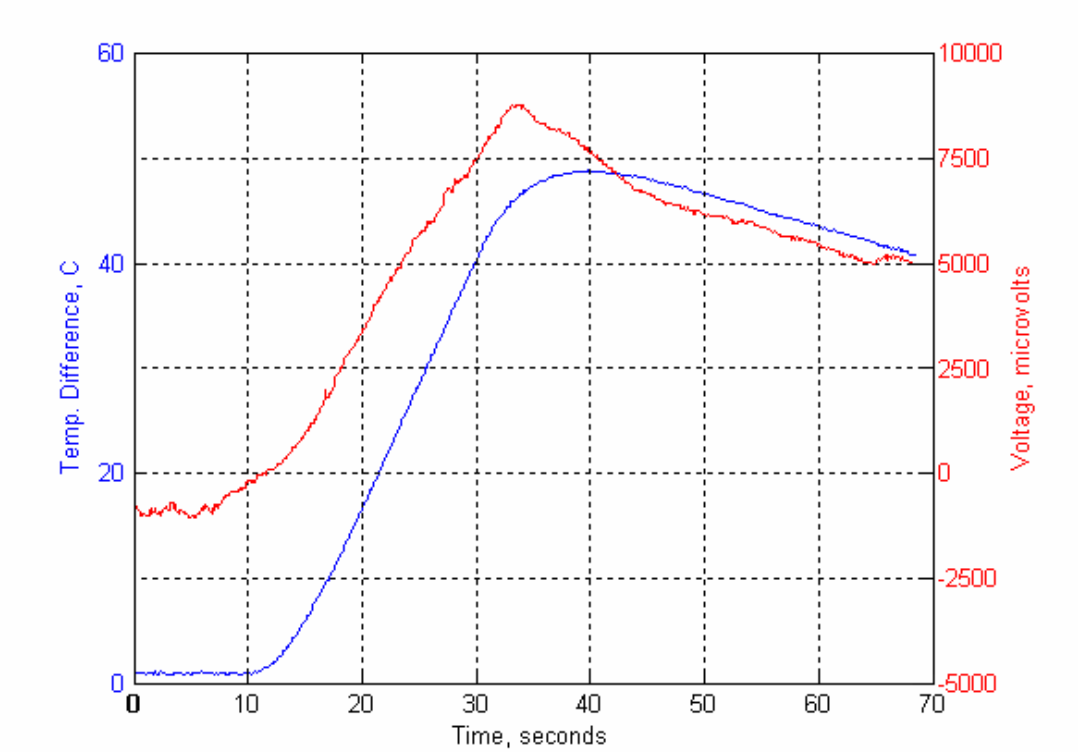

Figure 3.10. Transient heat flux sensing test of the device made with carbon paint.

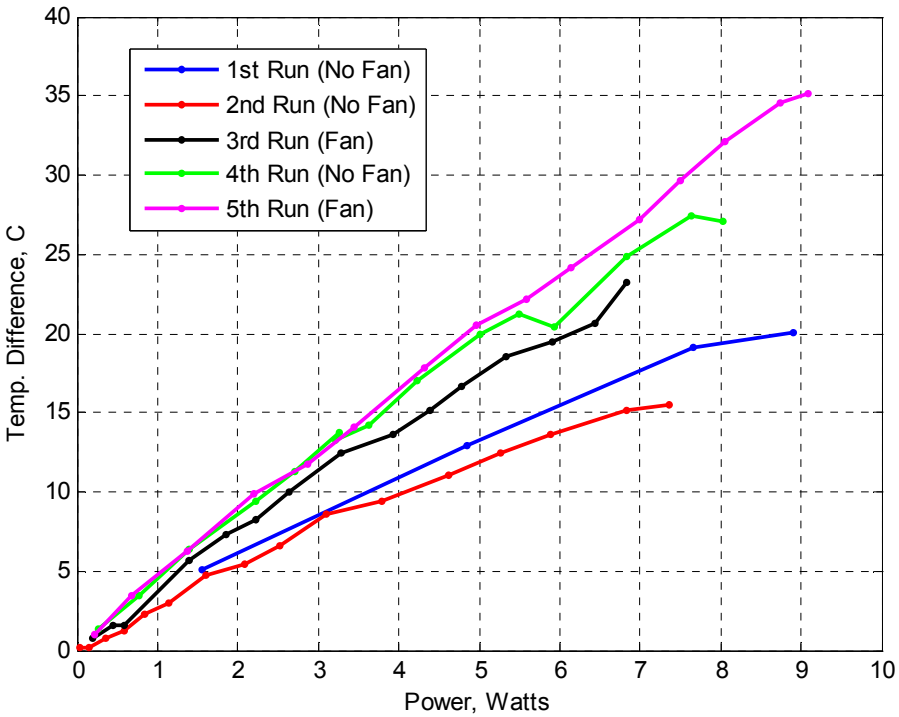

Figure 3.11. Steady state heat flux sensing tests with the device made with carbon paint. The lines correspond to tests on different days.

A new interface material, high purity silver paint from SPI®, was chosen because it also was easy to use and remove. The device was constructed in the same manner as before, and tested in the same way. The internal resistance was about the same (about 12 ohms), and the results of testing were also similar. The device still did not exhibit cooling, but showed capabilities as a heat flux sensor, just as before. Some example results of heat flux sensing measurements using the device made with silver paint are shown in Figure 3.12.

The testing still indicated that there were large differences in the data between one day and the next, as seen in Figure 3.11. It was decided that a new interface material may result in better data. The next material, and the one ultimately chosen to continue testing with, was indium film from Indium Corporation of America®. This material was more difficult to apply to the bismuth and bismuth telluride layers, but resulted in a much lower internal resistance and also held the layers together more strongly.

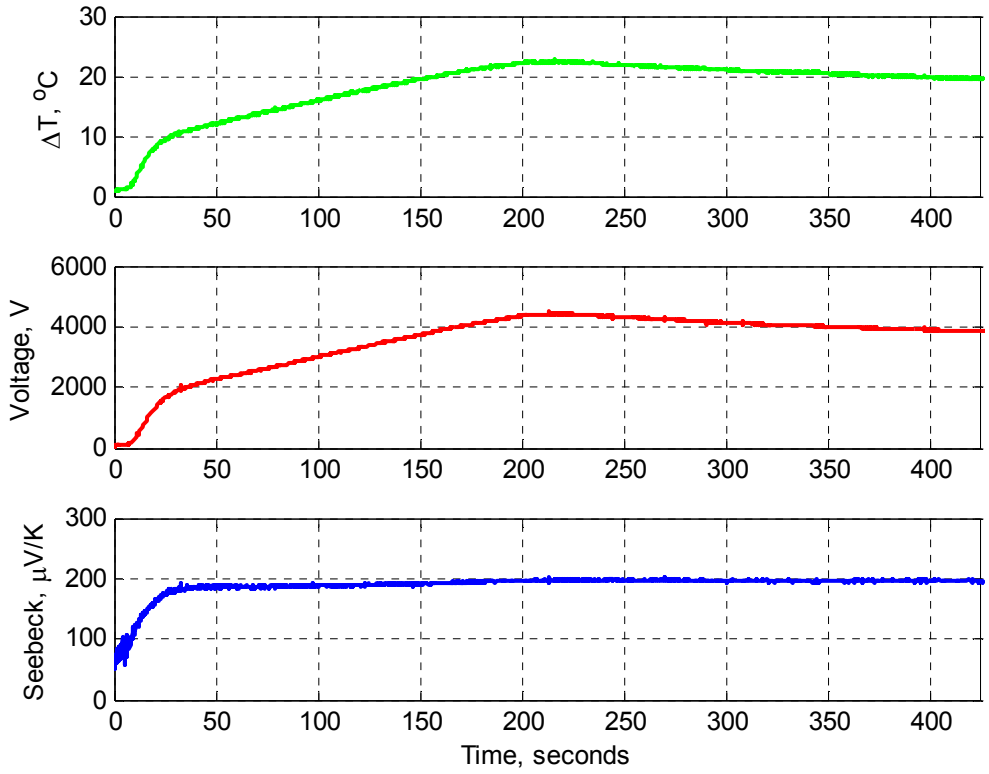

Figure 3.12. Sample data from Seebeck measurements on the device constructed with silver paint.

The method for implementing the indium film is outlined in Figure 3.13. The film has a melting point of 157 ºC, so once it was layered in between the bismuth and bismuth telluride pieces along with flux to aid in bonding, the device was heated to around 160-170 ºC using a cartridge heater. The excess indium seeped out of the sides of the device and was removed to prevent electrical shorts across the layers, and the device was allowed to cool. The end product was a layered device with better contacts than before (internal resistance less than 1 Ω) that was also structurally stronger. Figure 3.13 also shows the process of changing the angle, which simply consisted of heating the device above 157 ºC and moving the pieces to a new angle using a foam block cut to the desired angle. This process worked well, although an unforeseen side effect was that the bismuth slices experienced some localized melting. The melting temperature of bismuth is 271.3 ºC, but some bismuth did appear to melt. The implications of this along with other possible errors will be discussed in later chapters. The results of measurements taken from the device made with indium film can be found in the next chapter.

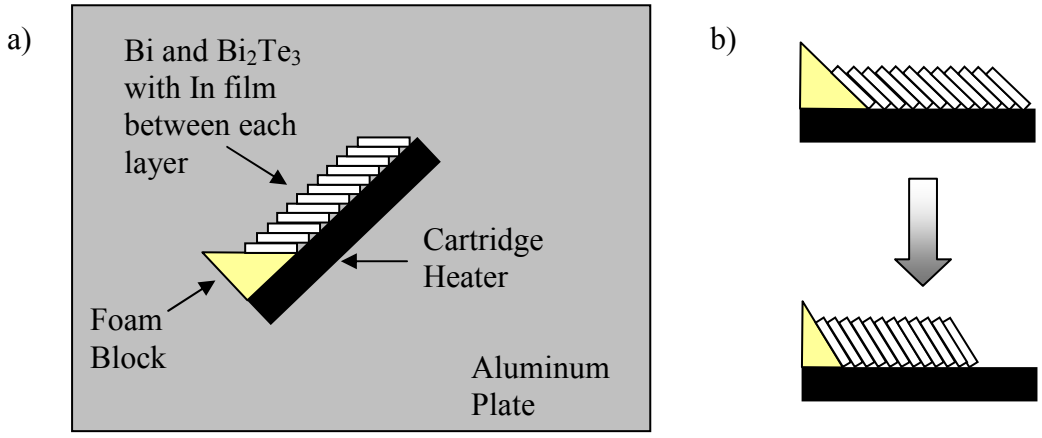

Figure 3.13. The processes for (a) constructing the initial device and (b) changing the angle of the device. In (a), the pieces were kept flat so that the indium melted uniformly between the pieces.

Even with the drastically lowered value of resistance, the device with indium interface connections still did not exhibit cooling as expected. It is assumed that there is some problem with the materials themselves that prevents the device from cooling, and the remainder of this report will focus on characterizing the device as a heat flux sensor.

3.4 Test Setup and Procedures

Once the device had been built, it was tested extensively for its heat flux sensing capabilities. This section outlines the procedures used to perform these tests, and the adjustments that were made as errors in testing became evident. The procedures for collecting data were much the same as in earlier tests, but are discussed in more detail. Many corrections and adjustments were made along the way, and those are described in detail as well.

3.4.1 Initial Test Setup

The test setup for measuring heat flux sensing capabilities was fairly straightforward, and is shown in Figure 3.14. A heat flux was applied to one side of the device with a cartridge heater in a steel sleeve while the other side of the device was connected to a heat sink. The resulting temperature gradient through the device created a voltage in the transverse direction. The top and bottom of the device were isolated electrically from the heater and sink using AOS® heat sink compound and boron nitride ceramic tiles. Type K thermocouples were used to measure temperature on the top and bottom surfaces of the device, and wire leads were connected to the ends with SPI® high purity silver paint to measure the voltage produced by the device. The temperature and voltage data was read with a DAQ system consisting of NI® parts.

The voltage wires and thermocouples were attached to signal conditioning modules (SCC-AI07 and SCC-TC02) that are specifically designed to handle the small voltages involved. These modules were attached in the SC-2345 Signal Conditioning Connector Block, which collected the data and sent it to the PCI-6221 M Series Multifunction DAQ card in the desktop computer. LabVIEW® was used to record the data, and MS Excel® and MatLab® were used to analyze it.

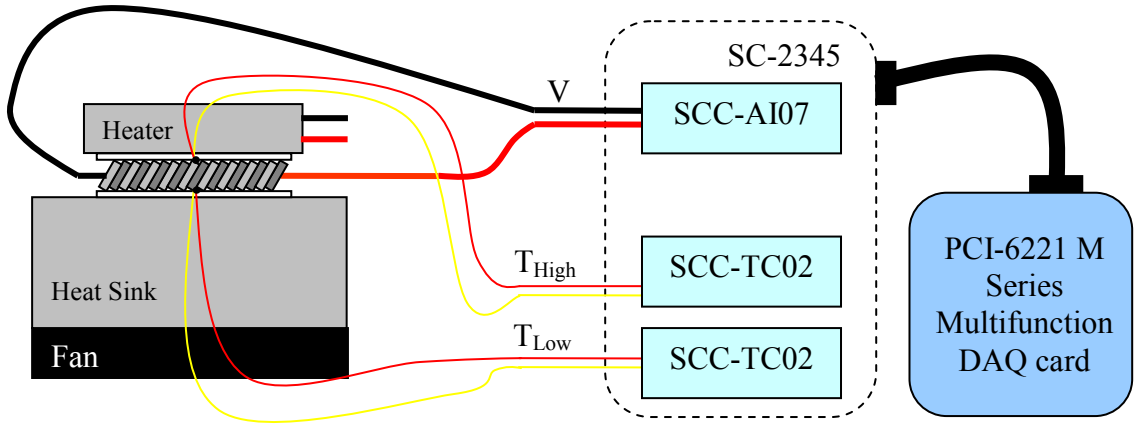

Figure 3.14. Schematic of the initial setup for measuring heat flux sensing capabilities.

The characterization of the device consisted of steady state measurements. The heater was turned on to a chosen power level and the setup was left to reach steady state. The initial requirements used to determine when steady state was reached were not stringent enough, and this is discussed in the next section. Once steady state had been reached, the DAQ system was collected data for a 30 second interval. The temperatures and voltage were then averaged over the interval and these data were recorded. The purpose of averaging the values over a 30 second interval was to eliminate some minor fluctuations that occurred in the signals. The results from the recorded data were several steady state points at different levels of heat flux. The values of temperature and voltage were later compared to calculated values to evaluate the accuracy of the testing. This process was repeated over many values of α, the angle of inclination of the device.

3.4.2 Adjustments to Test Setup

Several early problems were encountered, and adjustments were made to improve the test procedures. Figure 3.15 shows the first few days of testing with the device constructed with indium film. The points represent steady state values, and the lines represent different days of testing. The data varies wildly from day to day, and even on single lines, the points are not consistent with each other. Initially this was thought to be some sort of hysteresis within the device, as the points are fairly consistent when the

device is being heated or cooled, but points during heating are not consistent with points during cooling (the lines connect the steady state tests in chronological order). It was not understood why hysteresis should happen because the heater was not always changing temperature, i.e. the device should not "remember" if it was being heated or cooled because these were steady state tests. The criteria for steady state at that time was to let the device heat or cool until its top and bottom temperatures were not changing by more than 1 °C within a 30 second interval. It was determined with the help of Dr. Thomas Diller that this definition of steady state was not stringent enough. After the tests shown in Figure 3.15, it was decided to let the device sit for 45-60 minutes between tests to reach steady state. The temperatures were checked after 30-45 minutes, and if they hadn't changed after another 15 minutes then the setup was assumed to be at steady state. This definition resulted in much better data, which are shown in Chapter 4.

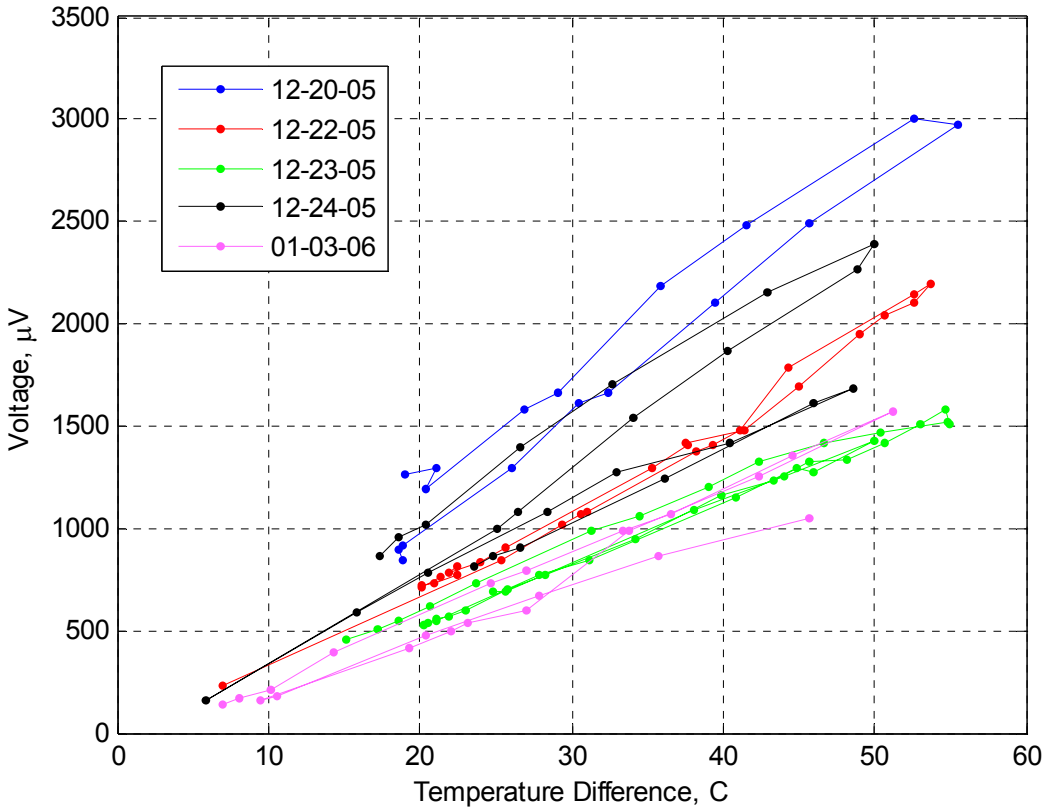

Figure 3.15. Initial test results with the device constructed with indium film.

Another possible source of error that was dealt with early in the process was convection from the ambient air. When the time for steady state was lengthened, it was noticed that there were still long term fluctuations in the temperatures, with periods of around 3-5 minutes. This time period was similar to the fluctuations in room temperature due to the air conditioning unit turning on and off, so it was assumed that the fluctuations would be lessened if the setup was isolated somehow. A glass bell jar was placed over the setup to enclose it from the ambient conditions, as seen in Figure 3.16. Foam was placed between the bottom of the glass bell and the table so that the wires could run under the glass while maintaining a seal.

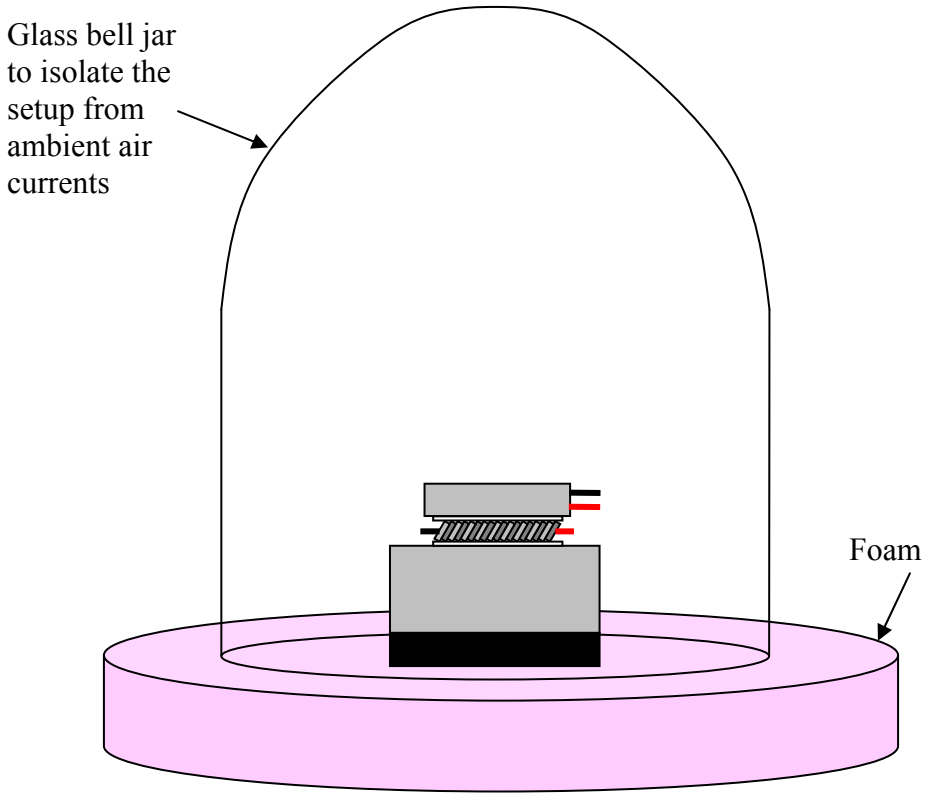

Figure 3.16. Modified setup to decrease errors due to convection in ambient air.

After implementing the glass bell jar, there were still some seemingly random long-term fluctuations in the signal even after the setup reached steady state. The heater was being powered by AC power through a transformer, and after close scrutiny it was discovered that this power had some long-term fluctuations, possibly due to other devices

on the same circuit being turned off and on. The output of the transformer was hooked into an Agilent® 34401A Digital Multimeter, and it was determined that this output was not constant. To solve this problem, the heater was instead powered by the Agilent® E3644A DC power supply so a constant amount of heat flux would be applied to the device. This resulted in much better data with much more consistent steady state values from day-to-day. Figure 3.17 shows the results of testing on the device with α = 77°. The results are fairly consistent after the first five days of testing. However, on the first five days, the results are linear but vary day-to-day. The reason for this variation has not been positively identified, but it may be due to long-term curing of the silver paint contacts on the ends of the device, or transient effects in the indium film or flux used to attach the indium film. The problem was solved by leaving the setup with the heater turned on overnight at a moderate value (hot side temperature ~ 50°C). This method caused the device to give consistent results starting on the first day of testing, and was used each time the angle was changed.

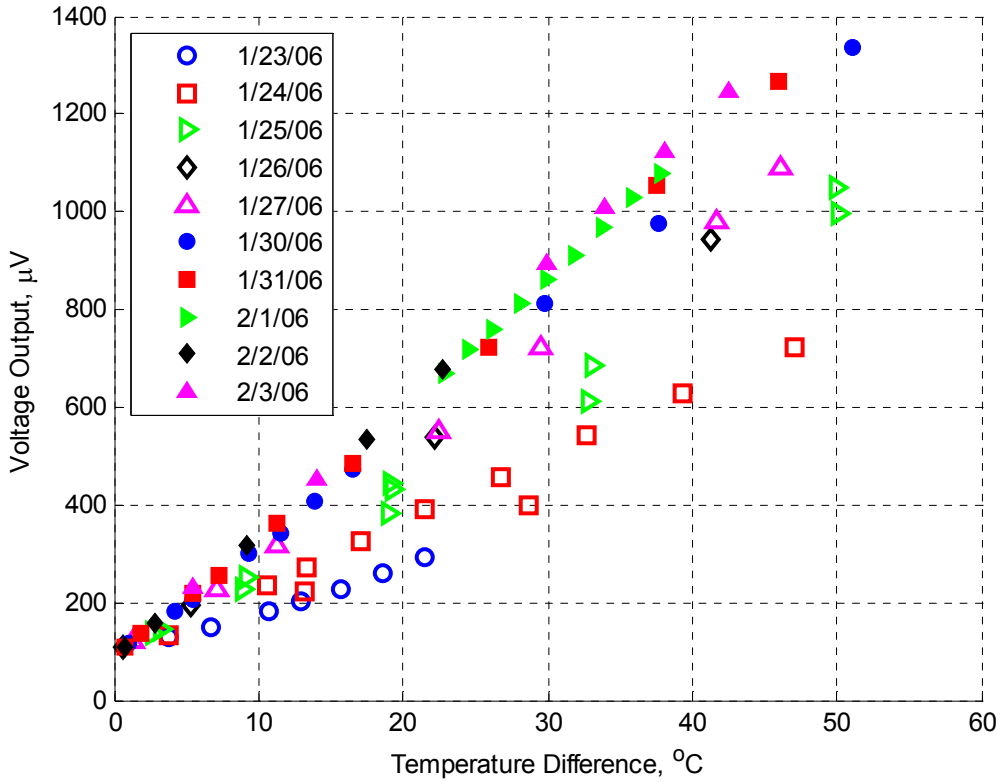

Figure 3.17. Steady state results from the device with α = 77°.

It should be noted that there is an offset of about 100 μV on the linear relationship depicted in Figure 3.17. This offset was evident in every test, and did not change sign if the leads from the device were switched (positive for negative). This means that the small offset was somewhere in the DAQ system, and was easy to deal with. The linear relationship between voltage and temperature difference was found using a least squares method in MatLab®, and the offset was easily determined and subtracted out. The slope of the line then became the "effective Seebeck coefficient" of the device. In later tests the heat flux sensing capabilities of the device were recorded using the power input to the heater (i.e. heat flux) rather than the temperature difference across the device. The two methods are not exactly the same because the value of the thermal conductivity of the device in the direction of the heat flux is not constant with α (see Chap. 4).

The three main adjustments made to the initial test procedures greatly increased the accuracy and repeatability of the measurements. The setup was enclosed in a glass bell jar to eliminate interference from ambient convection, the heater was powered with a DC rather than an AC supply, and the setup was heated overnight to eliminate day-to-day inconsistencies.

3.5 Data Collection and Analysis

A simple LabVIEW® program was written to record data from the thermocouples and voltage leads. A pre-built function named DAQ Assistant was used to transfer data at 10 Hz from the DAQ card to a text file, and a graphical interface (Fig. 3.18) was implemented so the temperatures and voltage could be monitored in real time. For steady state tests, this graphical interface was sufficient to determine the length of time needed. As stated before, the temperatures and voltage were observed about 30-45 minutes after the heater had been adjusted, and again about 15 minutes later. If the graph showed no change in temperature or voltage, the data was recorded.

Once the data had been recorded to a text file using LabVIEW®, that text file was imported to MatLab® using a simple m-file. The data was broken up into vectors and manipulated accordingly. MatLab® was chosen for its ease of use and exceptional

graphical outputs. A summary of values for each test was also stored in an MS Excel® spreadsheet.

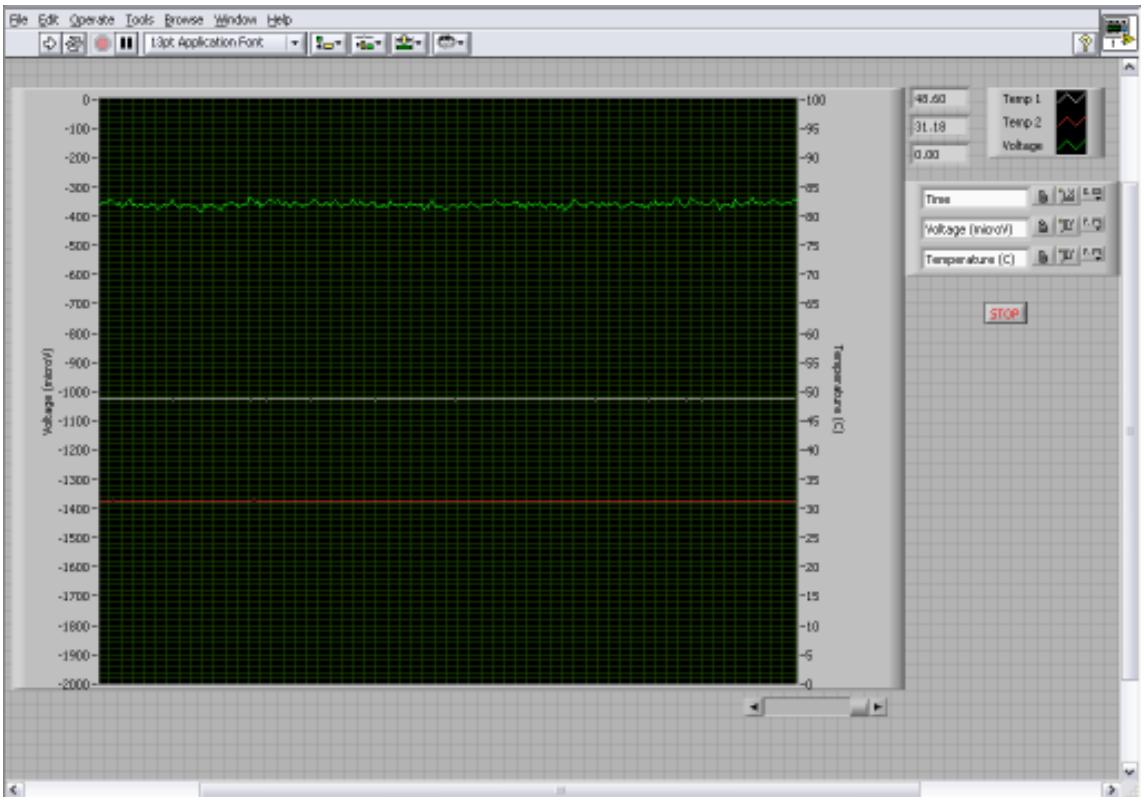

Figure 3.18. The front panel of the LabVIEW® VI used to record voltage and temperature data.

3.6 Summary

Since the ultimate goal is to create a device that will be thermoelectrically efficient, it was decided that bismuth and bismuth telluride would be used for the layers of the device in order to get a large signal. The layers were cut using a dicing saw and attached using indium film. The device was tested by first placing a heater on one side while the other side was attached to a heat sink, and then measuring the induced voltage in the transverse direction. Many adjustments were made to the device and setup as problems arose. The temperature and voltage data from the tests were collected using LabVIEW® and analyzed using MatLab® and Excel®.

Chapter 4 – Results & Analysis

The device was subjected to heat flux sensing tests for almost four months after the test setup was finalized. The length of time between steady state points made the process fairly slow, but nonetheless a large amount of data was recorded. This chapter outlines the major results and an analysis of the data, including comparisons with calculated values, follows. Note that a comprehensive collection of data can be found in Appendix A.

4.1 Expected Results

A study by Zahner *et al*. [10] in 1998 involved similar principles to this project. It consisted of a device constructed from a multilayered structure of sintered copper and constantan foils cut at an angle as shown in Figure 4.1. Their device was tested for heat flux sensing capabilities by irradiating it with a laser so that the surface of the device was subject to a known heat flux. The voltage output was recorded for each test, and these tests were repeated for several angles. The result was Figure 4.2, which shows the actual data points and a curve of calculated values. The equations leading up to this calculated curve will be discussed later in this chapter.

The project that is the subject of this thesis is similar to the study by Zahner *et al*., the major differences being the material selection, geometry of the device, and method of applying heat flux to the device. Therefore the expected results may be calculated using the equations from Ref. 10 with slight adjustments for geometry and materials. These calculations and comparisons are presented later in this chapter.

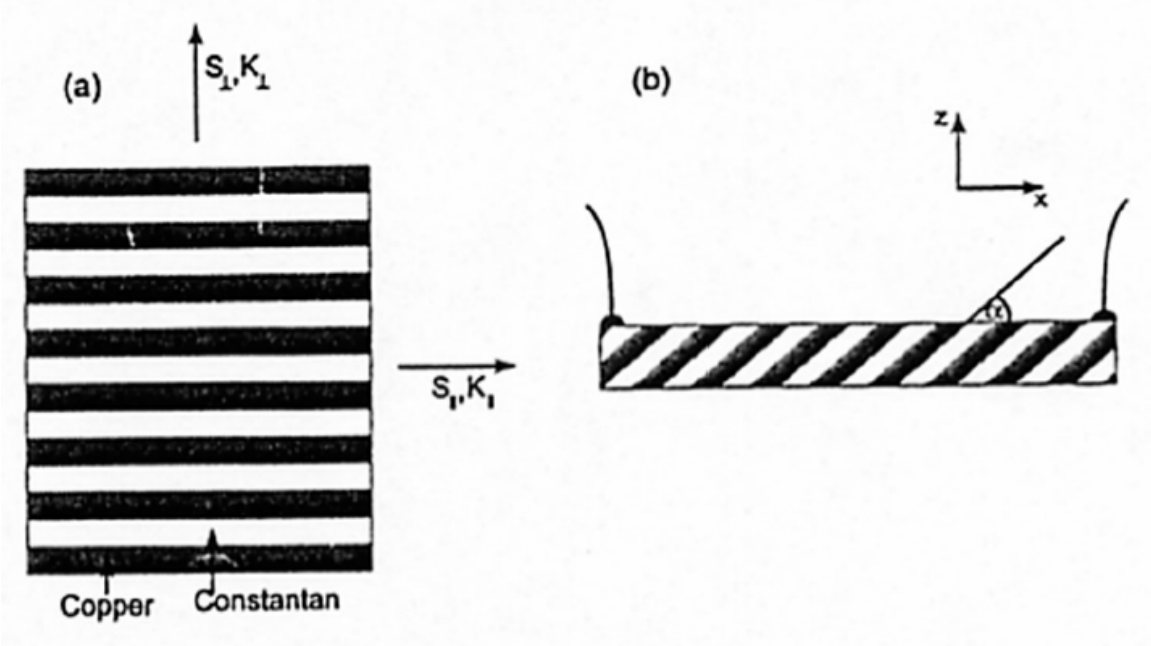

Figure 4.1. Transverse device built and tested by Zahner *et al*. [10]

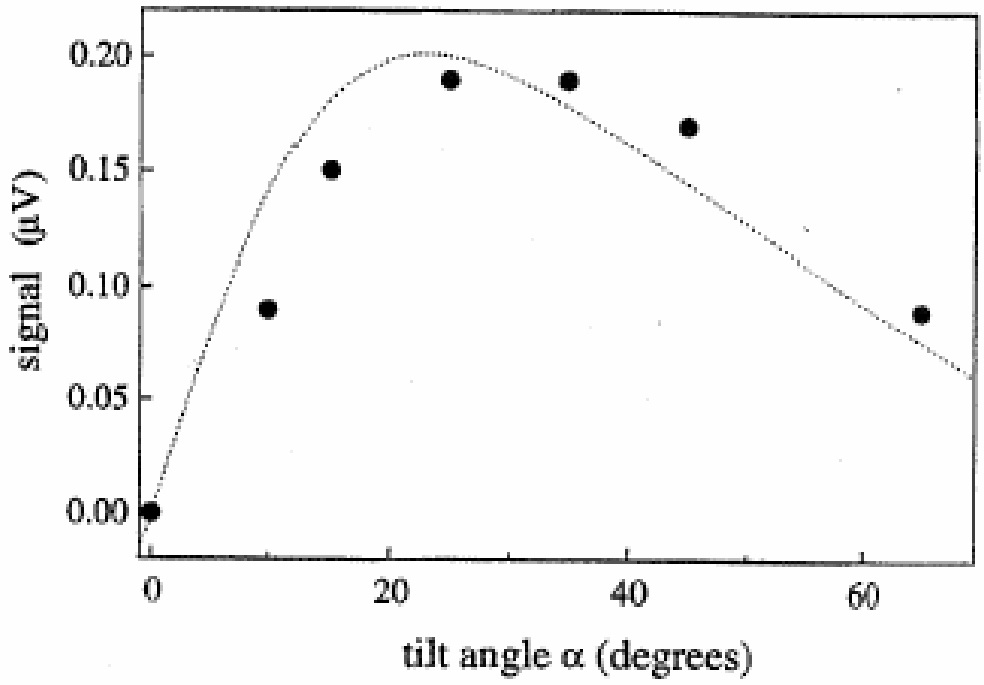

Figure 4.2. Heat flux sensing results at different angles from Zahner *et al*. [10]. A constant heat flux was applied to the device and the resulting signal was recorded at several angles.

4.2 Results for $\alpha = 77°$

The first angle tested was $\alpha = 77°$, an angle close to vertical (Fig. 4.3). The steady state measurements were taken for 10 days, with much variation on the first 5 days. This was due to the aforementioned problem with inconsistent day-to-day measurements that was solved by heating the device overnight. This problem had not been diagnosed yet when the first tests were carried out, so the data is not consistent over the first few days. Figure 4.4 shows all the data from the device with $\alpha = 77°$. It should be noted that this plot is different than the one shown in Fig. 3.17, which shows the same data with the temperature difference on the x-axis. It is sometimes more informative, when studying a heat flux sensor, to plot signal vs. heat flux. The heat flux was calculated by dividing the heater input power by the cross-sectional area of the device. This calculation assumes that all the electrical power consumed by the heater is converted to heat, and that all that heat is transferred to the device. The distinction between temperature difference and heat flux may seem subtle at first, but it is important when comparing angles because the thermal conductivity [10] and cross-sectional area of this device are not constant with angle.

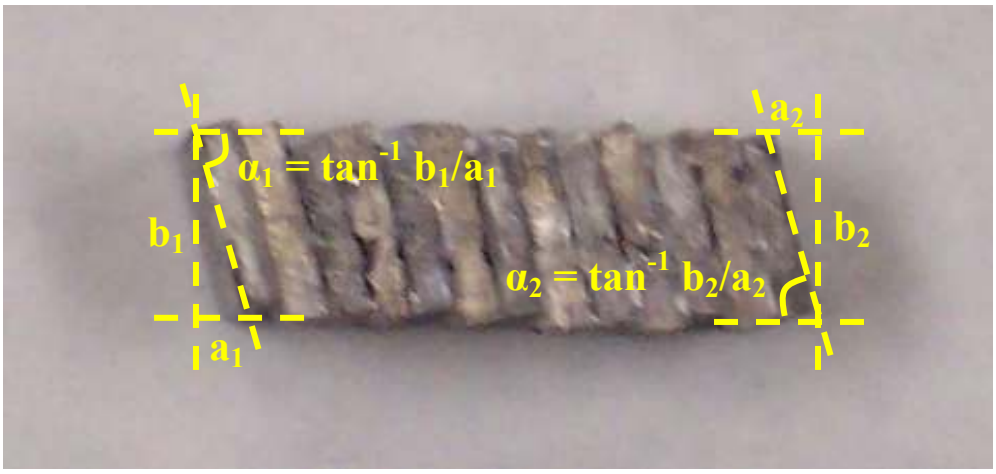

Figure 4.3. The device constructed with indium film with $\alpha = 77°$. A photograph of the device was measured to determine the value of the angle α, which was taken as the average of α_1 and α_2. Photographs of the device at all tested angles can be found in Appendix C.

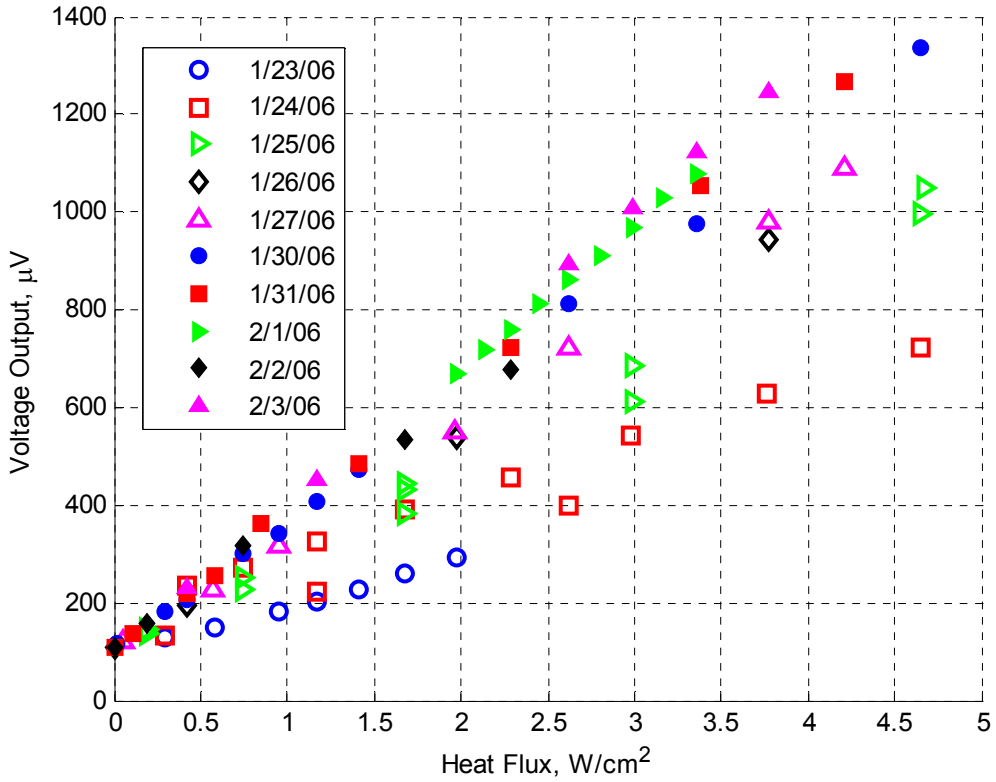

Figure 4.4. All heat flux sensing data from the device with $\alpha = 77°$.

If the early tests are ignored, there are 4 days of testing that are consistent with each other (Fig. 4.5). These points can be used to calculate a linear relationship between heat flux and output voltage. A simple least squares fit was implemented in Matlab®, and the resulting slope of the line was recorded as the signal strength in units of $\mu V/(W/cm^2)$. The process of determining which tests represented the true performance of the device and using these data to characterize the device was implemented for each of the tested angles.

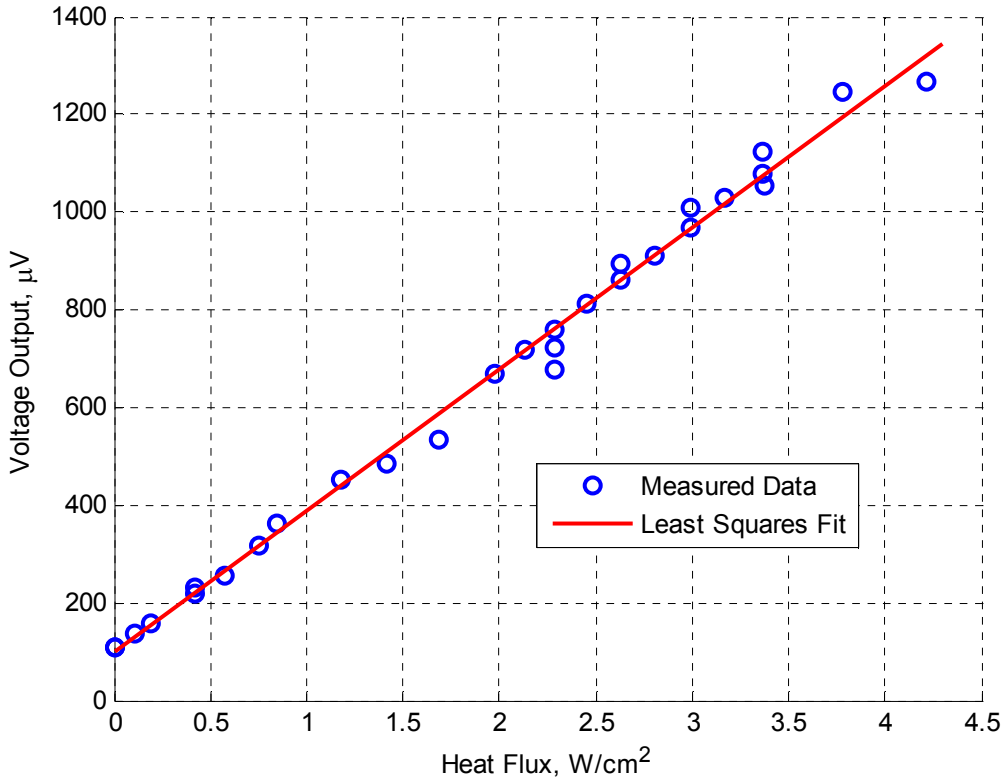

Figure 4.5. Least squares fit for the selected data from the device with $\alpha = 77°$.

The slope of the line in Figure 4.5, and therefore the signal strength of the device with $\alpha = 77°$, is 289.9 μV/(W/cm^2). This is of course much smaller than commercial heat flux sensors (sensors of comparable size made by Vatell Corp. in Christiansburg, VA have sensitivities of up to 150 mV/(W/cm^2) [41]), but keep in mind that the signal strength of a device of this nature is dependent on many factors including geometry and material properties. The devices in this study are meant for proof-of-principle purposes and are not competitive with commercial devices at this time.

4.3 Results for all angles

The problem of day-to-day inconsistencies was solved by heating the device overnight before testing. Therefore, the data from the later tests was much more consistent, and less data was taken before a good relationship was established. For

instance, Figure 4.6 shows all data taken from the device with α = 66°. No data was taken out from this set. The individual data sets for every angle in tabular and graphical form can be found in Appendix A of this report.

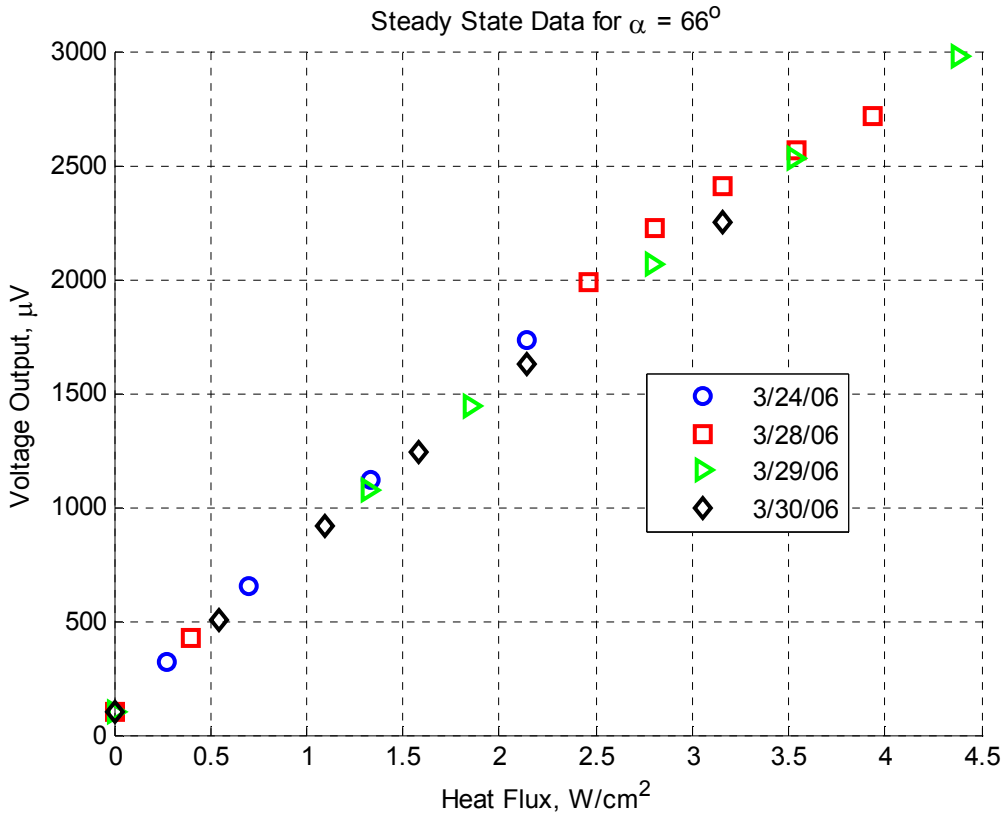

Figure 4.6. All heat flux sensing data from the device with α = 66°.

Figure 4.7 and Table 4.1 show the data from all of the tested angles. These data are compared to calculated values in Chapter 5, but it is already evident in the figure that there are certain repeatability issues. Specifically, there are angles close together that have wildly different voltage outputs. These tests were conducted separately, i.e. the device was set to one angle, then a second angle, then a third angle close to the first angle. One would expect that the results from the first angle and the third angle would be close since the angles are almost the same, but in some cases that did not occur. It is not known exactly what caused these problems, but the problem was solved by re-melting the indium film and allowing it to cool again. This process was repeated until the device gave an output near the expected value. The output seemed to be either very low or near the expected value, with no in-between values. Because of this fairly "digital" behavior,

it was assumed that the process of re-melting the indium film had some direct effect on the output of the device, and that sometimes the output was normal while other times it was very low. For the remainder of the tests, the device was re-melted until it gave a good output.

It is important to note that foam insulation was used on the heater for the last three angles. It was earlier assumed that all the heat from the heater was going through the device to the heat sink, but it was known that some heat was escaping to the surroundings from the top and side surfaces of the heater. In order to improve the accuracy of the assumption, foam insulation was attached to the top and side surfaces of the heater, in order to direct more heat down into the device (Fig. 4.8). The tests with insulation seem to result in a larger signal strength (closer to predicted values) than those without insulation.

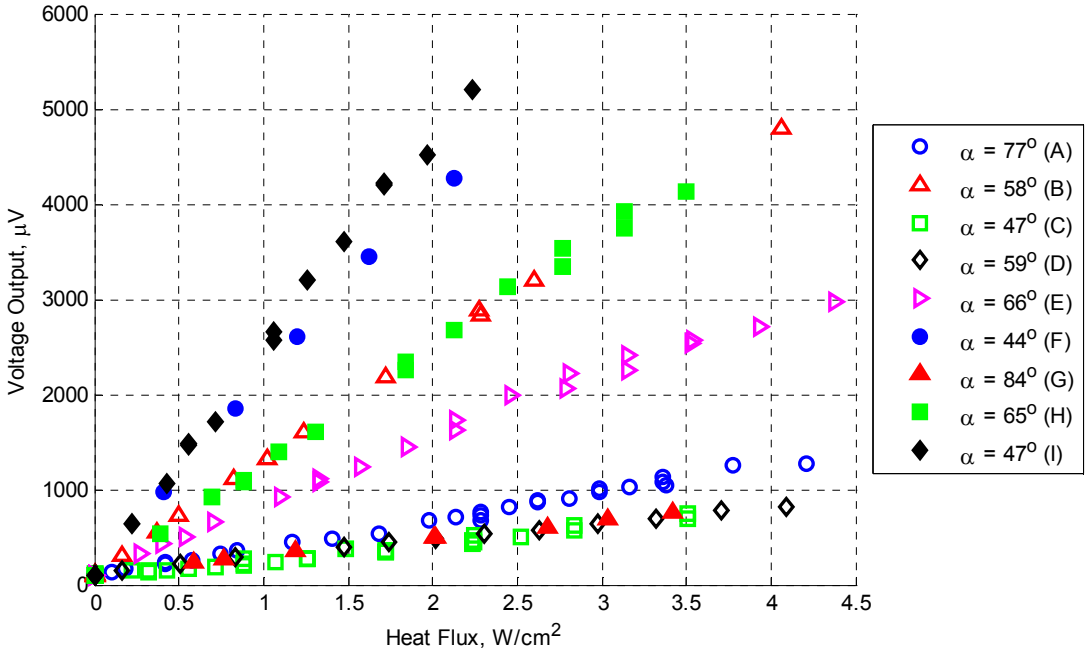

Figure 4.7. Steady state results from all nine angles. Each point represents a steady state test, and each data set represents the test from a single angle taken over several days. The sets are in chronological order from A to I.

It can be seen in both Figure 4.7 and Table 4.1 that there is a small offset associated with each data set. The offset is approximately the same for each angle, or at least does not correlate with the magnitude of the angle. It was assumed that the offset

was due to a flaw in the data acquisition system, and did not affect the results. The signal strength (SS) reported in Table 4.1 is simply the slope of a least-squares line for each data set, and the offset is the y-intercept of that line.

Table 4.1. Steady state results from all nine angles.

	Angle, α	**Sensitivity $\mu V / (W / cm^2)$**	**Offset (μV)**
A	77°	289.9	98.3
B	58°	1172.0	132.4
C	47°	173.2	81.8
D	59°	175.9	120.7
E	66°	682.5	157.2
F	44°	1980.1	162.5
G	84°	190.2	114.8
H	65°	1197.8	84.7
I	47°	2321.6	130.4

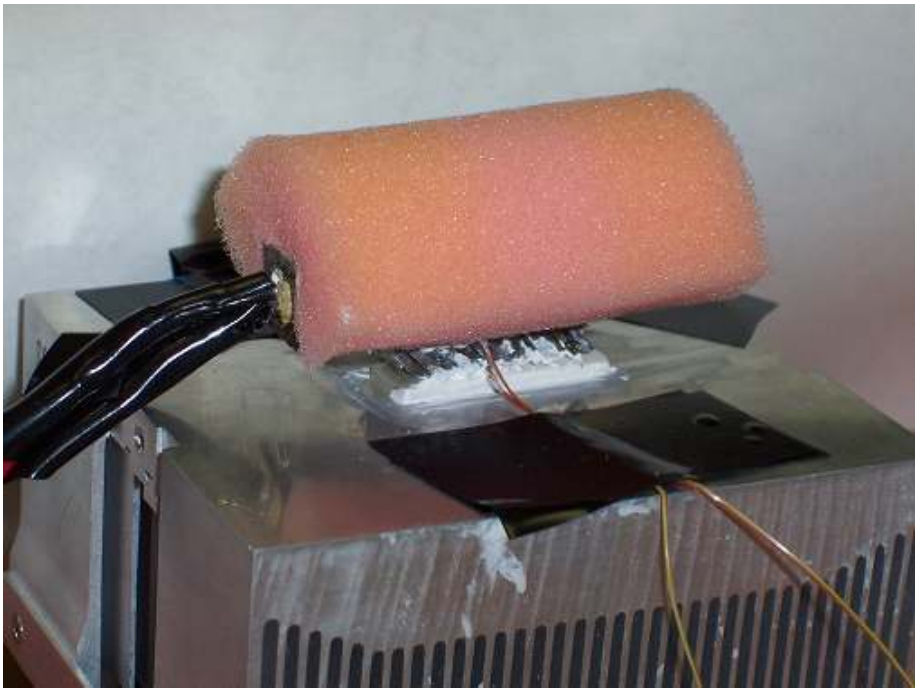

Figure 4.8. Insulation was added to the heater in order to improve the assumption that all the heat was going through the device.

In order to compare angles, the slope and offset of the least squares line was used. A specific value of heat flux was chosen, and the output voltage was calculated for each angle. Because each set of steady state data was close to linear, this method was determined to be the best way to compare the angles. Figure 4.9 shows the output voltage of each of the nine angles with a heat flux of 2 W/cm^2.

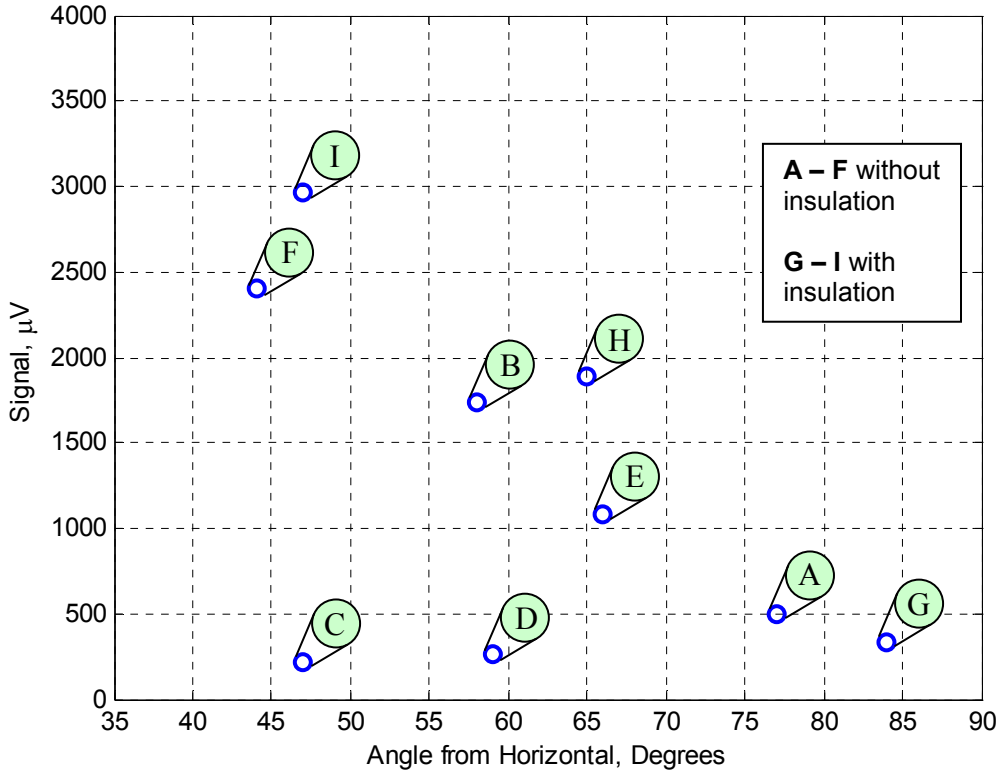

Figure 4.9. The signal from each angled device subjected to a heat flux of 2 W/cm^2 was derived from the raw data for easy comparison between angles. The tests are again labeled chronologically from A to I.

At first glance it may seem that there is no correlation between the angle and the output signal in Figure 4.9. However, it has been determined that there was something wrong with the device in sets C and D. There may have been bad connections between layers, or some substance interfering with thermoelectric effects. The small output seen in C and D was also apparent a few more times throughout testing, but after it was realized that the output should not be so low, the device was re-melted until the output was closer to the expected value. As explained before, this phenomenon seemed to be "digital," i.e. the output was either very low or near the expected value. The important

point here is that the problem seems to be related to the process of constructing the device rather than some unknown problem with the thermoelectric effects.

4.4 Comparing Measured Data with Calculated Values

Once the data for several angles had been collected, it could be compared to calculated values. Equations from Ref. 10 and 23 were modified to calculate the expected signal strength at each angle based on material properties and geometric orientation.

4.4.1 Outline of Governing Equations

The paper by Zahner *et al*. [10], first introduced in Chapter 2, outlines the equations needed to predict the voltage output of a transverse heat flux sensor made of alternating layers. The device used in Zahner's paper was a multilayered structure of copper and constantan films. The layers were sintered and cut at an angle to produce a transverse thermoelectric device. Although the materials and geometry are different in this work, the equations can still be applied.

The underlying equation for all thermoelectric heat flux sensors states that the electric field, E, produced by such a device when subjected to a temperature gradient can be expressed as [10]

$$E = S \cdot \nabla T \tag{4.1}$$

where S is the Seebeck tensor and ∇T is the temperature gradient. The Seebeck tensor is a 3×3 matrix, but in most cases it can be simplified. In the case of a transverse heat flux sensor, heat is moving only in the z direction and electricity is moving only in the x direction (there are local eddies in the individual layers, but when evaluating the total

voltage output of the device, these can be ignored). The general form of the Seebeck tensor is [10]

$$S = \begin{bmatrix} S_{\parallel}\cos^2\alpha + S_{\perp}\sin^2\alpha & 0 & \tfrac{1}{2}\left(S_{\parallel} - S_{\perp}\right)\sin 2\alpha \\ 0 & S_{\parallel} & 0 \\ \tfrac{1}{2}\left(S_{\parallel} - S_{\perp}\right)\sin 2\alpha & 0 & S_{\parallel}\sin^2\alpha + S_{\perp}\cos^2\alpha \end{bmatrix} \tag{4.2}$$

where $S_{\parallel}$ is the Seebeck coefficient in the x direction (the direction of electrical flow), $S_{\perp}$ is the Seebeck coefficient in the z direction (the direction of heat flow), and α is the angle of inclination of the layers from the x axis (Fig. 4.1).

If the device were simply a single layer of intrinsically anisotropic material, then $S_{\parallel}$ and $S_{\perp}$ would simply be the in-plane and out-of-plane Seebeck coefficients of the material, respectively. The Seebeck coefficients of a multilayered structure depend on the thermoelectric properties of the constituents [10]. The in-plane and out-of-plane Seebeck coefficients of a multilayered device made of bismuth and bismuth telluride layers are given by [10]

$$S_{\parallel} = \frac{\sigma_{Bi}S_{Bi} + \sigma_{Bi_2Te_3}S_{Bi_2Te_3}}{\sigma_{Bi} + \sigma_{Bi_2Te_3}}, \quad S_{\perp} = \frac{R_{Bi}S_{Bi} + R_{Bi_2Te_3}S_{Bi_2Te_3}}{R_{Bi} + R_{Bi_2Te_3}} \tag{4.3}$$

where σ is the electrical conductivity and R is the thermal resistance. The thermal resistance is given by $R = L/k$, where L is a characteristic dimension and k is the thermal conductivity. Since the dimensions of all layers are equal in this case, R can be replaced by k^{-1} in Equation 4.3.

The electric field in a transverse device subject to a temperature gradient can be determined using Equations 4.1, 4.2 and 4.3. Since the heat and electric current are in orthogonal directions in a transverse device, the off-diagonal terms in the Seebeck coefficient are used. With a temperature gradient in the z direction, the electric field is given by

$$E = \tfrac{1}{2}\sin 2\alpha\left(S_{\parallel} - S_{\perp}\right)\nabla_z T \tag{4.4}$$

The importance of anisotropy is apparent in Equation 4.4. The magnitude of the electric field is directly proportional to the difference between $S_{\parallel}$ and $S_{\perp}$, and therefore the material properties must be sufficiently different for a large electric field to be induced. Recall also that an important advantage of a transverse heat flux sensor is that the output voltage is proportional to the length of the device rather than the thickness. The actual voltage output of the device is equal to the magnitude of the electric field multiplied by the length of the device (assuming E is constant along the length of the device):

$$V = \tfrac{1}{2}\sin 2\alpha\left(S_{\parallel} - S_{\perp}\right)\nabla_z TL \tag{4.5}$$

In order to predict the output voltage of a transverse device, the temperature gradient across the device must be determined. The temperature difference across the device was measured in the experimental process outlined in Chapter 3, but recall that the heat flux was also monitored. The electrical power used by the heater was divided by the surface area of the device in order to calculate the heat flux for each angle. Fourier's Law $\left(q'' = k\nabla T\right)$ can be used along with Equation 4.5 to predict the output voltage of the device based on a heat flux input. The magnitude of the output voltage is then given by

$$V = \tfrac{1}{2}\sin 2\alpha\left(S_{\parallel} - S_{\perp}\right)\frac{q''}{k_z}L \tag{4.6}$$

where k_z is the "effective" thermal conductivity of the device in the direction of heat flow, which can be determined from the material properties of the constituents. The effective thermal conductivity of the device is given by [10]

$$k_z = k_{\parallel}\sin^2\alpha + k_{\perp}\cos^2\alpha \tag{4.7}$$

where $k_{\parallel}$ and $k_{\perp}$ are the in-plane and out-of-plane thermal conductivities, respectively, and are given by [10]

$$k_{\parallel} = \tfrac{1}{2}\left(k_{Bi} + k_{Bi_2Te_3}\right), \quad k_{\perp} = \frac{2k_{Bi}k_{Bi_2Te_3}}{k_{Bi} + k_{Bi_2Te_3}} \tag{4.8}$$

where k_{Bi} and $k_{Bi_2Te_3}$ are the thermal conductivities of bismuth and bismuth telluride, respectively. Equations 4.3 and 4.8 can be combined with the material properties outlined in Table 3.1 to calculate the values of $S_{\parallel}$, $S_{\perp}$, $k_{\parallel}$, and $k_{\perp}$. These values are shown in Table 4.2.

Table 4.2. Summary of the "effective" material properties of the multilayered device calculated from the properties of the constituent materials.

Material Properties	**Equation**	**Result**
$\sigma_{Bi} = 9\times10^{5}\ 1/\Omega m$, $\sigma_{Bi_2Te_3} = 2.11\times10^{4}\ 1/\Omega m$, $S_{Bi} = 34.5\ \mu V/K$, $S_{Bi_2Te_3} = 190\ \mu V/K$	$S_{\parallel} = \frac{\sigma_{Bi}S_{Bi} + \sigma_{Bi_2Te_3}S_{Bi_2Te_3}}{\sigma_{Bi} + \sigma_{Bi_2Te_3}}$	$S_{\parallel} = 38.06\ \mu V/K$
$k_{Bi} = 8.0\ W/mK$, $k_{Bi_2Te_3} = 1.8\ W/mK$, $S_{Bi} = 34.5\ \mu V/K$, $S_{Bi_2Te_3} = 190\ \mu V/K$	$S_{\perp} = \frac{k_{Bi}^{-1}S_{Bi} + k_{Bi_2Te_3}^{-1}S_{Bi_2Te_3}}{k_{Bi}^{-1} + k_{Bi_2Te_3}^{-1}}$	$S_{\perp} = 21.85\ \mu V/K$
$k_{Bi} = 8.0\ W/mK$, $k_{Bi_2Te_3} = 1.8\ W/mK$	$k_{\parallel} = \tfrac{1}{2}\left(k_{Bi} + k_{Bi_2Te_3}\right)$	$k_{\parallel} = 4.9\ W/mK$
$k_{Bi} = 8.0\ W/mK$, $k_{Bi_2Te_3} = 1.8\ W/mK$	$k_{\perp} = \frac{2k_{Bi}k_{Bi_2Te_3}}{k_{Bi} + k_{Bi_2Te_3}}$	$k_{\perp} = 2.94\ W/mK$

4.4.2 Characterization of Device Geometry

One significant difference between the device used in Zahner's paper [10] and the device used in this work is the selection of materials. Zahner's device was constructed of layers of copper and constantan, while the device used in this work was constructed of layers of bismuth and bismuth telluride. However, a more subtle difference is the geometry of the device, and how devices with different angles were made. As shown in Figure 4.1, the device in Ref. 10 was cut from a larger sample of the multilayered structure into a rectangular device, and many devices were cut at different angles but with the same dimensions. The device used in this work was made of rectangular pieces that were connected with indium film as shown in Figure 4.10. This method was used so that the same pieces could be used multiple times. The irregular shape of the device causes the length and thickness to change with the angle. Figure 4.10 shows the orientation of the device and the dimensions in question.

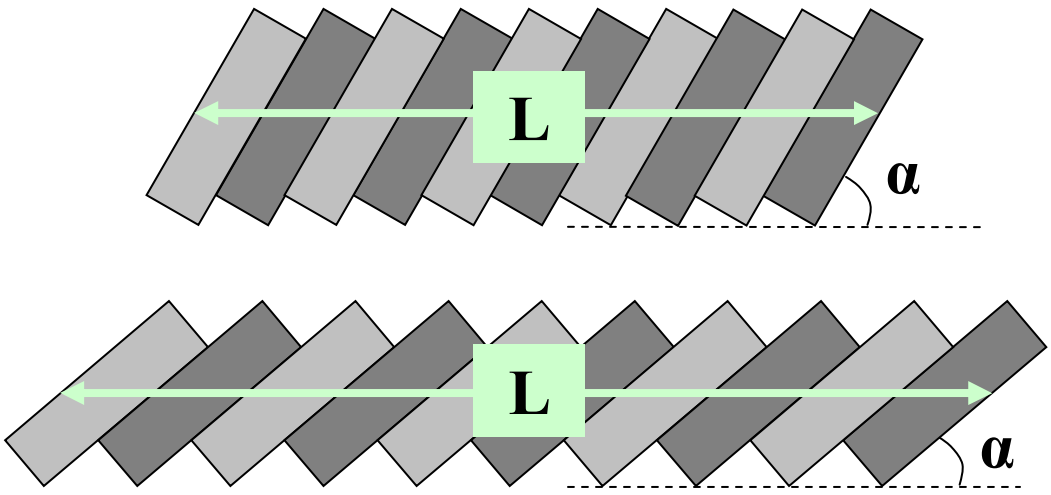

n = number of pieces

t = layer thickness

$$L = \frac{n \cdot t}{\sin \alpha} = \frac{13 \cdot 0.00113 \text{ m}}{\sin \alpha} = \frac{0.01469 \text{ m}}{\sin \alpha}$$

Figure 4.10. The length of the device as a function of the angle α. There were 13 layers used in each tested device, each with a thickness of 1.13 mm.

4.4.3 Comparing the Actual Data to the Calculated Curve

Once the material properties and device geometry had been determined, the components of Equation 4.6 could be collected to predict the signal strength of the device over a range of angles. When the components are all combined, the resulting output voltage is given by

$$V = \tfrac{1}{2}\sin 2\alpha\left(S_{\parallel} - S_{\perp}\right)\frac{q''}{k_z}L$$

$$V = \tfrac{1}{2}\sin 2\alpha\left(16.21\ \mu\text{V/K}\right)\left[\frac{q''}{\left(4.9\ \text{W/mK}\right)\sin^2\alpha + \left(2.94\ \text{W/mK}\right)\cos^2\alpha}\right]\frac{0.01469\ \text{m}}{\sin\alpha} \quad (4.9)$$

The output voltage V was calculated for a range of angles α with a given heat flux q'', and the result was in units of μV. The resulting curve was then plotted along with the actual data, as shown in Figure 4.11. The curve was plotted by selecting a specific value of heater power (2 W), and the points are plotted by calculating the output voltage of the device at that value of heater power, using the slopes in Table 4.1. It is apparent in Figure 4.11 that the predicted signal is at a maximum at an angle of about 39°. However, the device was only tested for angles between 45° and 90° because of the geometry of the device. It proved to be too difficult to assemble the device with a shallow angle, because the contacts between layers would be too small (see Figure 4.10). Without data on both sides of the curve it is difficult to say with certainty that the data follow the trend of the predicted line, but they certainly seem to be heading in the right direction. The three points that represent data sets where insulation was used (G, H, and I) are closer to the curve than the four points where insulation was not used (A, B, E, and F). There is a significant amount of error even in the tests where insulation was used, and the possible sources of this error are discussed in the next section.

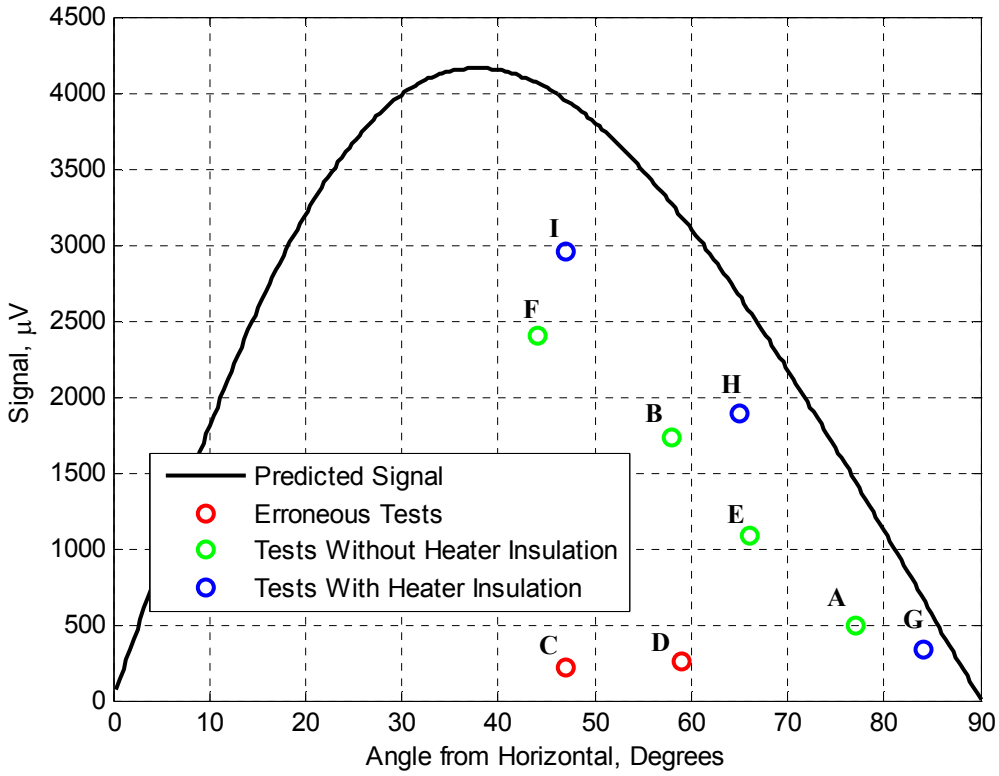

Figure 4.11. The predicted values of signal strength are plotted with the actual data. The points are again labeled chronologically from A to I. All points correspond to a constant heater power of 2 W.

4.4.4 Possible Sources of Error

The points in Figure 4.11 (other than C and D) seem to follow the trend of the predicted curve well, although there is a sizeable gap between the points and the curve. The most obvious possible source of error is that the heat flux was calculated using the electrical input to the heater. The heater probably turned almost all of that electrical power into heat, but not all the heat went though the transverse device. Some escaped through the other sides of the heater, and some was lost along the sides of the device, before reaching the heat sink. It is apparent that this was a large source of error because the points in Figure 4.11 got much closer to the predicted curve when insulation was added.

Another possible source of error is the electrical connections between the layers. The indium film could have had some small effect on the thermoelectric properties of the device, and the quality of the connections almost certainly had some effect on local thermoelectric effects (eddies) that could have contributed to the total output of the device. An ideal connection would have been seamless, as if the device were made of one solid material. The connections on either end of the device (silver paint) also could have affected the signal. The irregular shape of the device may have contributed to the error as well. The calculations assumed that the device was of a rectangular shape, but the actual device had a jagged edge due to the shape of the layers (Figure 4.10). The protrusions on the top and bottom sides of the device may have contributed local current eddies that affected the signal. Finally, the uncertainties in the material properties and geometric dimensions could have affected the predicted values and the measured data points. These uncertainties are discussed more thoroughly in the next section.

4.5 Uncertainty Analysis

The predicted values of the output voltage of the device were determined using published and measured material properties. It is difficult to assign uncertainties to these values, because the particular materials used may or may not be of the same exact form as those tested in other publications. The bismuth used in the device was amorphous, while the bismuth in other studies may be single crystal. The bismuth telluride samples may be doped differently. Table 4.3 shows the uncertainties used in calculating maximum and minimum values for the predicted curve. These uncertainty values do not have any real scientific basis, but are useful for determining the general effects of uncertainty and examining the properties for which the output of the device is most sensitive. The dimensions of the device were measured directly with a caliper, so the accuracy of the dimensions is high. The uncertainty in the actual measurements was also analyzed. Each data set was close to linear, but outer bounds were drawn to include all the points and the minimum and maximum values of signal strength were added as error bars to the final plot.

4.5.1 Uncertainty in Material Properties and Geometry

Each material property (S, k, and σ) was subjected to theoretical uncertainties of 5%, 10%, and 15%. The output voltage was calculated using these uncertainties to find curves for the minimum and maximum values of the output voltage. First the effects of individual properties had to be determined, because some cause the voltage to increase and some cause the voltage to decrease. Table 4.3 shows the effects of the individual material properties. The output voltage was first calculated at its maximum value (α = 37.8°) with the nominal values of all material properties. Then each property was changed individually to values 15% higher and lower than the nominal value. The effect of changing each property was recorded, and once the effects of all the properties had been recorded, all six properties were altered to find absolute maximum and minimum values of the output voltage. Note that these maximum and minimum values correspond to a situation in which all six material properties have the maximum amount of uncertainty in the direction that either maximizes or minimizes the output voltage, which is very unlikely. It is especially unlikely since the electrical conductivity and thermal conductivity are somewhat linked, i.e. a material with a high electrical conductivity tends to also have a high thermal conductivity.

Table 4.3. The effects of uncertainty in material properties on the output voltage (V) of the device. The output voltage is calculated at its maximum value, which is at $\alpha = 37.8°$.

Property	Effect on V if property is increased by 15%	Effect on V if property is decreased by 15%
$S_{Bi} = 34.5\ \mu V/K$	- 3.33 %	+ 3.33 %
$S_{Bi_2Te_3} = 190\ \mu V/K$	+ 18.33 %	- 18.33 %
$\sigma_{Bi} = 9\times10^5\ 1/\Omega m$	+ 0.37 %	- 0.49 %
$\sigma_{Bi_2Te_3} = 2.11\times10^4\ 1/\Omega m$	- 0.42 %	+ 0.43 %
$k_{Bi} = 8.0\ W/mK$	- 4.50 %	+ 4.84 %
$k_{Bi_2Te_3} = 1.8\ W/mK$	- 9.40 %	+ 11.46 %

Once the contributions of individual material properties had been determined, the uncertainties were combined in a way that would maximize the uncertainty of the output voltage. That is, a curve was constructed using the uncertainty in each property that would maximize the output voltage, and another curve was constructed using the uncertainty in each property that would minimize the output voltage. The results of these combinations are shown in Figure 4.12 along with the actual data.

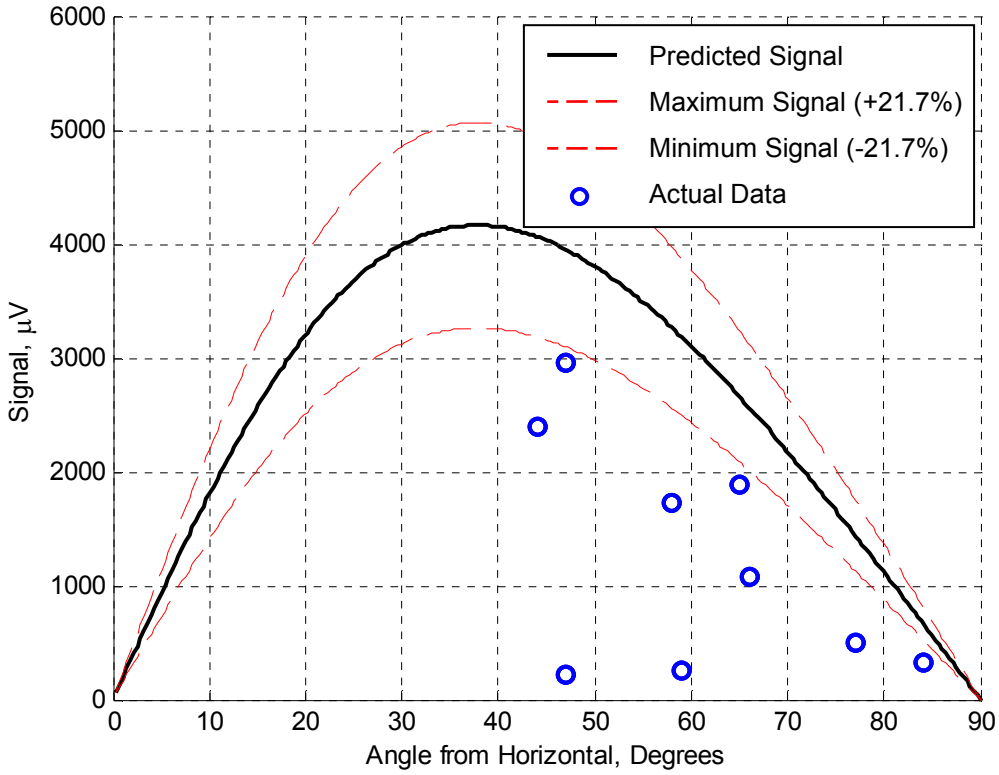

Figure 4.12. The effect of uncertainty on the predicted output voltage of the device. The red dashed lines represent the maximum and minimum values of the predicted output voltage using 15% uncertainty in the material properties of the device.

The actual data points in Figure 4.12 are close to the curve representing the minimum value of output voltage with material property uncertainties of 15%. To compare these results with the individual contributions found in Table 4.3, the values of the maximum and minimum curves at the peak angle of 37.8° are 21.7% higher and 21.7% lower than the nominal curve, respectively. If the uncertainties in the individual

properties are simply added, the total uncertainty would seem to be much more than 21.7%, but some of the effects tend to cancel each other out in the equations.

4.5.2 Uncertainty in Measurements

Another possible source of error is the linearity of the data sets. The output of the device at each angle was measured at several different values of heat flux, and the resulting data sets were fairly linear (see Figure 4.7). Each data set was fitted with a least-squares line, the assumption being that the relationship between heat flux and output voltage was linear. However, there was some amount of error involved in each data set, as the line did not go through every point. In order to determine the amount of uncertainty involved in linearizing the data sets, two methods were used. The first method was to draw alternate slopes into the plots in order to include all of the data points, as shown in Figure 4.13.

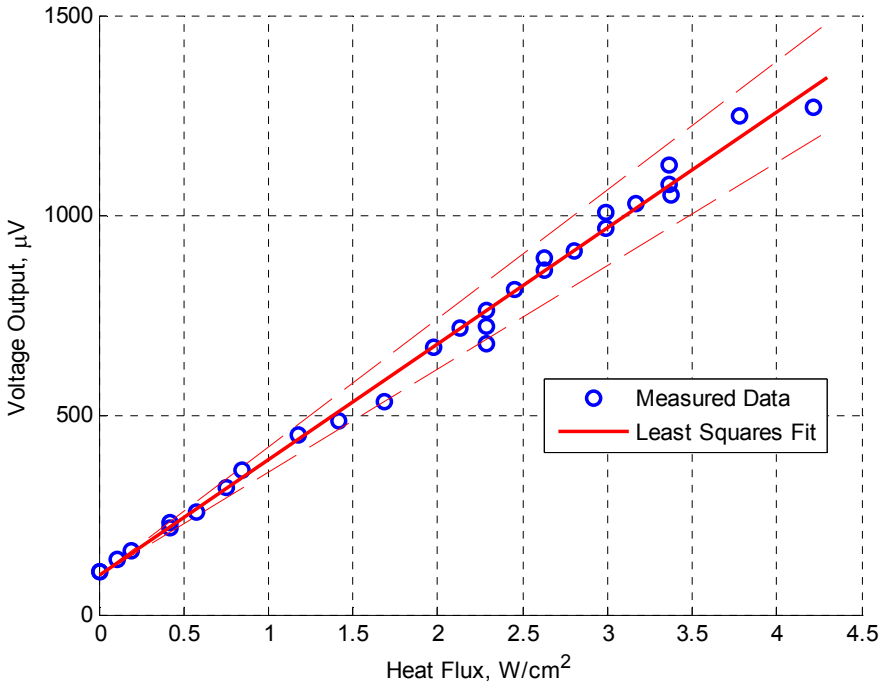

Figure 4.13. The result of uncertainty analysis for $\alpha = 77°$. The dashed lines were drawn to include all points, and represent a 10% uncertainty in the slope of the least-squares line.

The dashed lines in Figure 4.13 represent a 10% uncertainty in the measured data. That is, the slopes of the dashed lines are 10% larger and smaller than the slope of the least-squares line. These dashed lines were added to the plots for all nine angles that were tested, and the plots can be found in Appendix A. The uncertainty in the plot for $\alpha = 77°$ was one of the largest; most of the others had uncertainties of less than 5%.

Once the uncertainty in the measured data had been estimated, it could be added to the plot shown in Figure 4.12. Error bars were added to each data point, indicating the uncertainty in the linearity of the data. Figure 4.14 shows the results of uncertainty analysis on the predicted values and the measured values. The error bars are quite small when seen on the scale of the plot, and they do not extend into the region of 15% uncertainty of the predicted values.

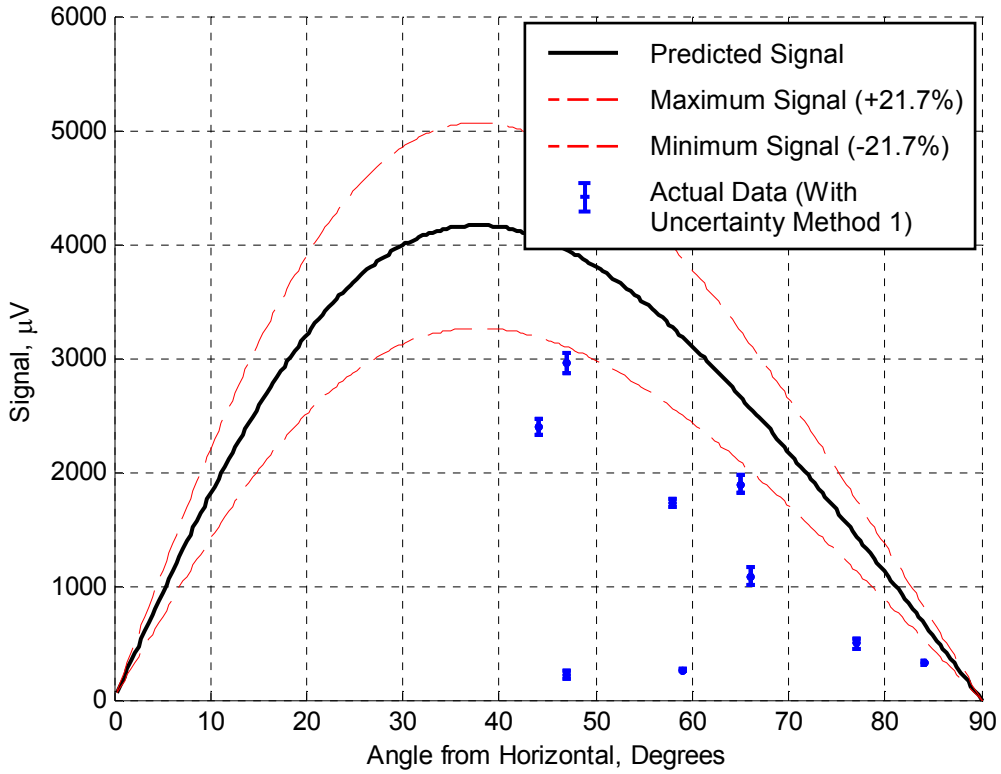

Figure 4.14. The result of uncertainty analyses on the measured data. The points represent the slopes from the nine data sets, and the error bars represent the uncertainty in those slopes.

The second method of estimating the uncertainty in the data was to statistically analyze the variance of the data from the least-squares line. The slope of the line describes the approximate value of the output voltage at any given heat flux. Therefore, the uncertainty can be analyzed by finding the variance between the predicted value and the actual value of the output voltage at every measured heat flux. The standard error of the least squares line is given as [42]

$$S_{yx} = \sqrt{\frac{\sum_{i=1}^{N} (y_i - y_{ci})^2}{v}} \tag{4.10}$$

where N is the number of data points, y_i is the actual voltage measurement at the i^{th} data point, y_{ci} is the predicted value at the i^{th} data point, and v is the degrees of freedom of the fit, $v = N - (m + 1)$, where m is the order of the least-squares fit. In this case $m = 1$, so $v = N - 2$. The standard error is multiplied by the t estimator (since the data set is finite) to arrive at the uncertainty in the fit [42]:

$$y_c \pm t_{v,P} S_{yx} \tag{4.11}$$

where y_c is the equation for the least-squares fit, $t_{v,P}$ is the t estimator at the proper values of v and P, and P is the percentage of confidence. A 90% confidence level was considered to be adequate in this case. The value in Equation 4.11 was added and subtracted from the slope of the least squares fit to determine the maximum and minimum values for the slope.

For each of the nine angles, the uncertainty was calculated with this method, and new error bars were added to the plot, as seen in Figure 4.15. The blue error bars indicate the uncertainty found in the "guessing" method, and the red error bars indicate the uncertainty found using the above equations. Table 4.4 summarizes the results of uncertainty analysis on the measured data.

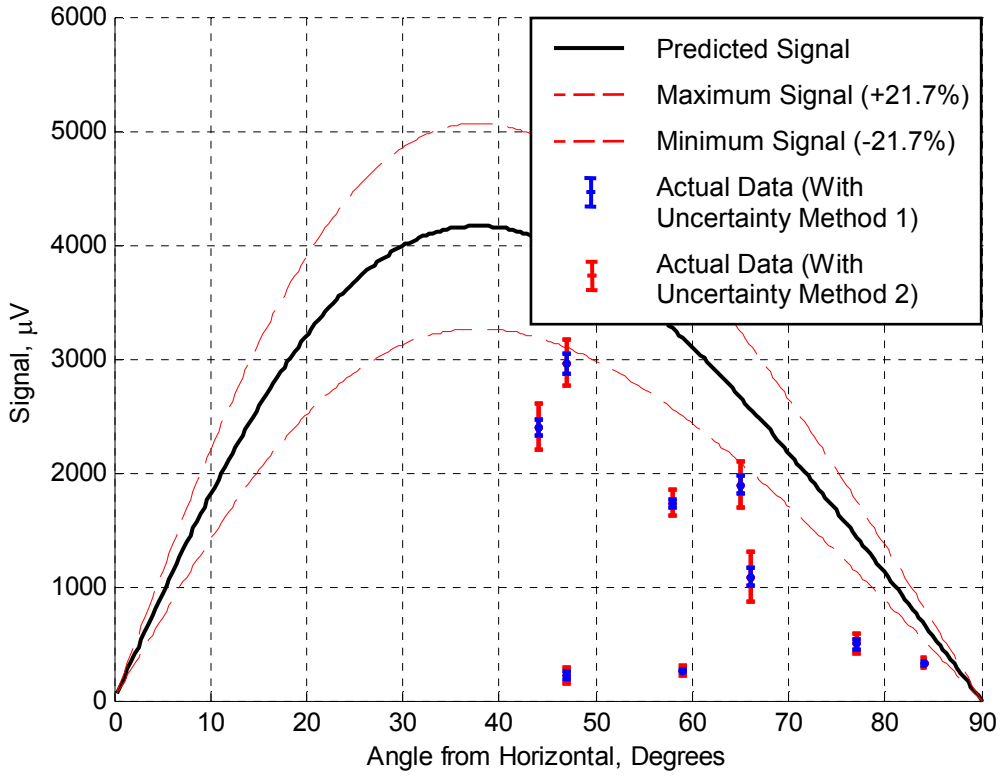

Figure 4.15. Comparison of the two methods for finding the uncertainty in the measured data. The smaller blue error bars indicate the uncertainty found in the "guessing" method, and the larger red error bars indicate the uncertainty found using the statistical method.

Table 4.4. Summary of the uncertainties found using the two methods.

Data Set	Angle	Intercept (μV)	Slope (μV/(W/cm^2))	Uncertainty from "guessing" method	Uncertainty from statistical method
A	77	98.3	289.9	± 10 %	± 17.6 %
B	58	132.4	1172.0	± 2 %	± 6.8 %
C	47	81.8	173.2	± 15 %	± 28.8 %
D	59	120.7	175.9	± 4 %	± 14.6 %
E	66	157.2	682.5	± 7 %	± 19.5 %
F	44	162.5	1980.1	± 3 %	± 8.5 %
G	84	114.8	190.2	± 5 %	± 14.2 %
H	65	84.7	1197.8	± 4 %	± 11.0 %
I	47	130.4	2321.6	± 3 %	± 6.7 %

Figure 4.15 and Table 4.4 show that the two methods produced significantly different values of uncertainty at each point. This is most likely due to bias in the methods. In the first method, where the alternate slopes were "guessed," more attention was paid to the data points at higher values of heat flux because these points tended to have larger magnitudes of error. However, the statistical method paid equal attention to all points, and the points at lower values of heat flux, while closer to the line, sometimes had larger relative values of error. Figure 4.16 outlines a description of the bias in the two methods. In the hypothetical plot, the "guessing" method includes the larger value and is closer to the least-squares line, but the statistical method is influenced more by the smaller value because it must "pivot" around the intercept while including all points.

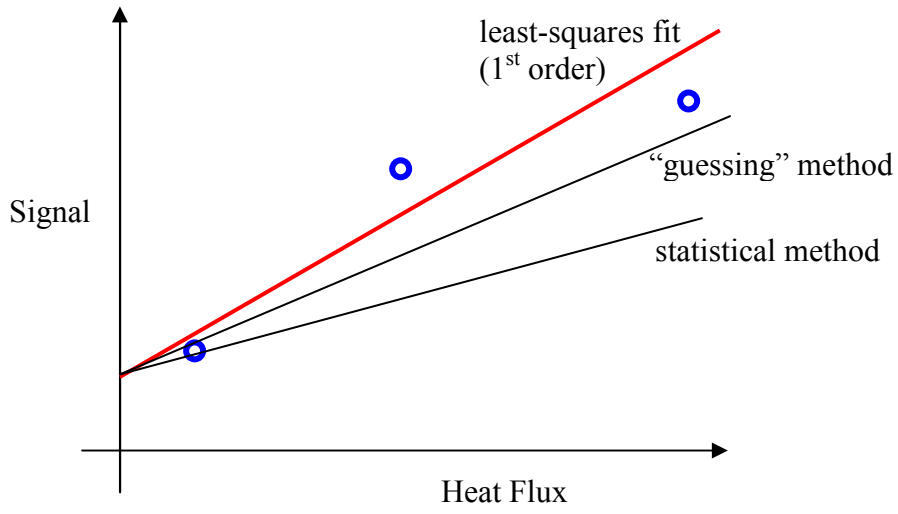

Figure 4.16. A hypothetical comparison of the bias in each method.

The statistical method may not be perfect, but it ultimately was chosen to represent the uncertainty in the measured data. However, as shown in Figure 4.15, the data is still not overlapping the predicted curve. The uncertainty in the heat flux was estimated next. The actual data sets from each angle with the uncertainty from each method can be found in Appendix A.

4.5.3 Uncertainty in the Measured Heat Flux

Perhaps the largest source of uncertainty is in the estimate of the amount of heat flux that goes through the device. Recall that the last three data sets were obtained after insulation was applied to the heater, and there was a significant rise in the output voltage. This was because more of the heat produced by the heater was going through the device (less was escaping to the surroundings). Unfortunately there is no way to determine exactly how much error was involved, because the heat released to the environment was not measured. Two methods were used to attempt to analyze the uncertainty in the amount of heat flux that went through the device.

4.5.3.1 Method 1 – Using Temperature Data

Since the temperature across the device was measured for each test, the heat flux through the device should be easy to calculate using Fourier's Law:

$$q'' = -k_z \nabla_z T \tag{4.12}$$

where k_z is the effective thermal conductivity of the device in the direction of heat flow (see Equation 4.7) and $\nabla_z T$ is the temperature gradient in the direction of heat flow, and is simply equal to the temperature difference divided by the distance in that direction. Using this equation, the heat flux across the device can be determined by using experimental temperature data, as shown in Figure 4.17. It is clear in the plot that the output voltage is different when the heat flux is calculated using the temperature difference (a different value of heat flux results in a different value being calculated from the least-squares fit for each angle). In fact, the data show that in most cases the heat flux is lower when calculated using the temperature difference. If this is assumed to be the "true" value of the heat flux, then it follows that the heater is actually producing a larger heat flux than it should be (when calculated using the power input to the heater). Clearly there is some problem when calculating the heat flux using Fourier's Law, because the

heat flux that actually goes through the device must always be smaller than the heat flux calculated using the electrical power input to the heater, due to convective losses.

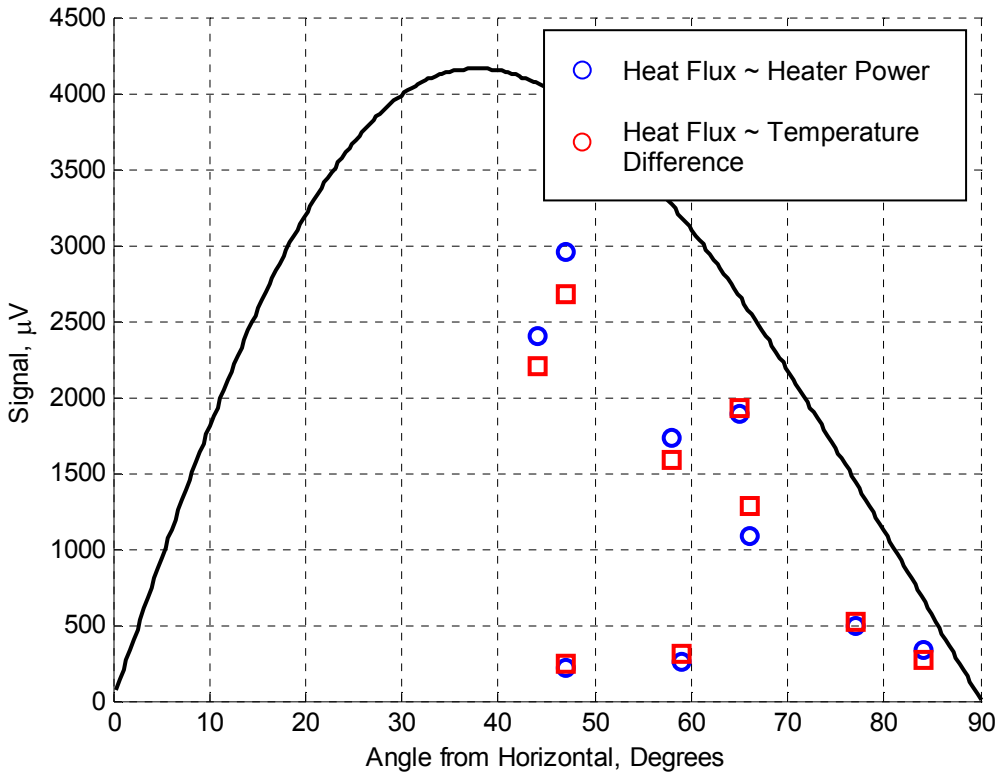

Figure 4.17. Comparison of the data when the heat flux is calculated by the two methods. The blue points indicate when the heat flux is calculated from the electrical power input to the heater, and the red points indicate when the heat flux is calculated from the thermocouple data.

There are two possible explanations to this problem. The first is that the material properties used to calculate k_z are inaccurate, i.e. either k_{Bi} or $k_{Bi_2Te_3}$ or both are too low. This is possible, but the more probable explanation is that the temperature data from the thermocouples are inaccurate. Figure 4.18 shows how the thermocouples were placed during testing. The thermocouples were not placed directly on the surface of the device, but were buried in the thermal paste between the device and the ceramic plates. The paste has a small value of thermal conductivity, and it was thought that this placement would ensure accurate temperature readings. Also, there may have been local changes in temperature depending on which layer the thermocouple was placed. The "average" thermal conductivity of the device is calculated as k_z, but the individual layers still retain there own values of k.

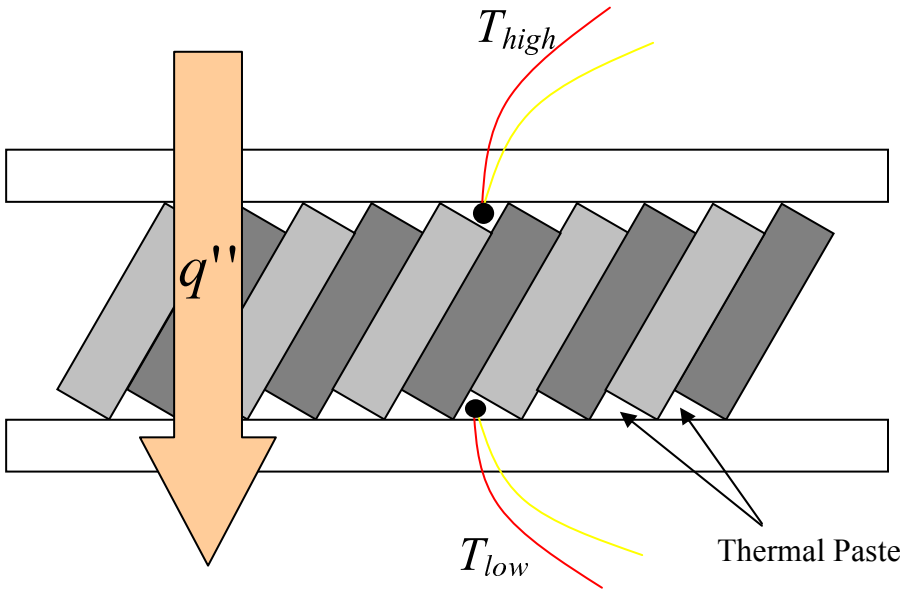

Figure 4.18. A schematic of the thermocouple placement in the test setup.

Figure 4.18 shows that the placement of the thermocouples probably resulted in the recorded temperature difference being larger than the actual temperature difference, resulting in the actual heat flux through the device being smaller than the heat flux calculated using Fourier's Law. Thus, it was decided that the method of calculating the heat flux using the electrical power to the input was more accurate, despite the fact that this method does not include the effects of convection.

4.5.3.2 Method 2 – Simple Analysis of Convective Losses

In order to estimate the heat lost from the heater before going through the device, a first-order approximate model was developed to estimate convective losses (radiative losses were neglected because of the relatively low temperatures involved). Figures 4.19 and 4.20 outline the resistance networks and equations used to solve for the heat flux through the device.

With Insulation

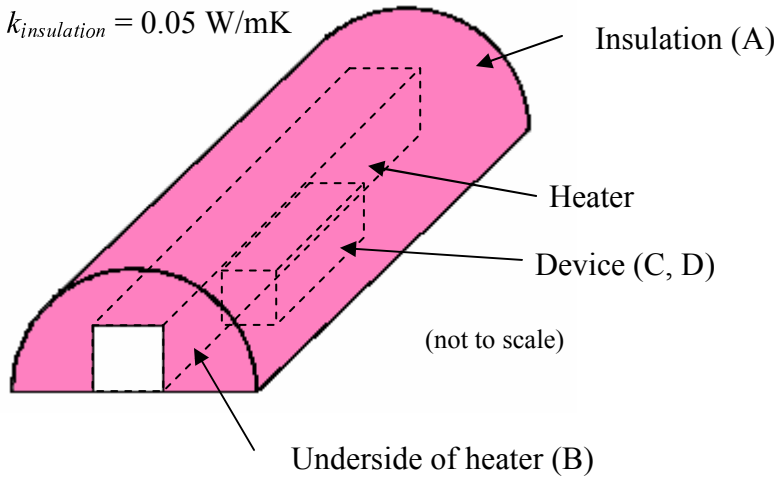

4 Paths for Heat:

A – Conducted through insulation, convected to air
B – Convected through bare spots on the heater
C – Convected from sides of device
D – Conducted through device to heat sink

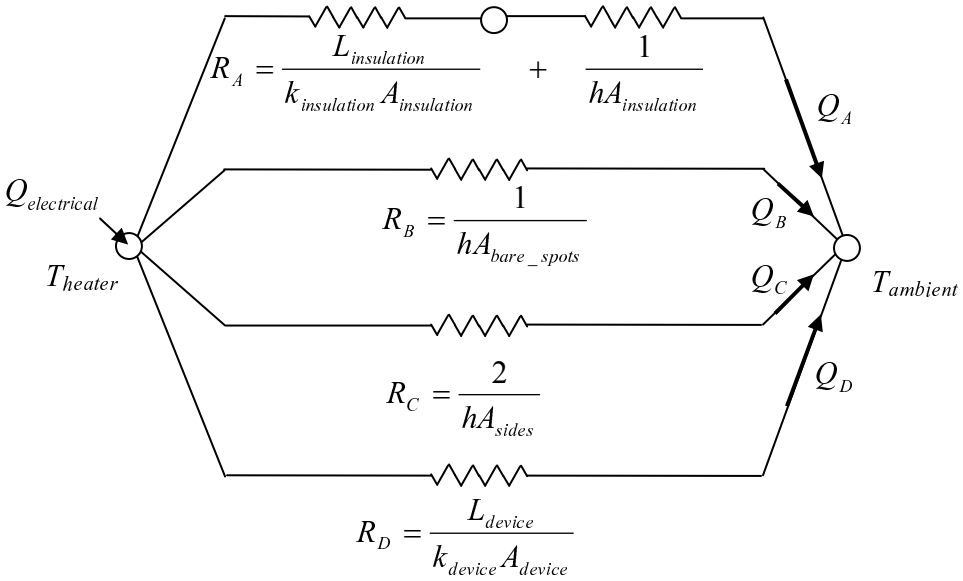

$$T_{heater} - T_{ambient} = Q_A R_A = Q_B R_B = Q_C R_C = Q_D R_D$$

$$Q_{electrical} = Q_A + Q_B + Q_C + Q_D = Q_D \frac{R_D}{R_A} + Q_D \frac{R_D}{R_B} + Q_D \frac{R_D}{R_C} + Q_D$$

$$Q_D = \frac{Q_{electrical}}{R_D\left(\frac{1}{R_A} + \frac{1}{R_B} + \frac{1}{R_C} + \frac{1}{R_D}\right)} \approx 0.9\, Q_{electrical}$$

Figure 4.19. Outline of the resistive network and equations used to solve for the amount of heat that goes through the device when insulation was used.

Without Insulation

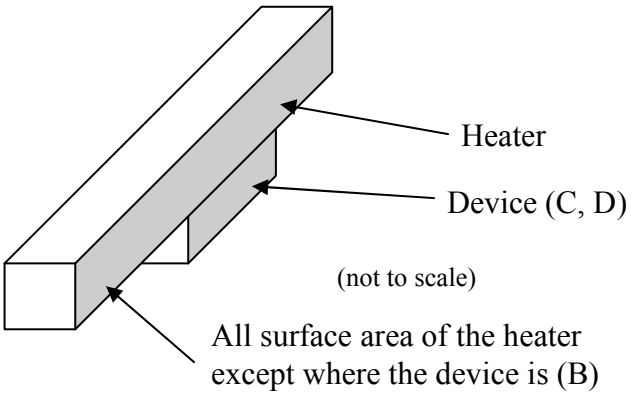

3 Paths for Heat:

B – Convected through bare spots on the heater
C – Convected from sides of device
D – Conducted through device to heat sink

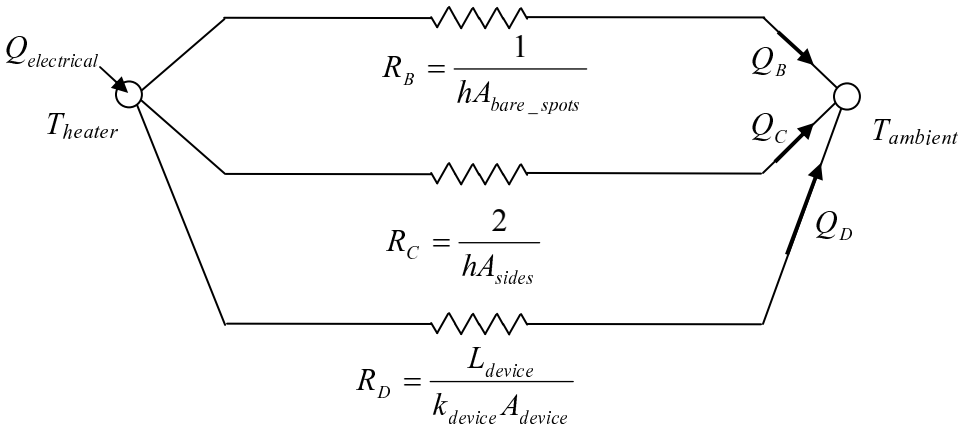

$$T_{heater} - T_{ambient} = Q_B R_B = Q_C R_C = Q_D R_D$$

$$Q_{electrical} = Q_B + Q_C + Q_D = Q_D \frac{R_D}{R_B} + Q_D \frac{R_D}{R_C} + Q_D$$

$$Q_D = \frac{Q_{electrical}}{R_D\left(\frac{1}{R_B} + \frac{1}{R_C} + \frac{1}{R_D}\right)} \approx 0.8\, Q_{electrical}$$

Figure 4.20. Outline of the resistive network and equations used to solve for the amount of heat that goes through the device when insulation was not used.

An angle of $\alpha = 65°$ was used for Figures 4.19 and 4.20, and the electrical input to the heater was 2 W. The rough estimate was that about 90% of the heat goes through the device when insulation is used on the heater, and about 80% of the heat goes through the device when insulation is not used (a convective heat transfer coefficient of 15 W/m^2K was used). Note that the "2" in the thermal resistance of the sides of the device comes from the fact that the average temperature of the sides is halfway between the heater temperature and the ambient temperature. Table 4.5 shows a summary of the convective heat losses at each surface for both cases (with and without insulation).

Table 4.5. Summary of the results from the analysis of the effects of convection. The heater power for each case is 2 W, the convective heat transfer coefficient is 15 W/m^2K, and the device has an angle of 65°.

	A (Insulation)	**B (Heater)**	**C (Sides)**	**D (Device)**
R_i (K/W) with insulation	174.8	207.4	386.1	9.25
Q_i with insulation (W)	0.0943	0.0795	0.0427	1.783
% of $Q_{electrical}$ with insulation	4.72 %	3.98 %	2.14 %	**89.2 %**
R_i (K/W) with no insulation	-	40.02	386.1	9.25
Q_i with no insulation (W)	-	0.368	0.0382	1.594
% of $Q_{electrical}$ with no insulation	-	18.4 %	1.91 %	**79.7 %**

4.5.3.3 The Effects of Uncertainty in the Heat Flux

If the nominal material properties of the device are assumed to be correct, curves can be drawn with several different estimates of heat loss to the surrounding air. Figure 4.21 shows the results of such speculation. Dashed lines are added to show what the predicted values of the output voltage would be if only a fraction of the heat produced by the heater actually flows into the device.

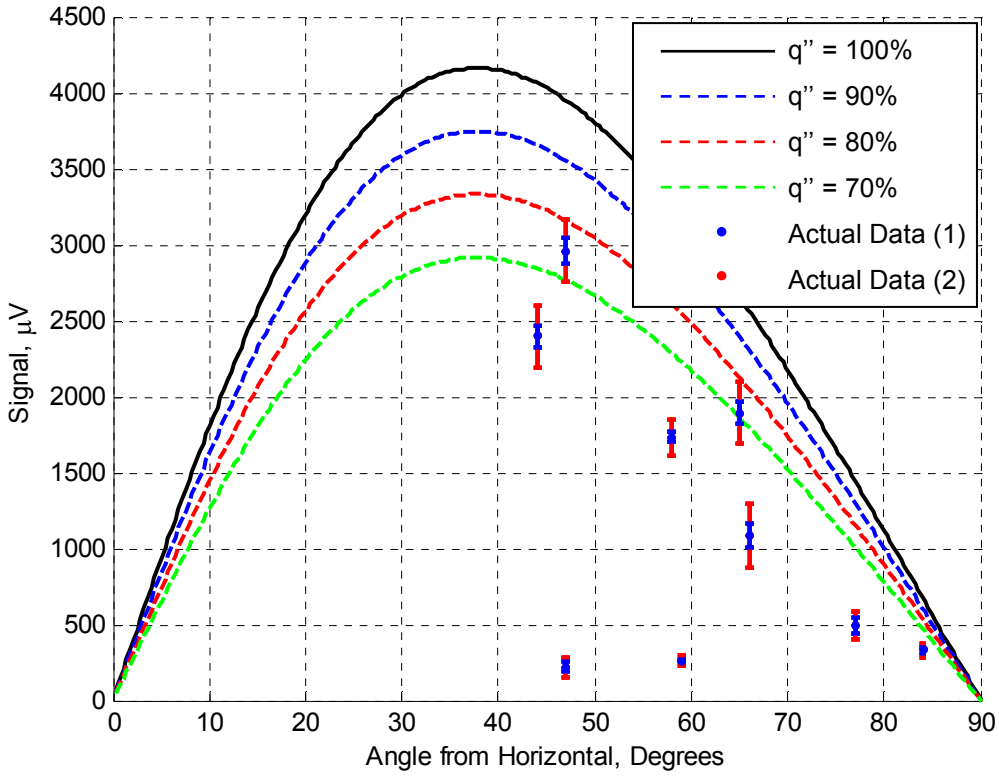

Figure 4.21. The possible uncertainty in the heat flux that flows through the device shows that the data may be close to the predicted values.

Figure 4.21 shows that with a certain amount of uncertainty in the heat flux, the data may be within the range of the predicted values. For instance, two of the points for which insulation were used are above the 70% curve, meaning that these values would be close to correct if the heat flux going through the device was between 70% and 80% of the amount of heat produced by the heater. It is difficult to tell if this is a reasonable amount of uncertainty in the amount of heat flux. The previous section estimated the percentage of heat flux that went through the device, and the rough estimations of the convective heat transfer coefficient and the thermal conductivity of the insulation resulted in the heat flux going through the device to be 90% of the total heat flux when insulation was used and 80% when the insulation was not used. Figure 4.21 shows that these amounts are still too large, but the assumptions are rough and may be too conservative.

4.6 Alternate Plotting Methods

The data in this report have been presented in plots where a specific value of heater power was chosen. That amount of heater power was used to calculate the heat flux at each angle for the predicted curve, and to select the appropriate data point from each least-squares line. The amount of heat flux at each angle is slightly different because the area of the device changes with angle. An alternate method of plotting the data is to simply plot the sensitivity (voltage / heat flux) of the device at each angle. This method is more helpful in an engineering sense, since it more precisely compares the performance of the device at several angles to the expected performance. However, there are certain subtleties that cause this method to have disadvantages. Figure 4.22 shows the plot of device sensitivity vs. angle.

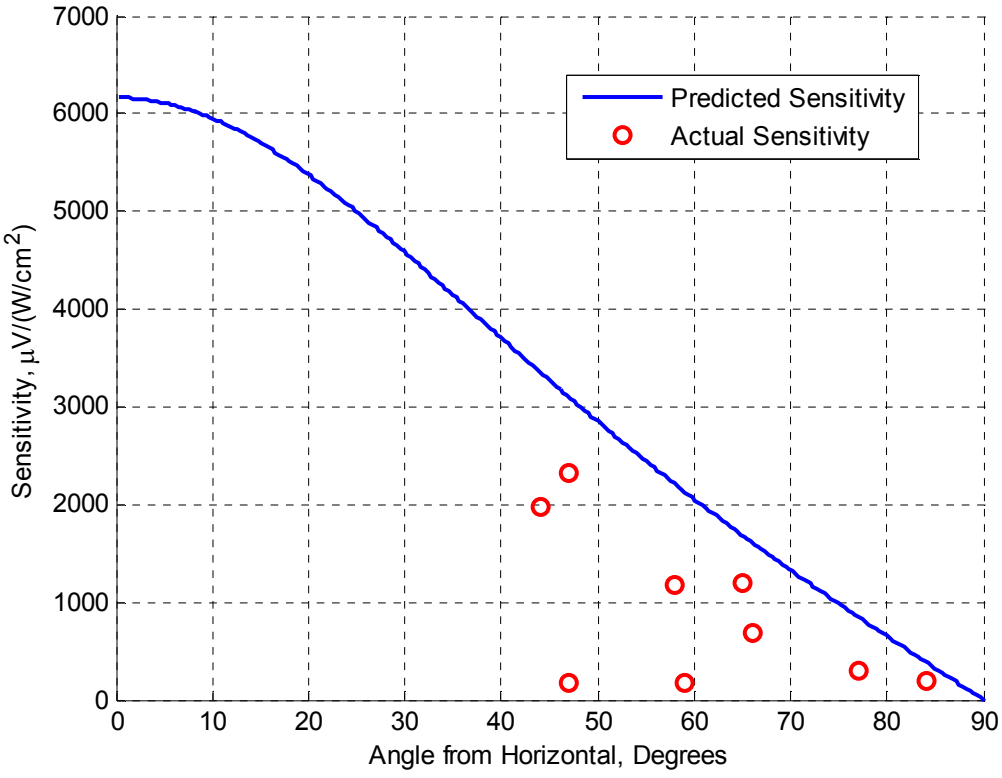

Figure 4.22. The comparison of predicted and actual values when calculated as sensitivities rather than voltages at a certain heater power.

The major downfall of this method is that it breaks down at small angles due to the geometry of the device. Recall that the equations used to predict the output voltage of the device were adapted from Ref. 10, where the device was made by cutting a rectangular piece from a stack of sintered foils. Therefore, in Ref. 10, the device was always the same size and shape for each angle. In this work, the device was constructed from rectangular layers, and therefore had an irregular shape that changed with each angle (see Fig. 4.10). The plotting method of selecting a specific value of heat flux eliminates the geometrical problems due to the shape of the device, while the method of plotting the device sensitivity does not.

If the heat flux is set to a specific value, the signal is calculated from Eq. 4.12,

$$V = \tfrac{1}{2}\sin 2\alpha\left(S_{\parallel} - S_{\perp}\right)\frac{q''}{k_z}L \tag{4.12}$$

where the heat flux q'' is calculated by dividing the heater power by the area of the device (again, assuming that all the heat goes through the device). The area is simply the length L of the device times the width W. The equation for the output voltage is then reduced to

$$V = \tfrac{1}{2}\sin 2\alpha\left(S_{\parallel} - S_{\perp}\right)\frac{Q}{W \cdot k_z} \tag{4.13}$$

where Q is the heater power. There are no geometrical dependencies left in this equation, and so it behaves as expected, with zero voltage output at 0° and 90° (where there are no transverse effects) and a maximum value somewhere in between.

If the sensitivity of the device is calculated, Eq. 4.12 is simply divided by the heat flux:

$$S = \frac{V}{q''} = \tfrac{1}{2}\sin 2\alpha\left(S_{\parallel} - S_{\perp}\right)\frac{L}{k_z} \tag{4.14}$$

This is still a valid way to calculate the output voltage of the device, but the L that remains in the equation presents a problem. Recall that the length of the device was calculated as

$$L = \frac{n \cdot t}{\sin \alpha} \tag{4.15}$$

where n is the number of layers, t is the thickness of each layer, and α is the angle of the device. The equation is thus not valid for small angles, where L tends to get very large. For moderate angles this is somewhat valid because the length of the device does increase with decreasing α, but it is unknown how accurate this method is since the smallest angle tested was 44°.

As shown in Figure 4.22, this alternate method results in about the same amount of error between the predicted and actual values, but it is nonsensical at small angles. This method makes more sense for engineering uses, but the geometry of the device prevents it from being as effective as the original method of choosing a specific value of heater power.

4.7 Summary

The device was tested for its heat flux sensing capabilities by setting it to nine different angles and taking steady state measurements of its output voltage when subjected to known heat fluxes. The results were fairly linear, and repeatable from day to day. However, there were inconsistencies between angles due to unknown errors in the preparation of the device. Insulation was added to the heater for the last few tests to improve the assumption that all the heat was flowing through the device.

The experimental results from testing were compared to values of the output voltage predicted from theory. The data followed the same trend of the predicted values, but there was a significant gap between the two. An uncertainty analysis was performed

to see if the data would match the predicted values under certain conditions, and it was concluded that the most likely source of error was the measured heat flux.

The results matched the general shape of the predicted values, but a more refined process of constructing and testing the device would almost certainly result in more accurate data. A thorough discussion of possible improvements is presented in the next chapter.

Chapter 5 – Conclusions and Recommendations

5.1 Summary of Results and Analysis

Although the transverse multilayered device did not display thermoelectric cooling effects, its capabilities as a heat flux sensor were tested extensively. A simple method for testing the device was devised, and the data was collected and compared to calculated predictions. The results tended to follow the same trends as the calculated values, but there were significant gaps between the magnitudes of the actual signals and the predicted values. This was partly explained through uncertainty analysis of the material properties and the linearity of the actual data, but was most likely due to the uncertainty in the amount of heat flux that was flowing through the device. Future projects may get more accurate results if closer attention is paid to these uncertainties. For example, the properties used in the calculations should be measured rather than taken from literature. To eliminate uncertainties related to convective losses, the tests should be performed in a vacuum.

All of the experimental results from heat flux testing on the multilayered device can be found in Appendix A, but a summary plot is shown in Figure 5.1. The solid black curve indicates the predicted values of the output voltage (as calculated using equations modified from Ref. 10), the red dotted lines indicate the maximum and minimum values of the output voltage based on 15% uncertainties in all the material properties, and the blue points with error bars indicate the actual data points with maximum and minimum values based on a 90% confidence interval. The horizontal axis indicates the angle of inclination of the device. The output voltage of the device depends on the angle because the angle is included in the Seebeck tensor, which determines the Seebeck coefficient of the device in the transverse direction based on the material properties of the constituent materials and the geometry of the device. The maximum output is not at exactly 45° because the thermal conductivity of the device depends on the angle, and because the geometry of the device changes with the angle.

In Figure 5.1, the three data points closest to the line were tested using insulation on the heater to decrease heat loss through the top and sides of the heater. The four "middle" points were gathered before the insulation was added, and it has been determined that the two "bottom" points are erroneous in some way and their inconsistencies are not due to thermoelectric effects. It can be seen that the largest source of error was most likely the calculation of the heat flux going through the device. When insulation was added, the signal got much closer to the predicted value, and it seems that with a perfectly insulated heat source (or a better way of determining the amount of heat flux going through the device), the data points would lie very close to the predicted curve.

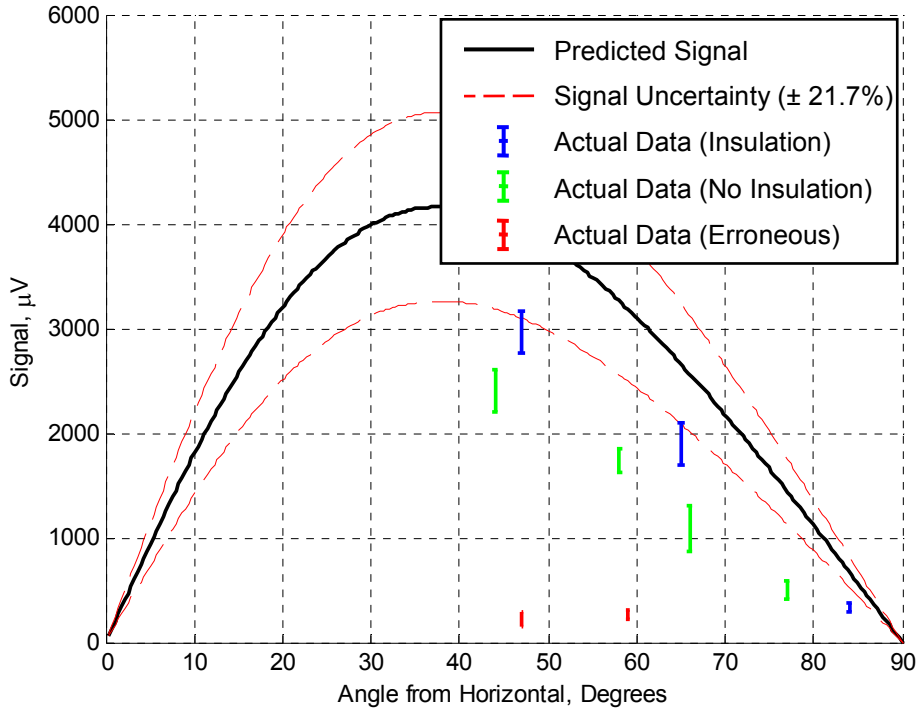

Figure 5.1. The final form of the comparison of actual data and predicted values at a heater power of 2 W. Uncertainties in material properties and actual measurements were taken into account, but there is unknown uncertainty in the amount of heat flux that actually reaches the device.

5.2 Achievements of the Project

Other than the data collected, there were many valuable achievements during the course of this project. Simple techniques were developed for measuring the cooling and

heat flux sensing capabilities of thermoelectric devices and materials. Information regarding the thermoelectric properties of bismuth and bismuth telluride was gathered. Equations were modified from Ref. 10 to analyze the results, and a simple uncertainty analysis revealed many possible improvements to the process. The data and knowledge collected in this project could lead to the construction of a more reliable and accurate multilayered device, or eventually to a prototype thin-film device that could display characteristics that rival those of current thermoelectric technology.

5.3 Recommendations

There are several parts of the project that could be improved. Of course, many improvements were made along the way, but several other improvements could still be made. Below is a list of improvements that would be implemented if the project were to be started anew with the knowledge already gained.

- The most important improvement would be a better way of determining the amount of heat flux that actually flows through the device. Perhaps a thin-film heat flux sensor could be placed between the heater and the device. The output from this sensor would directly relay the amount of heat flux flowing into the device, although a small amount would still leak from the sides of the device. Alternatively, the tests could be performed in a vacuum to eliminate convection.
- An improved way to measure the temperature of the top and bottom sides of the device while testing is needed. This is not as important as measuring the heat flux, but may be helpful in determining certain characteristics of the device.
- The individual properties of the constituent materials should be measured rather than taken from references. This would decrease the amount of uncertainty in the calculated values. Another improvement would be a process by which the properties of the device can be measured after it has been constructed. These values could then be directly added to the equations rather than estimated from the properties of the constituents.

- The bismuth layers need to be replaced with another metal that has a higher melting temperature if the indium film is to be used to connect the layers. The localized melting in the bismuth layers was detrimental to the structure and possibly the performance of the device. Any metal will do, so long as the thermoelectric properties are sufficiently different from those of bismuth telluride. In fact, this may actually lead to a larger signal, because normal metals have Seebeck coefficients near zero. The difference between the Seebeck coefficients of the two constituents would then be larger.
- The layers should be coated with a thin film of nickel to prevent diffusion of the indium film into the thermoelectric materials. This may or may not have been a problem with the device in this project.
- More care should be taken when collecting steady state data. Even though the points for most of the angles are close to the least-squares fits, the small discrepancies at low heat flux levels cause large uncertainties to arise.
- If possible, the device should be regularly shaped, i.e. parallelograms rather than rectangles, as in Ref. 10 (see Figure 4.1). This would eliminate the ambiguities involved in the geometry in the device, but would prevent the process of re-melting the device and changing the angle at will. Several devices would have to be built, which may be inconvenient and/or impractical.

5.4 Conclusions

The results of this work indicate that the device displays transverse thermoelectric properties. The data follow the trend of calculated values, although significant sources of uncertainty prevented an accurate match between experimental results and calculated values. Further research is needed to determine whether transverse devices, whether they are made of layers of thermoelectric materials or thin films, can compete with more traditional devices for cooling and heat flux sensing.

References

[1] R. Venkatasubramanian, E. Siivola, T. Colpitts, and B. O'Quinn, "Thin-film thermoelectric devices with high room-temperature figures of merit," Nature, Vol. 413, 2001, pp. 597–602.

[2] Marlow Industries, "Product Description – Single Stage Coolers," http://www.marlow.com/Products/productlist.asp?ProductType=10&SubType=0, (Dallas, TX).

[3] T. E. Diller, "Heat Flux," The Measurement, Instrumentation, and Sensors Handbook, CRC Press, Boca Raton, 1999, pp. 34-1–34-15.

[4] Jet Propulsion Laboratory, "Radioisotope Thermoelectric Generators," http://voyager.jpl.nasa.gov/spacecraft/instruments_rtg.html, (Pasadena, CA).

[5] Jet Propulsion Laboratory, "Cassini-Huygens: Mission to Saturn & Titan," http://saturn.jpl.nasa.gov/spacecraft/safety.cfm, (Pasadena, CA).

[6] National Aeronautics and Space Administration, "Human-Implantable Thermoelectric Devices," http://www.nasa.gov/centers/ames/research/technology-onepagers/human_devices.html, (Ames Research Center, Moffett Field, CA).

[7] T. S. Gudkin and E. É. Fiskind, "Response time of a thermal converter with a synthetic anisotropy," Sov. Tech. Phys. Lett., Vol. 4, No. 7, 1978, pp. 844–847.

[8] T. S. Gudkin, E. K. Iordanishvili, and E. É. Fiskind, "Transverse cooling effect in a statefied medium with artificial anisotropy," Sov. Tech. Phys. Lett., Vol. 4, No. 5, 1978, pp. 607–610.

[9] V. P. Babin, T. S. Gudkin, Z. M. Dashevskii, L. D. Dudkin, E. K. Iordanishvili, V. I. Kaidanov, N. V. Kolomoets, O. M. Narva, and L. S. Stil'bans, "Anisotropic synthetic thermoelements and their maximum capabilities," Sov. Phys. Semicond., Vol. 8, No. 4, 1974, pp. 748–753.

[10] Th. Zahner, R. Förg, and H. Lengfellner, "Transverse thermoelectric response of a tilted metallic multilayer structure," Appl. Phys. Lett., Vol. 73, No. 10, 1998, pp. 1364–1366.

[11] T. J. Seebeck, Magnetische Polarisation der Metalle und Erzedurch Temperatur-Differenz. Abhand Deut. Akad. Wiss. Berlin, 1822, pp. 265–373.

[12] J. C. Peltier, Nouvelles experiences sur la caloriecete des courans electriques. Ann. Chem., LVI, 1834, pp.371–387.

[13] E. Altenkirch, Physikalische Zeitschrift, Vol. 12, 1911, pp. 920–924.

[14] D. M. Rowe, CRC Handbook of Thermoelectrics, CRC Press, Boca Raton, 1994.

[15] R. F. Service, "Temperature rises for devices that turn heat into electricity," Science, Vol. 306, 2004, pp. 806–807.

[16] O. Yamashita and S. Tomiyoshi, "Bismuth telluride compounds with high thermoelectric figures of merit," J. Appl. Phys., Vol. 93, No. 1, 2003, pp. 368–374.

[17] I. Stark and M. Stordeur, "New micro thermoelectric devices based on bismuth telluride – type thin solid films," 18th Intl. Conf. on Thermoelectrics, 1999, pp. 465–472.

[18] T. C. Harman, P. J. Taylor, M. P. Walsh, and B. E. LaForge, "Quantum dot superlattice thermoelectric materials and devices," Science, Vol. 297, 2002, pp. 2229–2232.

[19] A. Majumdar, "Thermoelectricity in semiconductor nanostructures," Science, Vol. 303, 2004, pp. 777–778.

[20] D. Vashaee and A. Shakouri, "Improved thermoelectric power factor in metal-based superlattices," Phys. Rev. Lett., Vol. 92, No. 10, 2004, pp. 106103-1–106103-4.

[21] W. Thomson (Lord Kelvin), Mathematical and Physical Papers, Vol. 1, Cambridge Univ. Press, 1882, pp. 266.

[22] V. I. Kaidanov, V. A. Tselishchev, A. P. Usov, L. D. Dudkin, B. K. Voronov, and N. N. Trusova, "Anisotropy of the transport properties of chromium disilicide," Sov. Phys. Semicond., Vol. 4, No. 7, 1970, pp. 1338–1345.

[23] S. L. Korolyuk, I. M. Pilat, A. G. Samoĭlovich, V. N. Slipchenko, A. A. Snarskiĭ, and E. F. Tsar'kov, "Anisotropic thermoelements," Sov. Phys. Semicond., Vol. 7, No. 4, 1973, pp. 725–733.

[24] A. G. Samoĭlovich and A. A. Snarskiĭ, “Investigation of thermoelectric eddy currents,” Sov. Phys. Semicond., Vol. 13, No. 8, 1979, pp. 1539–1547.

[25] T. S. Gudkin, E. K. Iordanishvili, and E. É. Fiskind, “Theory of an anisotropic thermoelectric cooling unit,” Sov. Phys. Semicond., Vol. 11, No. 9, 1977, pp. 1790–1794.

[26] L. I. Bytenskiĭ, T. S. Gudkin, E. K. Iordanishvili, and E. É. Fiskind, “Anisotropic thermoelectric cooling unit in a magnetic field,” Sov. Phys. Semicond., Vol. 12, No. 3, 1978, pp. 538–542.

[27] V. N. Slipchenko and A. A. Snarskiĭ, “Influence of the anisotropy of the thermal conductivity on the transverse thermoelectric power,” Sov. Phys. Semicond., Vol. 8, No. 10, 1974, pp. 2010–2013.

[28] O. Ya. Luste and A. G. Samoĭlovich, “Influence of the thermal conductivity anisotropy on the transverse thermoelectric power,” Sov. Phys. Semicond., Vol. 11, No. 1, 1977, pp. 209–211.

[29] A. A. Snarskiĭ, “Thermo-emf of anisotropic thermoelements. I. Rectangular elements,” Sov. Phys. Semicond., Vol. 11, No. 10, 1977, pp. 2053–2055.

[30] A. G. Samoĭlovich and V. N. Slipchenko, “The emf of an anisotropic thermoelement,” Sov. Phys. Semicond., Vol. 9, No. 3, 1975, pp. 594–596.

[31] O. S. Gorya and E. F. Lupashko, “Optimization of the figure of merit of a thermoelement with a deliberately induced anisotropy,” Sov. Phys. Semicond., Vol. 13, No. 2, 1979, pp. 340–343.

[32] H. Lengfellner, G. Kremb, A. Schnellbögl, J. Betz, K. F. Renk, and W. Prettl, “Giant voltages upon surface heating in normal $YBa_2Cu_3O_{7-\delta}$ films suggesting an atomic layer thermopile,” Appl. Phys. Lett., Vol. 60, No. 4, 1992, pp. 501–503.

[33] L. R. Testardi, “Anomalous laser-induced voltages in $YBa_2Cu_3O_x$ and ‘off-diagonal’ thermoelectricity,” Appl. Phys. Lett., Vol. 64, No. 18, 1994, pp. 2347–2349.

[34] S. Zeuner, W. Prettl, and H. Lengfellner, “Fast thermoelectric response of normal state $YBa_2Cu_3O_{7-\delta}$ films,” Appl. Phys. Lett., Vol. 66, No. 14, 1995, pp. 1833–1835.

[35] W. M. Huber, S. T. Li, A. Ritzer, D. Bäuerle, H. Lengfellner, and W. Prettl, "Transverse Seebeck effect in $Bi_2Sr_2CaCu_2O_8$," Appl. Phys. A, Vol. 64, 1997, pp. 487–489.

[36] Th. Zahner, R. Schreiner, R. Stierstorfer, O. Kus, S. T. Li, R. Roessler, J. D. Pedarnig, D. Bäuerle, and H. Lengfellner, "Off-diagonal Seebeck effect and anisotropic thermopower in $Bi_2Sr_2CaCu_2O_8$ thin films," Europhys. Lett., Vol. 40, No. 6, 1997, pp. 673–678.

[37] A. A. Snarskiĭ, A. M. Pal'ti, and A. A. Ashcheulov, "Anisotropic thermocouples article," Semiconductors, Vol. 31, No.11, 1997, pp. 1281–1298.

[38] N. Mateeva, H. Niculescu, J. Schlenoff, and L. Testardi, "Thermoelectric begavior of conducting polymers: On the possibility of 'off-diagonal' thermoelectricity," Mat. Res. Soc. Symp. Proc., Vol. 478, 1997, pp. 243–248.

[39] K. Fischer, C. Stoiber, A. Kyarad, H. Lengfellner, "Anisotropic thermopower in tilted metallic multilayer structures," Appl. Phys. A, Vol. 78, 2004, pp. 323–326.

[40] S. Cho, Y. Kim, A. DiVenere, G. K. L. Wong, and J. B. Ketterson, "Anisotropic Seebeck and magneto-Seebeck coefficients of Bi and $Bi_{0.92}Sb_{0.08}$ alloy thin films," J. Appl. Phys., Vol. 88, No. 2, 2000, pp. 808–812.

[41] Vatell Corporation, "Heat Flux Transducers," http://www.vatell.com/HF%20Sensors.htm, (Christiansburg, VA).

[42] R. S. Figiola and D. E. Beasley, Theory and Design for Mechanical Measurements, 2nd Edition, John Wiley and Sons, Inc., New York, 1995.

Appendix A – Heat Flux Sensing Data

This appendix shows the data from all nine angles tested with the multilayered device built with indium film connections. The first plot shows the data used to calculate the signal strength for every angle. Following are plots and tables for each individual angle. In each case, the first plot shows all data taken for that angle, and the second plot shows the truncated data. Recall that the data from the first few days for several angles was discarded because the steady state results were not consistent in that time period.

The plots of the truncated results also show the results of uncertainty analysis. The red dashed lines indicate the maximum and minimum values of the slope from the "guessing" method (method 1), while the blue dashed lines indicate the maximum and minimum values of the slope from the statistical method (method 2), using a 90% confidence level. Individual points on any plot correspond to one steady state test.

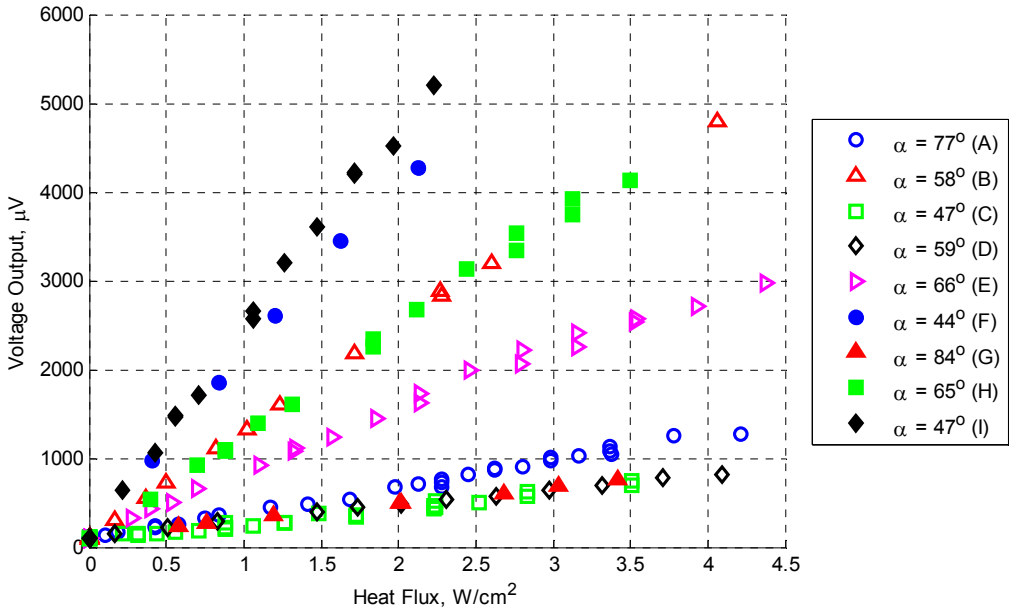

Figure A.1. All useable heat flux sensing data from each of the nine tested angles.

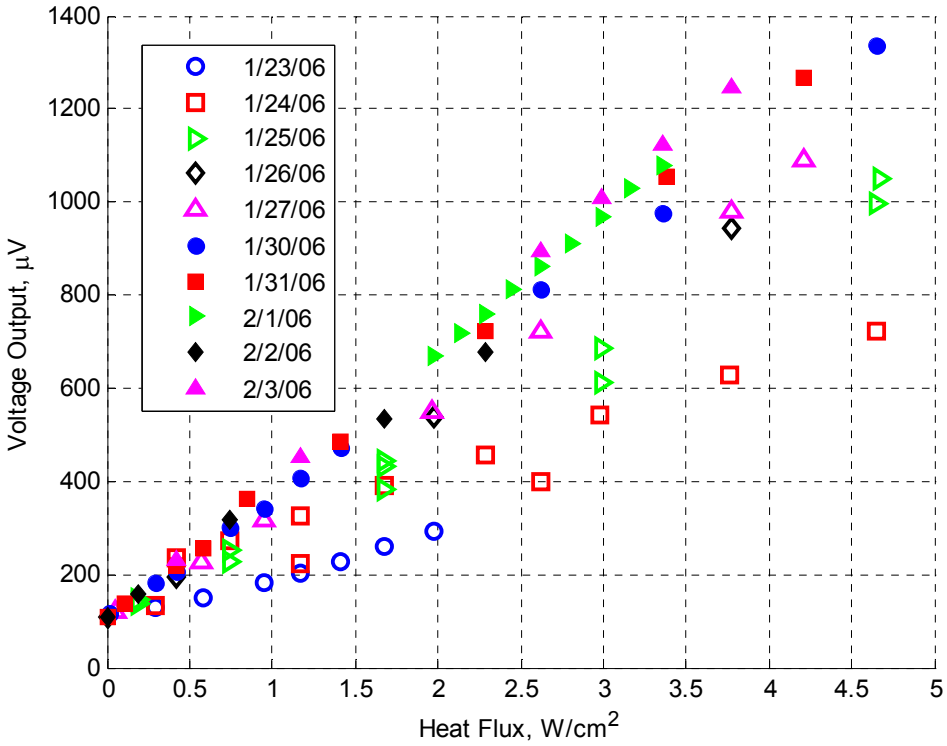

Figure A.2. All data from steady state heat flux sensing tests with the angle α = 77° (A).

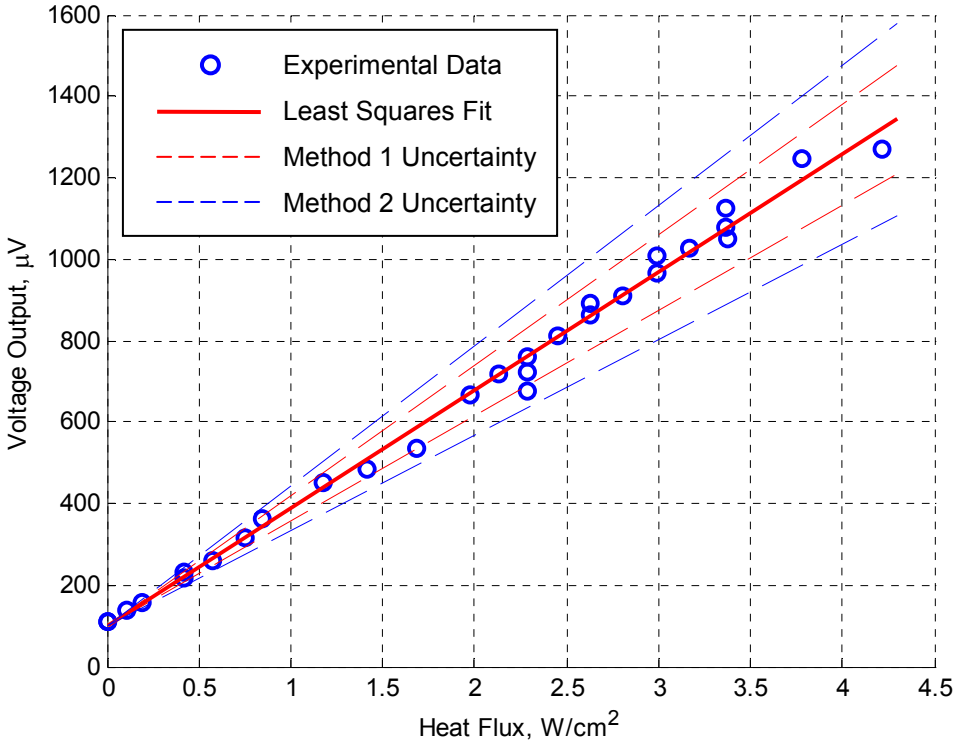

Figure A.3. Truncated data from the angle α = 77° (A). The slope of the least-squares fit is 289.9 μV/(W/cm^2) and the uncertainties from method 1 and method 2 are ±10% and ±17.6% respectively.

Table A.1. Comprehensive tabular data from heat flux sensing tests with α = 77° (A).

	run #	Power (W)	Heat Flux (W/cm^2)	T_{high} (°C)	T_{low} (°C)	Δ T (°C)	Voltage (μV)
jan 23rd	1	0.345	0.293	29.03	25.21	3.82	129.2
	2	0.679	0.577	32.67	25.98	6.69	150.6
	3	1.116	0.948	37.99	27.32	10.67	183.9
	4	1.38	1.172	41.17	28.19	12.99	203.8
	5	1.661	1.411	44.88	29.19	15.69	228.6
	6	1.98	1.682	48.84	30.20	18.64	258.8
	7	2.327	1.976	52.89	31.35	21.54	293.7
jan 24th	1	0.345	0.293	28.75	24.91	3.85	133.5
	2	1.380	1.172	41.13	27.94	13.19	221.3
	3	3.090	2.624	62.86	34.14	28.71	398.5
	4	5.480	4.654	86.87	39.80	47.08	721.9
	5	4.428	3.761	77.65	38.25	39.40	628.8
	6	3.504	2.976	69.00	36.33	32.67	542.7
	7	2.688	2.283	61.13	34.44	26.69	458.1
	8	1.980	1.682	54.16	32.66	21.50	390.0
	9	1.380	1.172	48.29	31.19	17.11	324.3
	10	0.880	0.747	43.15	29.78	13.37	273.4
	11	0.498	0.423	39.16	28.64	10.52	237.0
jan 25th	1	0.220	0.187	28.19	25.47	2.72	137.8
	2	0.880	0.747	36.34	27.44	8.90	226.0
	3	1.980	1.682	49.90	30.91	19.00	384.7
	4	3.520	2.989	68.63	35.76	32.87	613.7
	5	5.480	4.654	91.73	41.60	50.13	997.2
	6	3.520	2.989	69.37	36.31	33.06	684.4
	7	1.980	1.682	50.95	31.63	19.33	432.1
	8	0.880	0.747	37.48	28.23	9.25	252.6
	9	0.220	0.187	29.11	25.93	3.18	147.2
	10	1.980	1.682	50.70	31.53	19.17	442.3
	11	5.500	4.671	91.93	41.99	49.94	1048.9
jan 26th	1	0.000	0.000	25.39	24.72	0.68	107.6
	2	0.498	0.423	31.58	26.20	5.38	195.5
	3	2.327	1.976	54.12	31.96	22.17	537.0
	4	4.446	3.776	79.94	38.64	41.30	943.7
jan 27th	1	4.446	3.776	80.22	38.58	41.64	982.0
	2	2.314	1.965	54.98	32.51	22.47	551.4
	3	0.672	0.571	34.34	27.26	7.09	228.9
	4	0.056	0.048	26.46	25.21	1.25	118.9
	5	1.116	0.948	39.63	28.43	11.21	316.1
	6	3.090	2.624	63.95	34.50	29.46	722.2
	7	4.959	4.212	86.21	40.15	46.06	1092.5
jan 30th	1	0.498	0.423	31.32	25.88	5.44	206.5
	2	3.961	3.364	74.66	36.92	37.74	975.1
	3	1.116	0.948	39.99	28.47	11.52	343.0
	4	0.014	0.012	26.05	24.95	1.10	116.8
	5	0.345	0.293	30.14	25.90	4.24	183.1

	6	5.480	4.654	92.79	41.76	51.02	1334.6
	7	1.370	1.164	43.75	29.88	13.87	406.5
	8	1.661	1.411	47.03	30.45	16.58	470.8
	9	3.090	2.624	64.51	34.76	29.76	812.4
	10	0.880	0.747	37.39	28.12	9.27	299.6
jan 31st	1	0.498	0.423	32.31	26.85	5.46	217.1
	2	2.688	2.283	59.57	33.71	25.86	723.4
	3	4.959	4.212	86.26	40.25	46.01	1268.9
	4	1.661	1.411	47.74	31.21	16.53	486.0
	5	0.679	0.577	34.94	27.72	7.22	257.5
	6	0.000	0.000	26.08	25.35	0.73	109.2
	7	0.126	0.107	27.60	25.70	1.90	136.1
	8	0.992	0.842	40.14	28.83	11.31	361.8
	9	3.978	3.378	74.98	37.44	37.54	1052.1
feb 1st	1	2.327	1.976	55.09	32.25	22.84	669
	2	2.511	2.133	57.43	32.92	24.51	718.3
	3	2.688	2.283	59.71	33.46	26.25	760.5
	4	2.886	2.451	62.21	34.14	28.07	811.5
	5	3.090	2.624	64.73	34.79	29.94	863.3
	6	3.302	2.804	67.21	35.39	31.82	910.4
	7	3.520	2.989	69.82	36.06	33.76	967.6
	8	3.729	3.167	72.56	36.72	35.84	1028.2
	9	3.961	3.364	75.25	37.41	37.84	1078.1
feb 2nd	1	0.000	0.000	25.12	24.38	0.74	108.7
	2	0.220	0.187	27.94	25.15	2.79	158.9
	3	0.880	0.747	36.73	27.51	9.22	316.8
	4	1.980	1.682	48.04	30.55	17.49	534.3
	5	2.688	2.283	55.06	32.31	22.76	676.4
feb 3rd	1	0.498	0.423	32.08	26.57	5.51	229.4
	2	1.380	1.172	43.64	29.64	14.00	451.5
	3	3.090	2.624	65.37	35.44	29.93	893.0
	4	3.520	2.989	70.72	36.79	33.93	1007.3
	5	3.961	3.364	76.20	38.16	38.03	1123.0
	6	4.446	3.776	82.30	39.72	42.57	1246.1

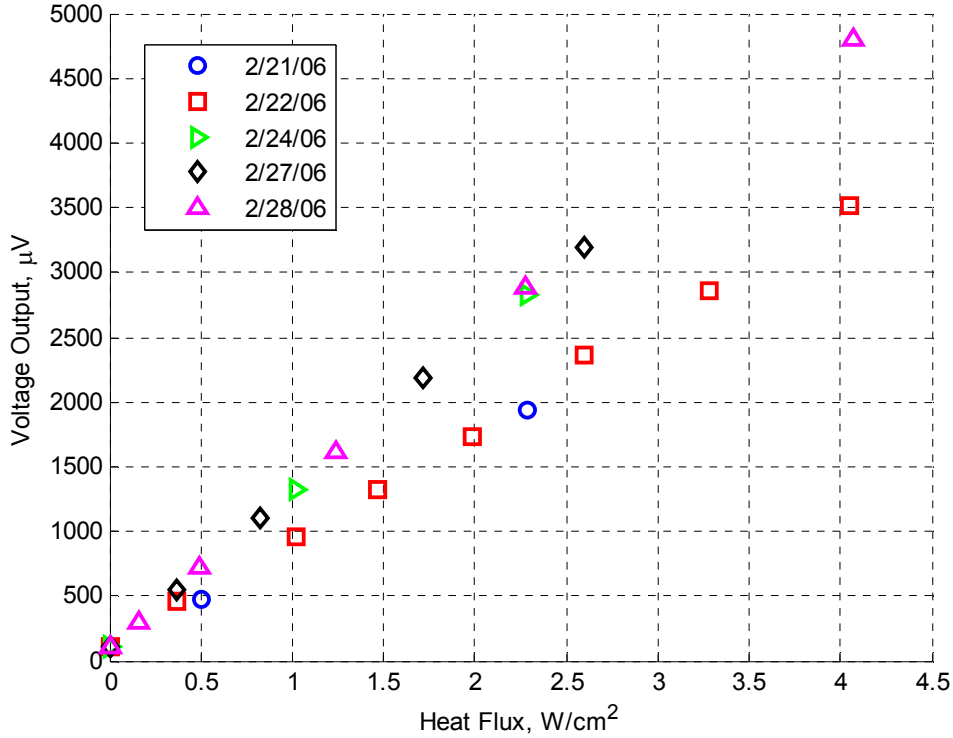

Figure A.4. All data from steady state heat flux sensing tests with the angle $\alpha = 58°$ (B).

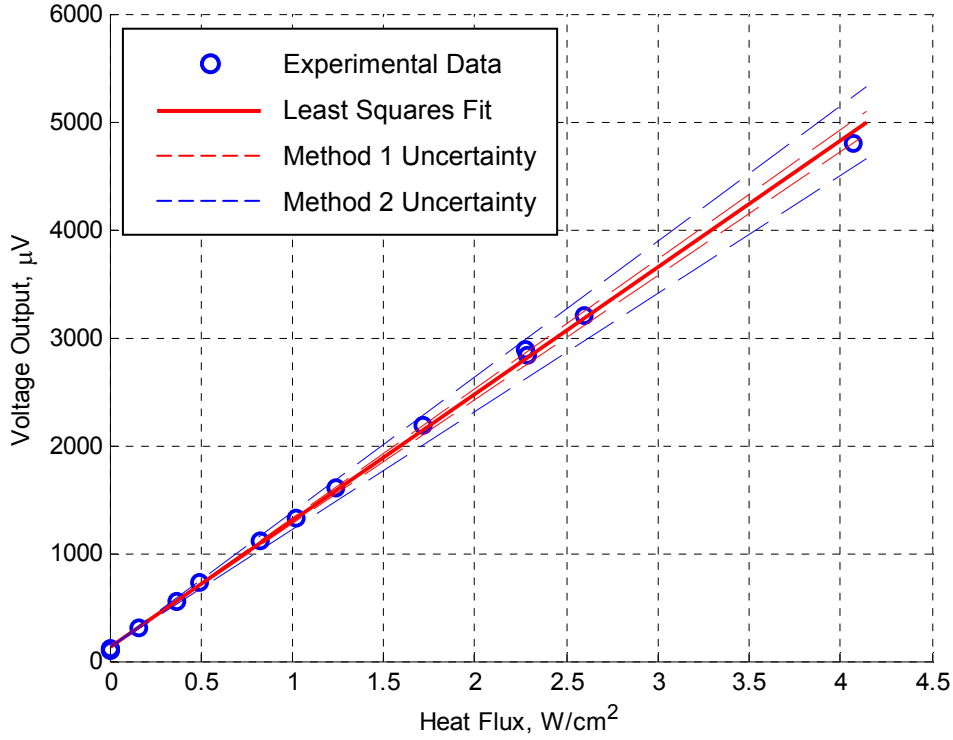

Figure A.5. Truncated data from the angle $\alpha = 58°$ (B). The slope of the least-squares fit is 1172.0 $\mu V/(W/cm^2)$ and the uncertainties from method 1 and method 2 are ±2% and ±6.8% respectively.

Table A.2. Comprehensive tabular data from heat flux sensing tests with $\alpha = 58°$ (B).

	run #	Power (W)	Heat Flux (W/cm^2)	T_{high} (°C)	T_{low} (°C)	Δ T (°C)	Voltage (μV)
2/21/2006	1	0.000	0.000	26.63	25.99	0.64	108.7
	2	0.679	0.502	34.62	28.15	6.46	472.6
	3	3.090	2.284	64.84	36.65	28.19	1932.4
2/22/2006	1	0.000	0.000	24.93	24.25	0.68	107.9
	2	0.498	0.368	31.48	26.12	5.36	465.1
	3	1.380	1.020	40.48	28.64	11.84	963.8
	4	1.980	1.464	46.64	30.31	16.33	1321.5
	5	2.688	1.987	53.74	32.11	21.63	1738.9
	6	3.520	2.602	61.95	34.24	27.72	2362.4
	7	4.446	3.286	70.54	36.49	34.05	2851.7
	8	5.480	4.051	79.94	38.56	41.38	3521.1
2/24/2006	1	0.000	0.000	25.74	25.09	0.65	105.9
	2	1.380	1.020	44.42	30.29	14.13	1324.2
	3	3.090	2.284	66.82	36.14	30.68	2829.9
2/27/2006	1	0.000	0.000	25.66	24.97	0.69	103.7
	2	0.498	0.368	32.40	26.83	5.57	551.2
	3	1.116	0.825	40.89	29.19	11.70	1109.6
	4	2.327	1.720	56.88	33.32	23.56	2191.8
	5	3.520	2.602	72.25	37.36	34.89	3199.0
2/28/2006	1	0.000	0.000	25.35	24.67	0.68	106.4
	2	0.220	0.163	28.61	25.78	2.83	302.3
	3	1.672	1.236	48.14	30.97	17.17	1611.8
	4	5.500	4.065	95.18	42.63	52.55	4798.0
	5	3.075	2.273	66.79	36.10	30.69	2883.2
	6	0.672	0.497	35.39	28.07	7.32	724.1

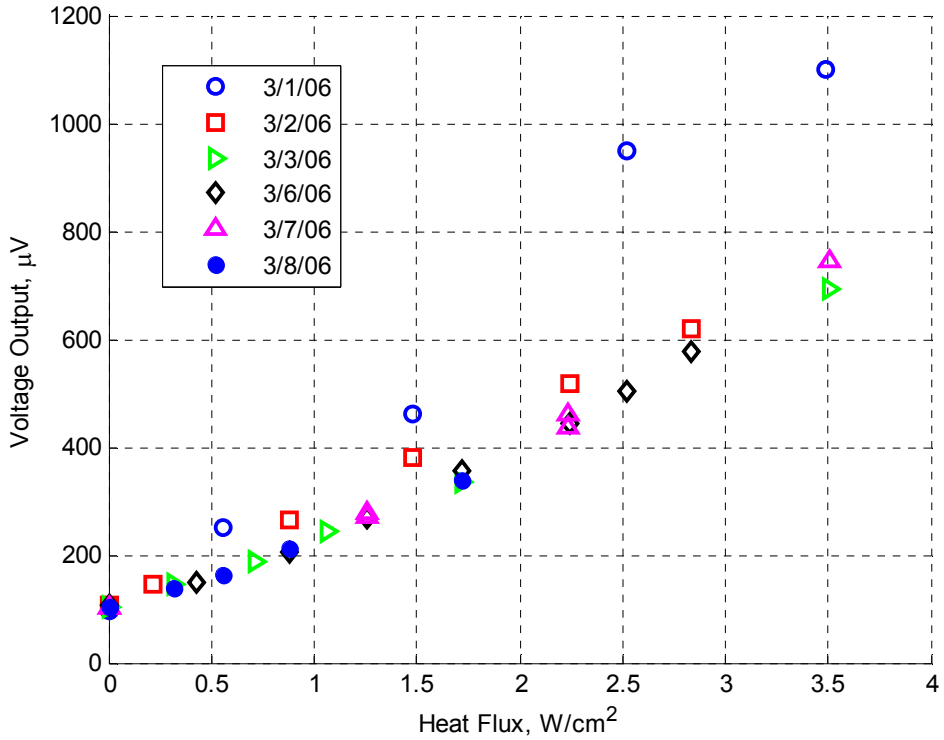

Figure A.6. All data from steady state heat flux sensing tests with the angle $\alpha = 47°$ (C).

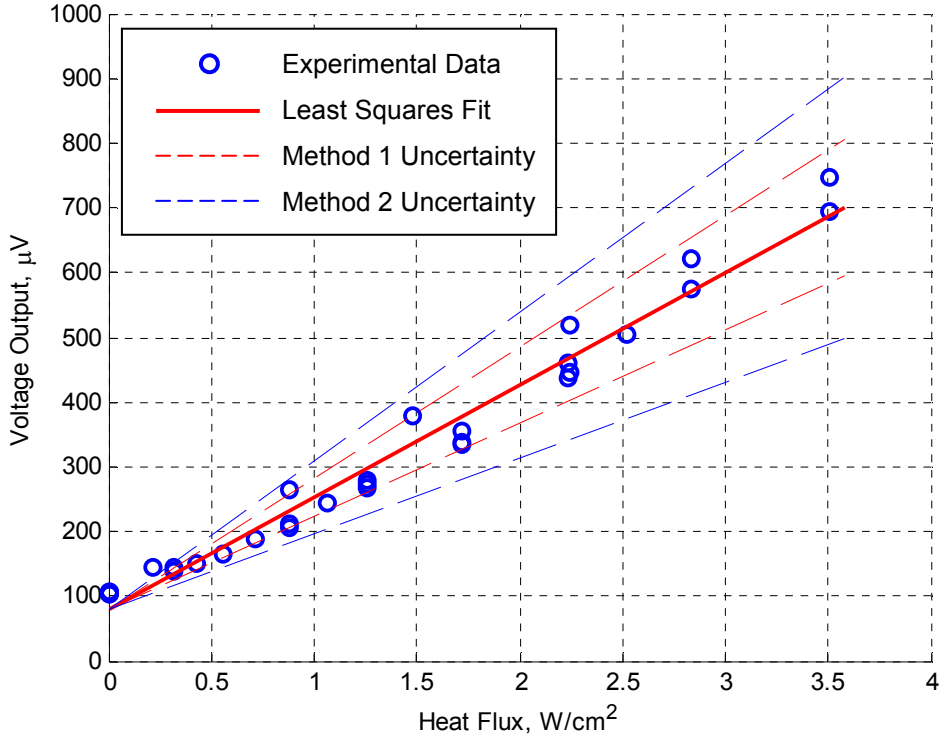

Figure A.7. Truncated data from the angle $\alpha = 47°$ (C). The slope of the least-squares fit is 173.2 $\mu V/(W/cm^2)$ and the uncertainties from method 1 and method 2 are ±15% and ±28.8% respectively.

Table A.3. Comprehensive tabular data from heat flux sensing tests with $\alpha = 47°$ (C).

	run #	Power (W)	Heat Flux (W/cm^2)	T_{high} (°C)	T_{low} (°C)	Δ T (°C)	Voltage (μV)
3/1/2006	1	0.000	0.000	25.68	24.74	0.94	96.50
	2	3.961	2.525	71.68	41.88	29.80	948.10
	3	5.480	3.493	87.48	47.62	39.86	1100.20
	4	0.880	0.561	37.15	29.64	7.51	251.00
	5	2.327	1.483	53.34	35.47	17.87	459.80
3/2/2006	1	0.000	0.000	25.20	24.49	0.72	105.47
	2	0.345	0.220	29.62	26.47	3.14	144.29
	3	1.380	0.880	41.86	31.14	10.73	265.02
	4	2.327	1.483	52.83	35.33	17.50	379.81
	5	3.520	2.244	65.95	40.26	25.70	518.00
	6	4.446	2.834	76.16	44.05	32.11	621.02
3/3/2006	1	0.000	0.000	25.39	24.66	0.73	105.03
	2	0.498	0.317	31.50	27.26	4.24	144.52
	3	1.116	0.711	38.01	29.90	8.11	188.88
	4	1.672	1.066	43.45	31.92	11.53	243.87
	5	2.702	1.722	53.37	35.65	17.72	336.14
	6	5.500	3.506	78.38	44.78	33.60	693.56
3/6/2006	1	0.000	0.000	24.85	24.13	0.72	105.70
	2	0.679	0.433	32.95	27.48	5.48	149.29
	3	1.380	0.880	41.09	30.64	10.45	205.65
	4	1.980	1.262	47.90	33.35	14.55	267.36
	5	2.702	1.722	55.92	36.55	19.37	355.40
	6	3.520	2.244	64.76	39.95	24.82	445.38
	7	3.961	2.525	69.37	41.62	27.75	505.15
	8	4.446	2.834	74.40	43.49	30.91	575.67
3/7/2006	1	0.000	0.000	25.33	24.60	0.73	104.80
	2	1.980	1.262	47.65	33.36	14.29	272.55
	3	5.500	3.506	84.29	46.92	37.37	747.21
	4	3.504	2.234	64.92	40.04	24.88	459.69
	5	1.980	1.262	48.53	34.07	14.46	278.36
	6	3.504	2.234	64.92	39.99	24.93	438.00
3/8/2006	1	0.000	0.000	25.27	24.54	0.73	105.26
	2	0.498	0.317	31.19	27.08	4.12	138.70
	3	0.880	0.561	35.74	28.92	6.82	164.53
	4	1.380	0.880	41.56	31.27	10.29	210.69
	5	2.702	1.722	56.02	36.89	19.13	337.44

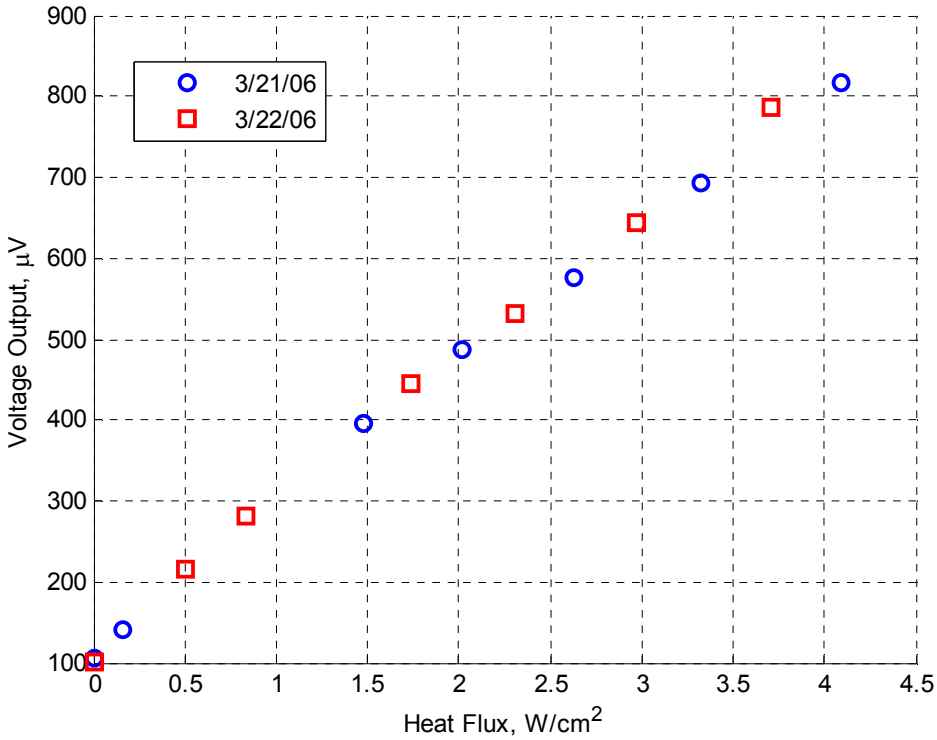

Figure A.8. All data from steady state heat flux sensing tests with the angle α = 59° (D).

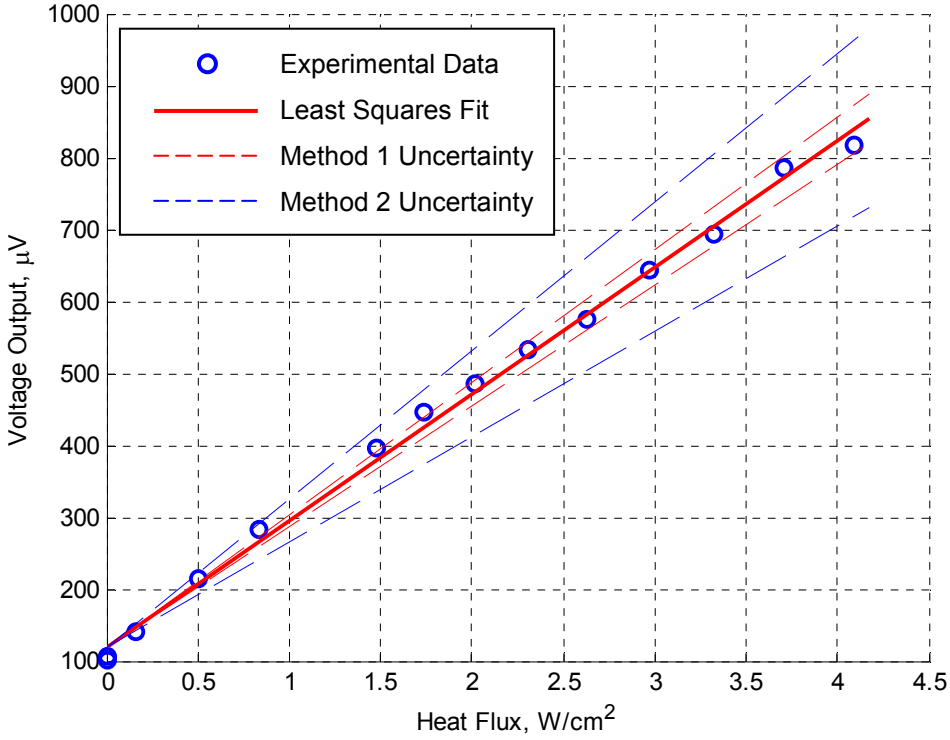

Figure A.9. Truncated data from the angle α = 59° (D). The slope of the least-squares fit is 175.9 μV/(W/cm^2) and the uncertainties from method 1 and method 2 are ±4% and ±14.6% respectively.

Table A.4. Comprehensive tabular data from heat flux sensing tests with $\alpha = 59°$ (D).

	run #	Power (W)	Heat Flux (W/cm^2)	T_{high} (°C)	T_{low} (°C)	Δ T (°C)	Voltage (μV)
3/21/2006	1	1.980	1.479	51.04	34.80	16.24	395.54
	2	2.702	2.019	59.76	38.12	21.64	486.18
	3	3.520	2.630	69.62	41.77	27.85	575.54
	4	4.446	3.322	80.45	45.68	34.76	693.23
	5	5.480	4.094	91.93	49.76	42.18	817.88
	6	0.220	0.164	29.51	27.03	2.48	141.85
	7	0.000	0.000	26.82	26.08	0.74	106.55
3/22/2006	1	0.000	0.000	26.58	25.89	0.69	101.58
	2	0.679	0.507	34.61	28.67	5.94	214.95
	3	1.116	0.834	39.83	30.41	9.42	282.19
	4	2.327	1.739	54.74	35.95	18.79	445.38
	5	3.090	2.309	63.99	39.28	24.71	532.16
	6	3.978	2.972	74.30	42.99	31.32	643.43
	7	4.959	3.705	85.82	47.21	38.61	786.19

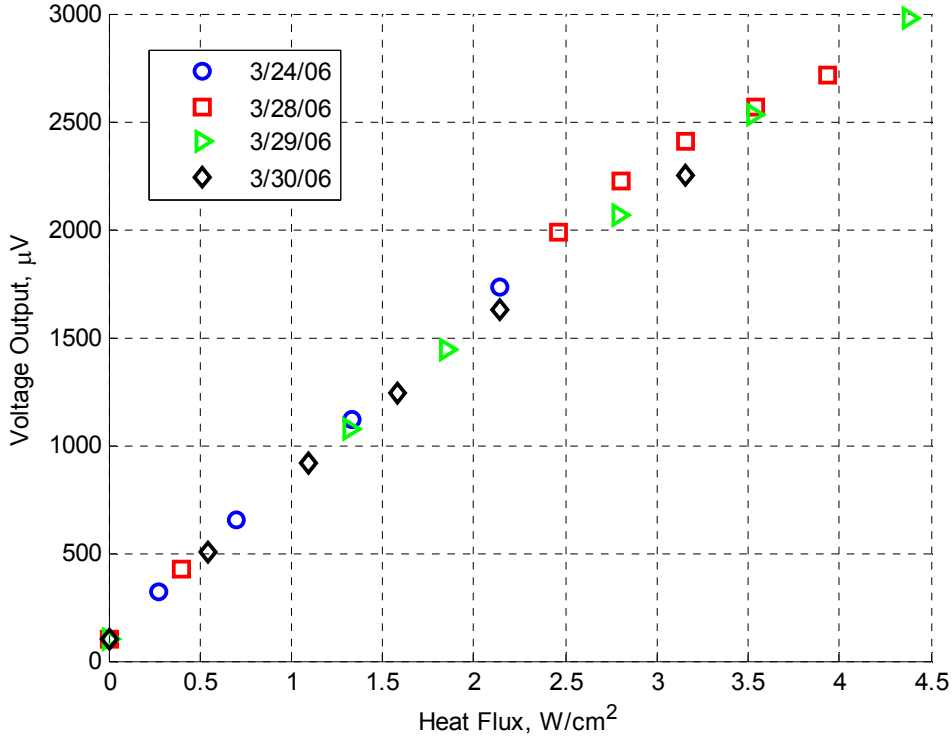

Figure A.10. All data from steady state heat flux sensing tests with the angle α = 66° (E).

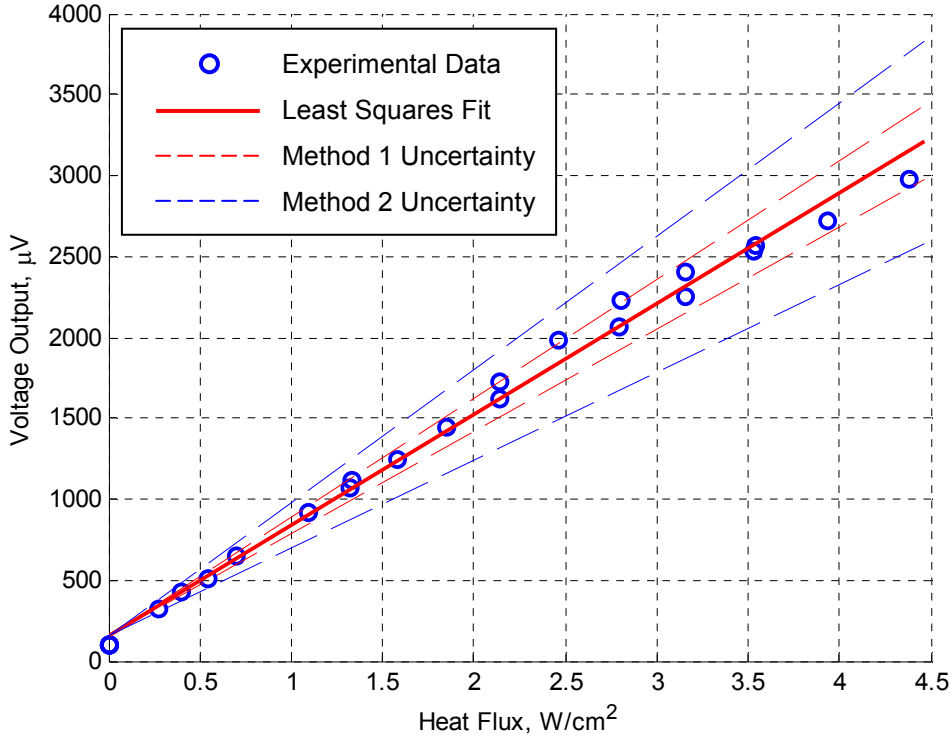

Figure A.11. Truncated data from the angle α = 66° (E). The slope of the least-squares fit is 682.5 μV/(W/cm^2) and the uncertainties from method 1 and method 2 are ±7% and ±19.5% respectively.

Table A.5. Comprehensive tabular data from heat flux sensing tests with $\alpha = 66°$ (E).

	run #	Power (W)	Heat Flux (W/cm^2)	T_{high} (°C)	T_{low} (°C)	Δ T (°C)	Voltage (μV)
3/24/2006	1	0.000	0.000	26.09	25.47	0.62	102.7
	2	0.345	0.275	30.73	27.29	3.44	321.3
	3	0.880	0.701	38.27	30.43	7.84	653.7
	4	1.672	1.331	48.81	34.56	14.25	1122.7
	5	2.688	2.140	62.24	39.88	22.36	1728.8
3/28/2006	1	0.000	0.000	25.50	24.79	0.71	101.5
	2	0.498	0.397	32.66	27.94	4.72	425.0
	3	3.090	2.460	66.37	41.12	25.25	1985.8
	4	3.520	2.803	71.94	43.42	28.52	2224.1
	5	3.961	3.154	77.42	45.56	31.86	2407.2
	6	4.446	3.540	83.04	47.26	35.77	2561.6
	7	4.940	3.934	88.68	49.01	39.66	2718.1
3/29/2006	1	0.000	0.000	25.16	24.46	0.70	104.1
	2	5.500	4.379	94.57	50.55	44.02	2980.3
	3	4.428	3.526	82.53	46.36	36.17	2535.0
	4	3.504	2.790	71.69	42.65	29.04	2067.5
	5	2.327	1.853	56.91	37.20	19.71	1446.9
	6	1.661	1.323	48.12	33.85	14.27	1075.2
3/30/2006	1	0.000	0.000	25.45	24.78	0.67	101.0
	2	0.679	0.541	34.85	28.66	6.19	503.2
	3	1.380	1.099	44.28	32.28	12.00	914.0
	4	1.980	1.577	52.29	35.33	16.95	1242.2
	5	2.688	2.140	61.53	38.87	22.66	1624.9
	6	3.961	3.154	77.28	44.61	32.66	2253.7

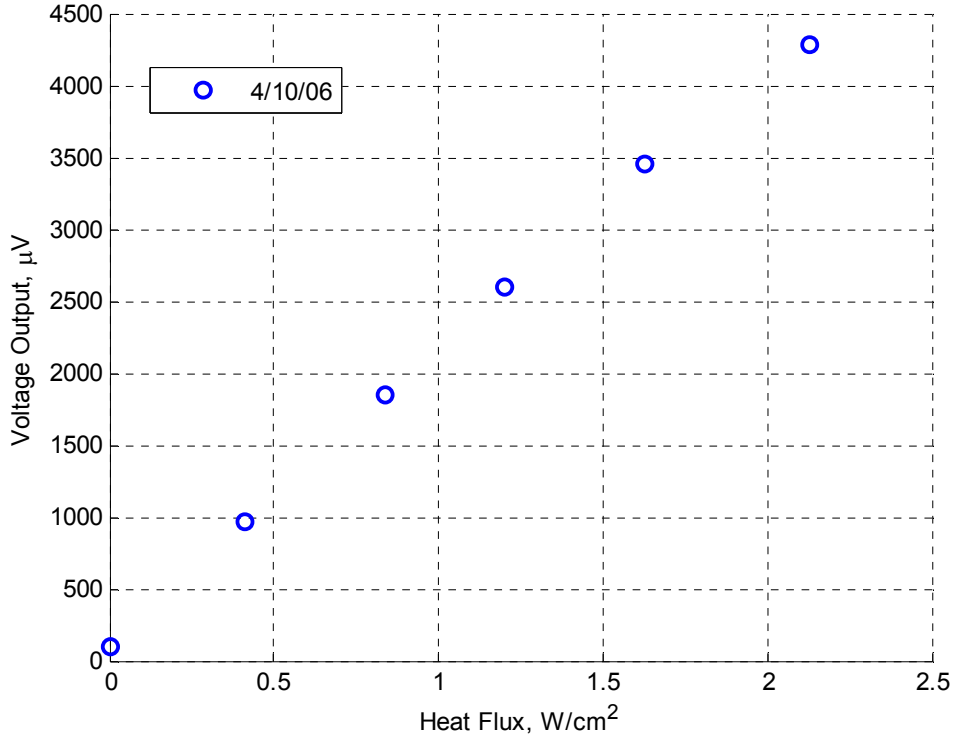

Figure A.12. All data from steady state heat flux sensing tests with the angle α = 44° (F).

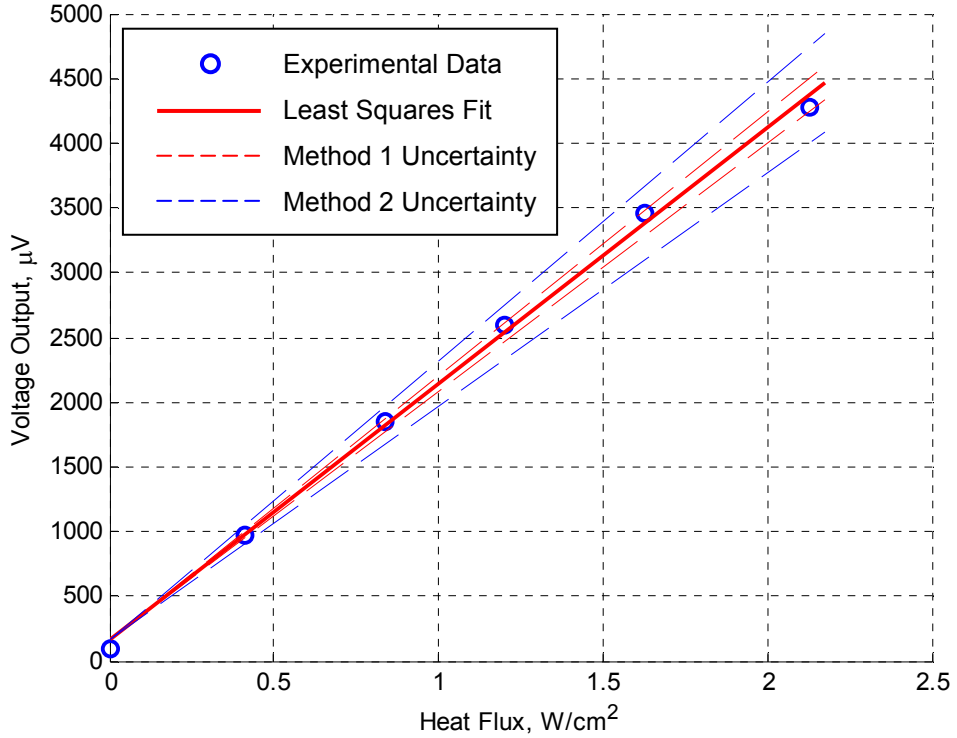

Figure A.13. Truncated data from the angle α = 44° (F). The slope of the least-squares fit is 1980.1 μV/(W/cm^2) and the uncertainties from method 1 and method 2 are ±3% and ±8.5% respectively.

Table A.6. Comprehensive tabular data from heat flux sensing tests with $\alpha = 44°$ (F).

	run #	Power (W)	Heat Flux (W/cm^2)	T_{high} (°C)	T_{low} (°C)	Δ T (°C)	Voltage (μV)
4/10/2006	1	0.000	0.000	24.83	24.12	0.71	100.7
	2	0.679	0.411	34.70	28.68	6.02	970.2
	3	1.380	0.836	45.14	33.63	11.51	1854.4
	4	1.980	1.199	53.84	37.64	16.20	2601.7
	5	2.688	1.628	63.75	42.17	21.59	3454.2
	6	3.520	2.131	74.78	47.02	27.76	4280.3

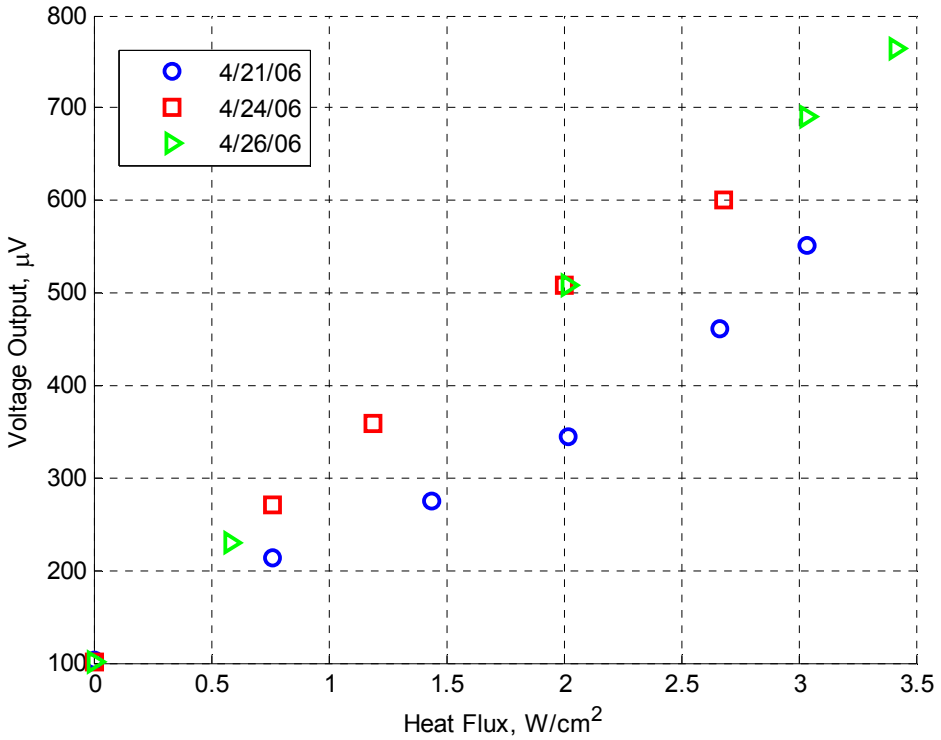

Figure A.14. All data from steady state heat flux sensing tests with the angle α = 84° (G).

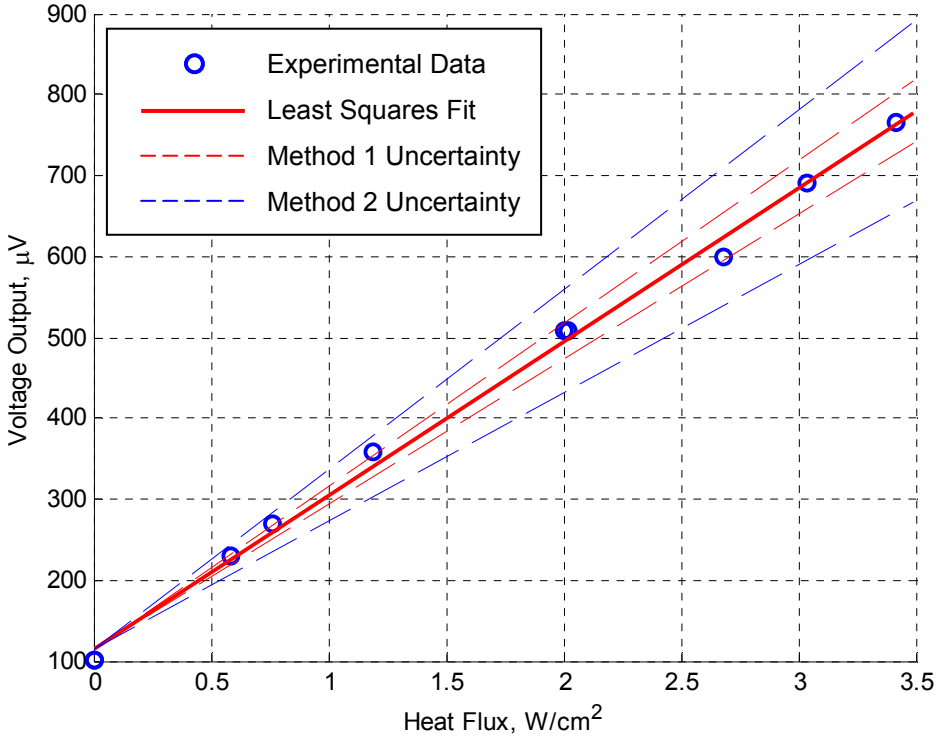

Figure A.15. Truncated data from the angle α = 84° (G). The slope of the least-squares fit is 190.2 μV/(W/cm^2) and the uncertainties from method 1 and method 2 are ±5% and ±14.2% respectively.

Table A.7. Comprehensive tabular data from heat flux sensing tests with $\alpha = 84°$ (G).

	run #	Power (W)	Heat Flux (W/cm^2)	T_{high} (°C)	T_{low} (°C)	Δ T (°C)	Voltage (μV)
4/21/2006	1	0.000	0.000	26.06	25.43	0.63	102.8
	2	0.880	0.763	41.11	29.76	11.35	214.2
	3	1.661	1.440	54.01	33.45	20.56	276.0
	4	2.327	2.017	64.60	36.42	28.18	345.6
	5	3.075	2.666	76.32	39.51	36.81	462.2
	6	3.504	3.037	82.72	41.20	41.52	551.1
4/24/2006	1	0.000	0.000	25.51	24.91	0.60	101.9
	2	0.880	0.763	40.64	29.13	11.51	270.6
	3	1.370	1.188	48.61	31.20	17.42	359.4
	4	2.314	2.006	63.59	35.21	28.39	508.2
	5	3.090	2.679	75.52	38.49	37.03	599.7
4/26/2006	1	0.000	0.000	25.19	24.59	0.60	100.6
	2	0.672	0.583	37.08	28.12	8.97	230.0
	3	2.327	2.017	63.98	35.40	28.58	507.9
	4	3.504	3.037	82.20	40.15	42.05	689.8
	5	3.944	3.419	88.92	41.91	47.01	764.6

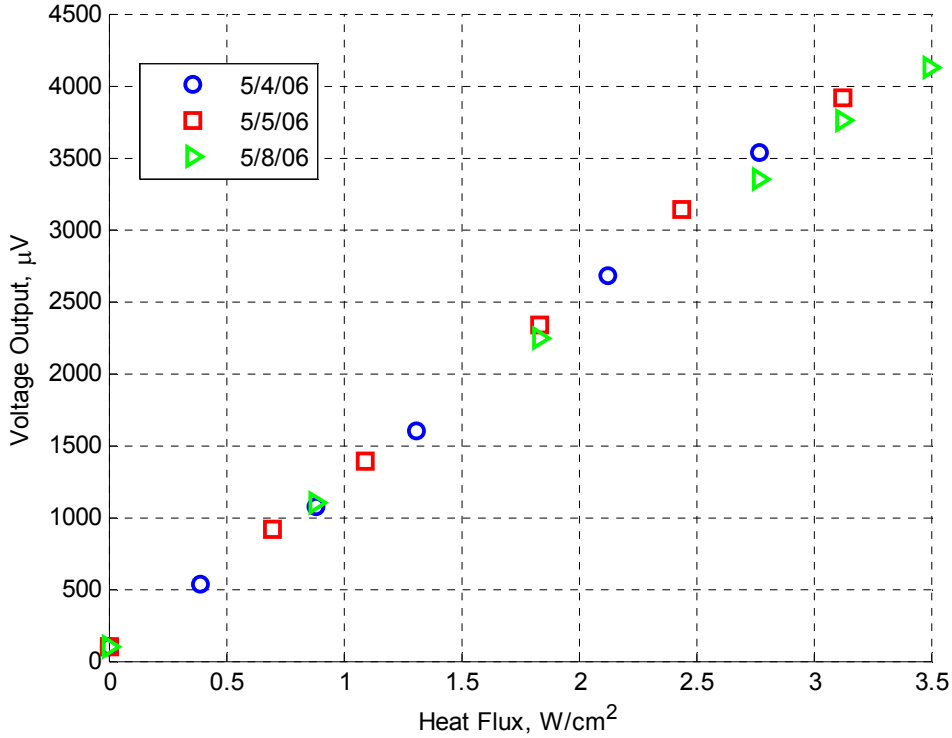

Figure A.16. All data from steady state heat flux sensing tests with the angle α = 65° (H).

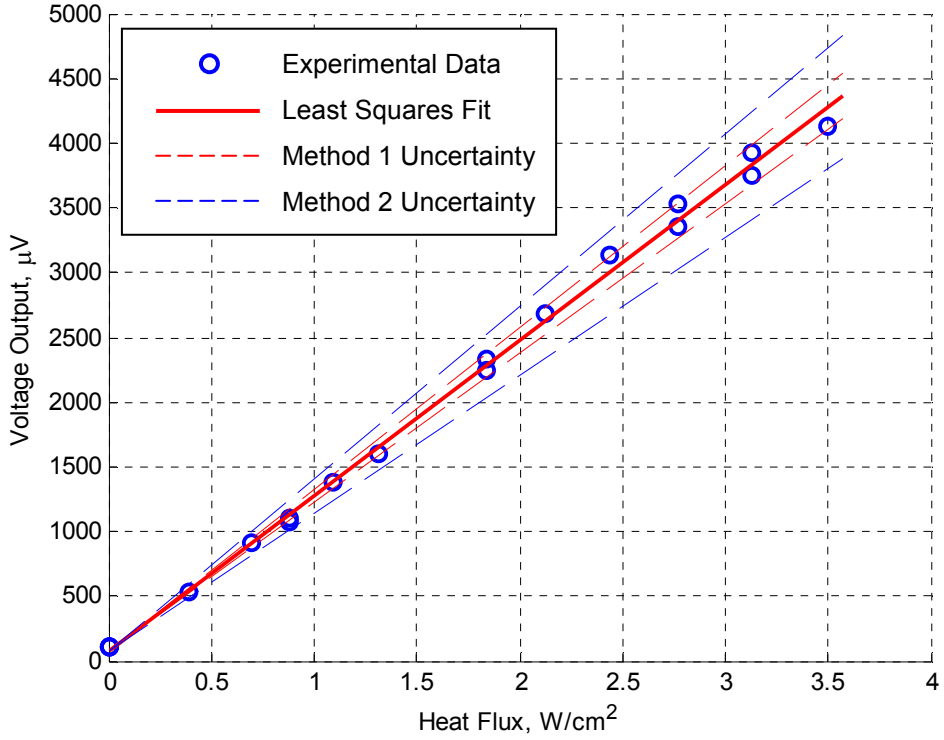

Figure A.17. Truncated data from the angle α = 65° (H). The slope of the least-squares fit is 1197.8 μV/(W/cm^2) and the uncertainties from method 1 and method 2 are ±4% and ±11.0% respectively.

Table A.8. Comprehensive tabular data from heat flux sensing tests with α = 65° (H).

	run #	Power (W)	Heat Flux (W/cm^2)	T_{high} (°C)	T_{low} (°C)	Δ T (°C)	Voltage (μV)
5/4/2006	1	0.000	0.000	26.32	25.67	0.65	103.1
	2	0.498	0.393	33.85	28.68	5.17	527.2
	3	1.116	0.882	43.00	32.10	10.90	1077.4
	4	1.661	1.312	51.01	35.06	15.95	1599.4
	5	2.688	2.123	66.04	40.73	25.30	2683.5
	6	3.504	2.768	77.41	44.84	32.57	3536.7
5/5/2006	1	0.000	0.000	27.05	26.34	0.71	102.4
	2	0.880	0.695	40.18	31.43	8.74	917.6
	3	1.380	1.090	47.54	34.21	13.33	1387.3
	4	2.327	1.838	61.22	39.26	21.97	2338.4
	5	3.090	2.441	72.11	43.29	28.82	3133.1
	6	3.961	3.129	84.04	47.49	36.55	3919.0
5/8/2006	1	0.000	0.000	26.25	25.56	0.69	102.7
	2	1.116	0.882	42.72	31.87	10.85	1101.6
	3	2.327	1.838	60.21	38.36	21.86	2248.4
	4	3.504	2.768	77.25	44.63	32.62	3349.5
	5	3.961	3.129	83.57	47.03	36.54	3751.9
	6	4.428	3.498	90.02	49.37	40.65	4123.9

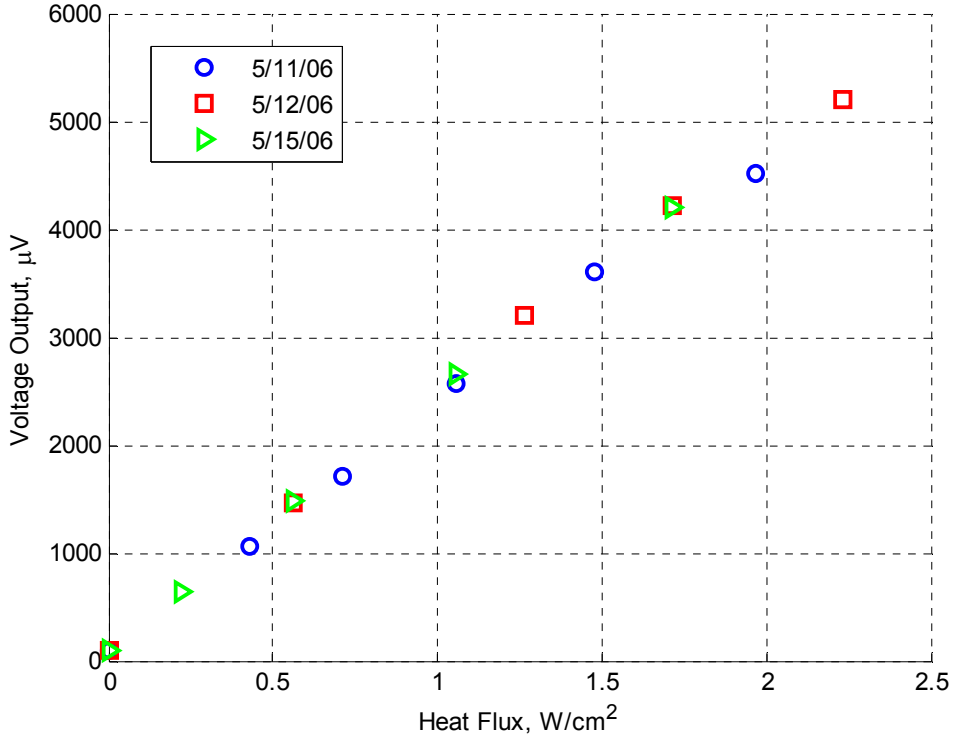

Figure A.18. All data from steady state heat flux sensing tests with the angle α = 47° (I).

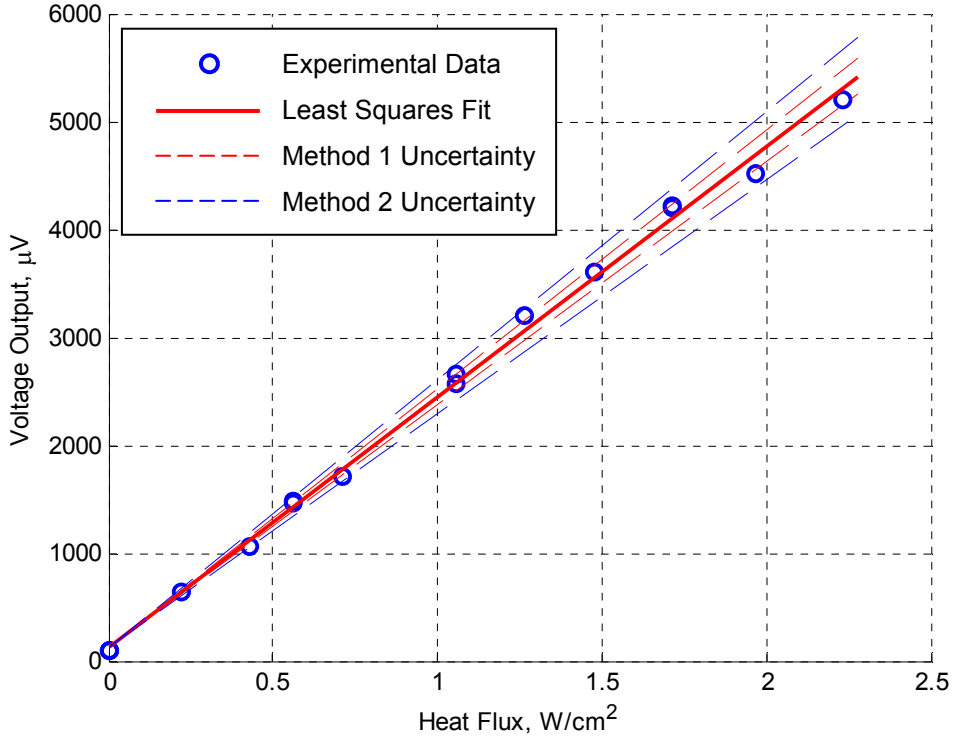

Figure A.19. Truncated data from the angle α = 47° (I). The slope of the least-squares fit is 2321.6 μV/(W/cm^2) and the uncertainties from method 1 and method 2 are ±3% and ±6.7% respectively.

Table A.9. Comprehensive tabular data from heat flux sensing tests with $\alpha = 47°$ (I).

	run #	Power (W)	Heat Flux (W/cm^2)	T_{high} (°C)	T_{low} (°C)	Δ T (°C)	Voltage (μV)
5/11/2006	1	0.000	0.000	26.70	26.05	0.65	104.8
	2	0.672	0.428	39.38	32.86	6.53	1058.5
	3	1.116	0.711	47.80	37.47	10.33	1711.4
	4	1.661	1.059	58.03	43.06	14.98	2573.0
	5	2.314	1.475	69.92	49.63	20.29	3606.6
	6	3.090	1.970	83.28	57.01	26.27	4513.7
5/12/2006	1	0.000	0.000	25.82	25.13	0.69	101.8
	2	0.880	0.561	42.88	34.80	8.07	1469.0
	3	1.980	1.262	63.63	46.44	17.20	3198.6
	4	2.688	1.713	76.69	53.71	22.98	4211.2
	5	3.504	2.234	91.14	61.57	29.57	5209.7
5/15/2006	1	0.000	0.000	24.96	24.27	0.69	97.7
	2	0.345	0.220	32.09	28.56	3.53	634.4
	3	0.880	0.561	42.69	34.67	8.01	1481.7
	4	1.661	1.059	57.67	43.23	14.43	2659.1
	5	2.688	1.713	76.89	53.97	22.92	4199.7

Appendix B – Other Measurements

This appendix shows the pertinent experimental data that was not included in the main text of this report.

The following two plots show results of a transient heat flux sensing test with a device with an angle of $\alpha = 60°$ that was constructed using silver paint to connect the layers. The resulting output voltage follows closely the temperature difference across the device, indicating a good response time. Since the temperature difference was measured across the height of the device and the voltage was measured along the length, the results indicate that the device is indeed displaying transverse thermoelectric effects.

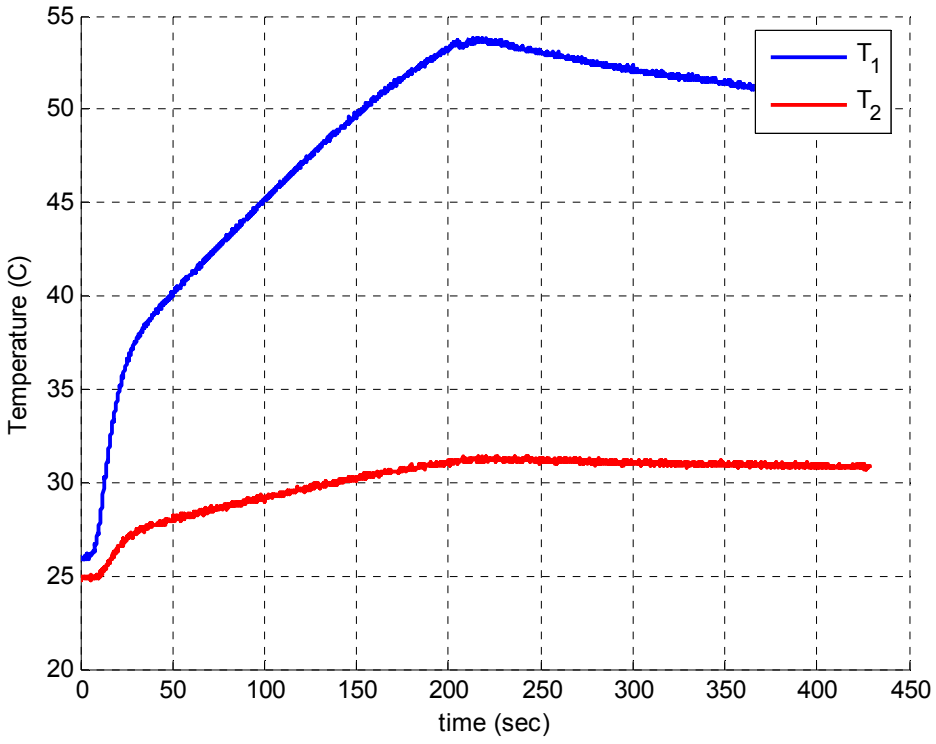

Figure B.1. The temperatures of the top and bottom surfaces of the device under a changing value of heat flux.

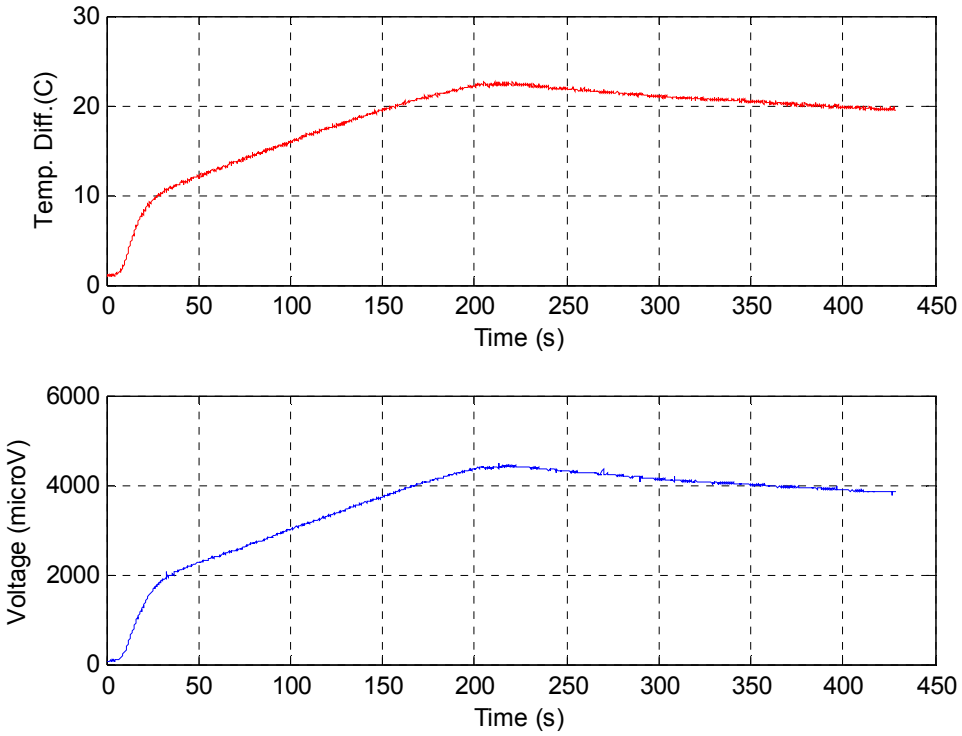

Figure B.2. The voltage and temperature difference associated with the transient test.

The next two plots show the results of Seebeck coefficient measurements on samples of bismuth and bismuth telluride. The methods of obtaining these results are described in Chapter 3.

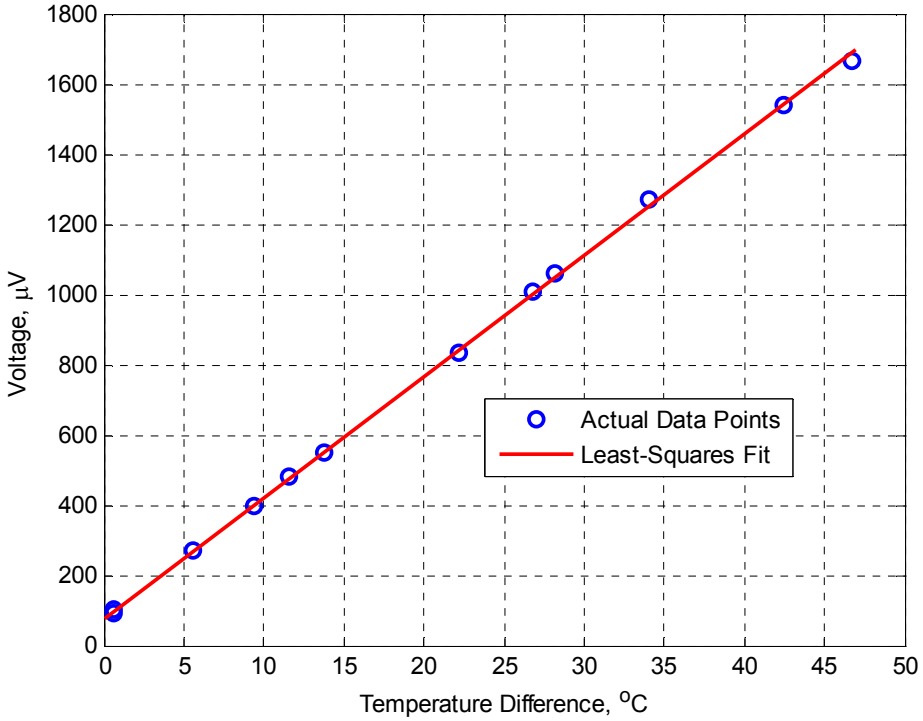

Figure B.3. Steady state data points and the least-squares fit for the measurement of the Seebeck coefficient of a sample of bismuth. The Seebeck coefficient was determined to be S = 34.5 μV/K.

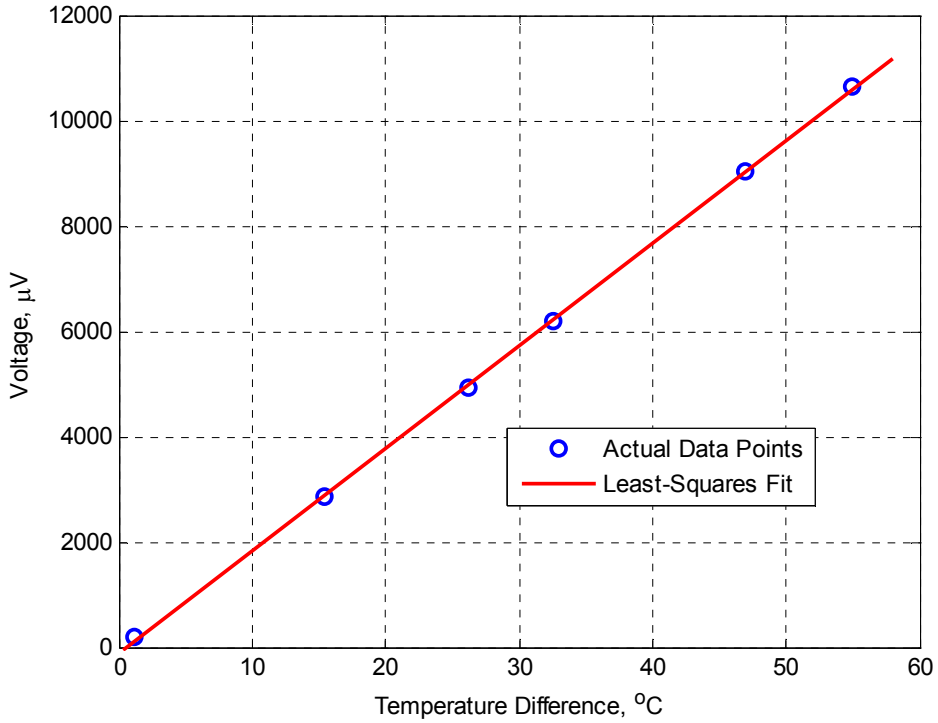

Figure B.4. Steady state data points and the least-squares fit for the measurement of the Seebeck coefficient of a sample of bismuth telluride. The Seebeck coefficient was determined to be S = 190 μV/K.

Appendix C – Pictures of the Device

Figure C.1. A picture of the device with α = 77° (A).

Figure C.2. A picture of the device with α = 58° (B).

Figure C.3. A picture of the device with α = 47° (C).

Figure C.4. A picture of the device with α = 59° (D).

Figure C.5. A picture of the device with α = 66° (E).

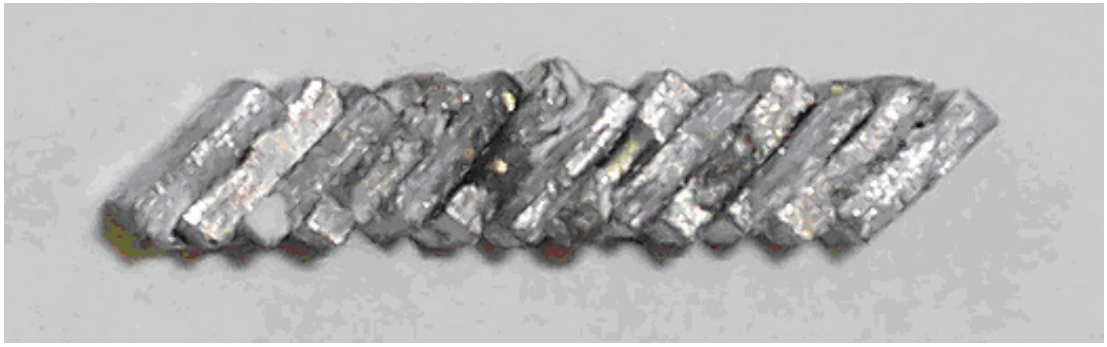

Figure C.6. A picture of the device with α = 44° (F).

Figure C.7. A picture of the device with α = 84° (G).

Figure C.8. A picture of the device with α = 65° (H).

Figure C.9. A picture of the device with α = 47° (I).

Vita

Brooks Samuel Mann was born on March 10th, 1982 in Charleston, South Carolina to Gail and Stephan Mann. After several years in South Carolina and the Washington, D.C. area, Brooks and his family moved to Frederick, Maryland. Brooks played baseball and soccer as a child, and played soccer into his high school years. Brooks graduated from Governor Thomas Johnson High School in 2000, and continued on to the engineering school at Virginia Tech. He worked as an Undergraduate Research Assistant under Dr. Ricardo Burdisso as a junior and senior, graduated with a B.S. in Mechanical Engineering in 2004, and stayed at Virginia Tech to pursue a graduate degree. Brooks worked as a Graduate Teaching Assistant for M.E. Lab II in the fall of 2004, and then became a Graduate Research Assistant working toward his thesis under Dr. Scott Huxtable. Brooks graduated with an M.S. in Mechanical Engineering in 2006.